



Michigan Technological University
Create the Future Digital Commons @ Michigan Tech

Dissertations, Master's Theses and Master's
Reports - Open

Dissertations, Master's Theses and Master's
Reports

2011

Ultraviolet digital imaging of volcanic plumes : implementation and application to magmatic processes at basaltic volcanoes

Patricia Amanda Nadeau
Michigan Technological University

Follow this and additional works at: <https://digitalcommons.mtu.edu/etds>



Part of the [Geology Commons](#)

Copyright 2011 Patricia Amanda Nadeau

Recommended Citation

Nadeau, Patricia Amanda, "Ultraviolet digital imaging of volcanic plumes : implementation and application to magmatic processes at basaltic volcanoes", Dissertation, Michigan Technological University, 2011.
<https://doi.org/10.37099/mtu.dc.etds/336>

Follow this and additional works at: <https://digitalcommons.mtu.edu/etds>



Part of the [Geology Commons](#)

ULTRAVIOLET DIGITAL IMAGING OF VOLCANIC PLUMES:
IMPLEMENTATION AND APPLICATION TO MAGMATIC PROCESSES AT
BASALTIC VOLCANOES

By

Patricia Amanda Nadeau

A DISSERTATION
Submitted in partial fulfillment of the requirements for the degree of
DOCTOR OF PHILOSOPHY
(Geology)

MICHIGAN TECHNOLOGICAL UNIVERSITY
2011

©2011 Patricia Amanda Nadeau

This dissertation, “Ultraviolet Digital Imaging of Volcanic Plumes: Implementation and Application to Magmatic Processes at Basaltic Volcanoes,” is hereby approved in partial fulfillment of the requirements for the Degree of DOCTOR OF PHILOSOPHY IN GEOLOGY.

Department of Geological and Mining Engineering and Sciences

Signatures:

Dissertation Co-Advisor

Dr. Simon A. Carn

Dissertation Co-Advisor

Dr. Gregory P. Waite

Department Chair

Dr. Wayne D. Pennington

Date

*"The smell of sulphur is strong, but
not unpleasant to a sinner."*

~Mark Twain, Letters from Hawaii

TABLE OF CONTENTS

List of Figures	viii
List of Tables.....	xiii
Preface	xiv
Acknowledgements	xv
Abstract	xvii
Chapter 1: Introduction.....	1
1.1 The role of gas in volcanism.....	1
1.2 Measurement of volcanic gases	2
1.2.1 Direct sampling.....	3
1.2.2 Satellite measurements.....	4
1.2.3 Ground-based remote sensing.....	4
1.2.3.1 COSPEC	5
1.2.3.2 Miniature DOAS-based spectrometers.....	6
1.2.3.3 UV cameras.....	7
1.3 Objectives	11
1.4 Study sites	12
1.4.1 Fuego volcano, Guatemala.....	12
1.4.1.1 Geologic setting	12
1.4.1.2 Recent volcanic activity	13
1.4.1.3 Previous Studies	14
1.4.2 Kilauea volcano, Hawaii	15
1.4.2.1 Geologic setting	15
1.4.2.2 Recent volcanic activity	16
1.4.2.3 Previous and Relevant Studies.....	17
1.4.2.3.1 Gas studies at Kilauea.....	17
1.4.2.3.2 Seismo-acoustic studies at Kilauea	18
1.4.2.3.3 Integration of gas and geophysics at Kilauea	20
1.5 Dissertation format	21
1.6 References.....	21

Chapter 2:	A Matlab Program For Deriving Emission Rates of Volcanic SO₂ from UV Imagery	29
2.1	Abstract.....	29
2.2	Introduction	29
2.3	Methodology and algorithms.....	31
2.3.1	<i>Image and sequence viewing</i>	32
2.3.2	<i>SO₂ column amount extraction</i>	37
2.3.2.1	Initial input.....	37
2.3.2.2	Profile selection.....	37
2.3.2.3	Calibration.....	39
2.3.2.4	Integrated column amount (ICA) derivation.....	39
2.3.3	<i>Plume speed determination</i>	43
2.3.4	<i>SO₂ emission rate calculations</i>	44
2.3.5	<i>Other programs</i>	45
2.4	Validation.....	45
2.4.1	<i>SO₂ emission rates</i>	45
2.4.2	<i>Plume speed</i>	46
2.4.3	<i>Associated errors</i>	49
2.5	Conclusions	49
2.6	Acknowledgements	51
2.7	References.....	51
Chapter 3:	Linking Volcanic Tremor, Degassing, and Eruption Dynamics via SO₂ Imaging	55
3.1	Abstract.....	55
3.2	Introduction	55
3.3	Methods	57
3.4	Results	57
3.5	Discussion and Conclusions.....	61
3.6	Acknowledgements	65
3.7	References.....	65

Chapter 4:	Examining the Role of Degassing in Recent Summit Activity, Kilauea Volcano, Hawaii	68
4.1	Abstract.....	68
4.2	Introduction	68
4.3	Methodology	70
4.4	Results	71
4.4.1	<i>SO₂ emissions</i>	71
4.4.1.1	Potential errors	73
4.4.2	<i>Seismicity</i>	73
4.4.3	<i>Infrasound and tilt</i>	76
4.4.4	<i>Vent rim camera</i>	78
4.4.5	<i>High stand summary</i>	81
4.5	Discussion.....	81
4.5.1	<i>Models for gas pistonning</i>	81
4.5.1.1	Slug rise.....	81
4.5.1.2	Gas accumulation	86
4.5.1.3	Cyclic pressure variations	88
4.5.2	<i>High stand mechanism</i>	90
4.5.3	<i>Geophysical implications</i>	93
4.6	Conclusions	96
4.7	Acknowledgements	97
4.8	References.....	97
Chapter 5:	Conclusions	101
5.1	Summary of results.....	101
5.2	Limitations of the UV camera.....	102
5.3	Future recommendations	104
5.4	References.....	105
	Complete Reference List.....	107

Appendix A: SO₂ emissions at Fuego volcano, 2008	119
A.1 Introduction	119
A.2 UV camera measurements	119
A.3 Seismic measurements	120
A.4 Results and preliminary discussion.....	120
A.5 References.....	125
Appendix B: Supplement to Chapter 2 – UVCamSO₂: Image processing program for extraction of SO₂ emission rates from UV imagery (User manual and tutorial).....	127
B.1 Introduction	127
B.2 Display of individual images.....	129
B.3 Creating movies with multiple images	135
B.4 Deriving integrated column amounts of SO ₂	139
B.5 Calculating plume speed.....	151
B.6 Back-calculation of time vector.....	154
B.7 Emission rate calculation	156
B.8 Data display	156
Appendix C: Supplement to Chapter 2 – Program codes and sample data	159
Appendix D: Supplement to Chapter 2 – Sample output files	160
D.1 Integrated column amount (multi_image_processing_code.m)	160
D.2 Plume speed (plumespeed.m).....	168
D.3 Back-calculation to vent (backcalc.m).....	171
D.4 Emission rate (ERcalc.m).....	172
Appendix E: Supplement to Chapter 3 – Methodology to derive emission rates of sulfur dioxide from UV imagery.....	174
E.1 References.....	177
Appendix F: Copyright Permissions	179

LIST OF FIGURES

Figure 1.1:	UV camera filter response and absorption cross section of SO ₂ from 285-345 nm. Gray curve is SO ₂ absorption, red curve is 307 nm filter, and blue curve is 326 nm filter. Figure created from data from Vandaele et al. [2009] and Andover Corporation (http://www.andovercorp.com/Web_store/Standard_BP/Std_BP_300nm.php).....	9
Figure 2.1:	Schematic diagram of UVCamSO2 program and subroutines. Rounded boxes represent main modules and empty rectangles their associated outputs. Gray rectangles represent interactive user inputs and critical steps in the program. Many more intermediate steps exist, but are excluded from the diagram for clarity. Dotted arrows point to optional steps in the program flow. Note the absence of lateral steps on the diagram; processes follow directly from top to bottom in the image.	33
Figure 2.2:	Main GUI window for UVCamSO2 program. All options may be run independently of each other, though emission rate calculations and data display require input of previously processed data files.	34
Figure 2.3:	Calibration cell selection. The user dictates the dimensions of the rectangle selected, and may zoom in or re-do their selection as necessary using the buttons at the bottom of the image window.....	36
Figure 2.4:	Sample input windows for subroutines of UVCamSO2. (a) Movie making input window. (b) Main ICA derivation input window. Other subroutines utilize similar input windows.	38
Figure 2.5:	A sample calibration curve derived from calibration cell selection. Linear curves are fit to the absorbance data, having been shown to be valid for concentration path-lengths of up to ~1500 ppm·m [<i>Dalton et al., 2009</i>].....	40
Figure 2.6:	Stack of profiles from successive images for background drift correction. a) Profiles from successive images are stacked; time increases to the right. Note variable brightness of background sky pixels on either side of plume trace including gradual drift as a result of brightening sky and sharp transitions reflecting exposure time changes. b) Representative ranges of background pixels are designated by the user. Average values for background pixels for each individual profile are calculated and subtracted from each pixel in the profile. c) Background drift has been mostly eliminated and background sky values have been set to zero.....	41

Figure 2.7:	ICA data from UV camera and FLYSPEC at Masaya Volcano, Nicaragua on March 18, 2008. Camera data are represented by gray circles; FLYSPEC data points (back-calculated to the approximate time of emission at the volcanic vent) are shown as black triangles.....	47
Figure 2.8:	Coincident UV camera-derived plume speeds (gray dots) and 10-minute average anemometer wind speeds (black triangles) from weather station located ~2 km from the plume at the Hawaiian Volcano Observatory. Data are from May 22, 2010.	48
Figure 3.1:	Examples of activity at Fuego volcano, Guatemala. (a) Ultraviolet (UV) camera imagery of variable gas emissions from two vents prior to an explosion. Times are GMT on 21 January 2009; UV image width is ~260 m and view is to the south. (b) Example of an ash-rich explosion plume (~450 m in height above summit). Explosions were variable in size; column heights reached a maximum of ~500 m above the summit. Explosion onsets ranged from emergence of a single pulse of ash from the summit area driven solely by buoyancy to momentum-driven jets with sustained pulsing for up to ~2 minutes.	58
Figure 3.2:	SO ₂ emission rates from Fuego volcano on 21 January 2009. Portions of plots with no SO ₂ data reflect periods of meteorological cloud or ash in the field of view or pauses in data acquisition for calibration. Note different x- and y-scales for a, b, and c. (a) Emission rates of SO ₂ (circles) plotted alongside explosion occurrences (vertical gray lines; numbered for reference). Dashed box denotes subset region shown in inset. (b) Emission rates of SO ₂ when emissions from distinct plumes were identified. (c) Example of ~30 minute period of similarity between SO ₂ emission rate (circles) and low-frequency 10 second average seismic amplitude (RSAM; black line). Note 32 s offset between x-axes to compensate for overall lag. (d) Increasing lag between RSAM and SO ₂ emission rate for time period in c. Lags were calculated using a moving 6.5-minute window with 5.5-minute overlap. Diamonds with outline represent lags with a correlation coefficient greater than 0.65.	59
Figure 3.3:	Schematic model of gas release and explosion generation for small ash-rich explosions at Fuego volcano, with theoretical SO ₂ release over time. (a) Both vents degas freely. (b) Rheological stiffening in upper conduit inhibits gas release from summit; flank degassing is unaffected. (c) Pressure beneath stiffened magma overcomes confining pressure, resulting in ash-rich explosion and release of accumulated gas before a return to free degassing.	63
Figure 4.1:	Map of Kilauea summit, showing instrument locations. Pale yellow line indicates approximate plume direction under trade wind conditions and blue line is approximate UV camera look direction.	72
Figure 4.2:	SO ₂ emission rate time series from Kilauea volcano, May 22, 2010.	74

Figure 4.3:	Sample plume imagery from May 22, 2010. (a) Lofting plume (b) Grounded plume, which may lead to underestimation of emission rates. Image field of view is approximately 1440 m.....	75
Figure 4.4:	Three phases of high stand seismicity, with spectral characteristics. (a) Seismic trace spanning first high stand on May 22, 2010. BG denotes background level tremor prior to the high stand, HS is high stand, and D is draining. Shaded areas indicate the 5000 s duration subsets used for calculation of long-term spectra; dashed boxes are 200 s subsets for short-term spectra. (b) Spectra for background tremor over 5000 and 200 s, left to right. (c) Spectra for high stand tremor over 5000 and 200 s, left to right. (d) Spectrum for draining over 200 s. A longer 5000 s spectrum could not be determined, as draining events occur over a short duration.....	77
Figure 4.5:	Sequence of HVO web camera images from a high stand on May 22, 2010, during UV camera data acquisition. (a) Lava at low stand, or base level, obscured by the plume. Dotted line indicates edge of lava lake. (b) Lava at low stand, barely visible through plume. (c) Lava at high stand. Note brightly-lit rocks in image foreground, as plume is diminished, allowing sunlight to illuminate ground surface. (d) Onset of lava draining.	79
Figure 4.6:	Sequence of HVO web camera images from a high stand during the night of October 5 – 6, 2010, illustrating clarity of web camera in the absence of sunlight. (a) Lava at low stand, or base level. (b) Lava ~20-30 m higher in vent at high stand. (c) Lava draining back to base level. Note preferential spattering and gas escape at edge of lake along conduit wall. (d) Lava post-high stand, back down to near base level, with some continued spatter along conduit wall.	80
Figure 4.7:	SO ₂ emission rate, radial tilt, and seismicity for onset of second lava high stand, May 22, 2010. Bottom panel is a spectrogram of seismic data; cool and warm colors are weak and strong seismicity at the corresponding time and frequency, respectively.	83
Figure 4.8:	SO ₂ emission rate, radial tilt, and seismicity for termination of second lava high stand, May 22, 2010.	84
Figure 4.9:	SO ₂ budget for two lava high stands of May 22, 2010.	89
Figure A.1:	VLP (12 – 60 s) seismic velocity and SO ₂ emission rate at Fuego volcano, January 15, 2008. Dashed gray lines are coincident with maximum VLP velocity and extend into the SO ₂ portion of the plot to indicate VLP occurrences relative to the SO ₂ peaks that follow.	121
Figure A.2:	Peak VLP velocity versus emitted SO ₂ mass for six VLP events at Fuego volcano in 2008. Calculated masses are likely over- or under-estimates of true masses for each VLP, as associated puffs overlap, leading to misallocation of some SO ₂ ; gray arrows indicate the direction in which the true mass would plot. Arrows indicate direction only and do not indicate the degree of over- or under-estimation. The correlation coefficient for trend line is 0.67.	124

Figure B.1:	Sample of correctly set Matlab working directory file path	128
Figure B.2:	Entry of program name in Matlab command window	129
Figure B.3:	Main GUI interface for UVCamSO ₂ program.....	129
Figure B.4:	Display type menu in image display module	130
Figure B.5:	File selection menu for image display module.....	130
Figure B.6:	Sample calibration cell image, with corresponding concentration path-length values labeled in white (units of ppm·m).....	132
Figure B.7:	Sample entry of calibration cell concentrations, including necessary square brackets.....	133
Figure B.8:	Example of proper selection of the 0 ppm·m calibration cell	134
Figure B.9:	Menu for navigating to colormap editing.....	135
Figure B.10:	Input box for movie creation module.....	136
Figure B.11:	Entry of background image locations, including square brackets	137
Figure B.12:	Entry of background image location and calibration cell values, including square brackets.....	137
Figure B.13:	Prompt for optional time stamp offset.....	138
Figure B.14:	Main input window for ICA processing code.....	140
Figure B.15:	Example of zooming in and selecting a distinct feature on the landscape for image alignment	143
Figure B.16:	Selection of a profile perpendicular to the plume, for a grounded plume	144
Figure B.17:	Selection of background sky for distance correction.....	145
Figure B.18:	Selection of a small section of the darkest portion of the plume for distance correction	145
Figure B.19:	Wait bar that is displayed during processing of images.....	146
Figure B.20:	Sample stack of image profiles, with time increasing to right. Note uniform dark blue section at bottom representing zero values padded on to shorter profiles.....	147
Figure B.21:	Clicking the limit between image information and padded zeros.....	147
Figure B.22:	Sample image stack from Fuego volcano dataset displaying variable background as a result of changing sky conditions and image exposure time.....	148
Figure B.23:	Selecting limit between SO ₂ and background sky	149
Figure B.24:	Selecting bottom of background sky range following delineation of upper limit	150
Figure B.25:	Sample plume speed profile selection	152

Figure B.26:	Screenshot of plume speed code running.....	153
Figure B.27:	Vent location selection for Kilauea volcano imagery	155
Figure B.28:	X-axis selection options in data display module.....	157
Figure B.29:	Sample final plot from data display module.....	158
Figure E.1:	Sample UV image converted to map of concentration path-length of SO ₂ , with sample profile line.....	176
Figure E.2:	Emission rates of SO ₂ (circles) plotted alongside explosion occurrences (vertical gray lines) for (a) 12 January 2009 and (b) 14 January 2009.....	178

LIST OF TABLES

Table 4.1:	Summary of geologic observations of lava high stand events.....	82
Table D.1:	Data file (single filter), 1-100int_notrend734794.5002.txt.....	160
Table D.2:	Metadata file, single filter: 1-100metadata734794.5002.txt.....	161
Table D.3:	Data file, dual filter: 1-100int_notrend_2filt_734794.5347.txt.....	164
Table D.4:	Metadata file, dual filter: 1-100metadata_2filt_734794.5347.txt.....	164
Table D.5:	Data file: 1-100plsp734794.5537.txt.....	168
Table D.6:	Metadata file: 1-100plsp_metadata734794.5537.txt.....	169
Table D.7:	Data file: 1-100backcalc734794.7405.txt.....	171
Table D.8:	Metadata file: 1-100backcalc_metadata734794.7405.txt.....	171
Table D.9:	Data file: 1-100EmRate-kgs734794.7568.txt.....	172
Table D.10:	Metadata file: 1-100EmRate-kgsmetadata734794.7568.txt.....	172

PREFACE

Chapter 2 (including Appendices B, C, and D), while not yet published, has been submitted to *Computers & Geosciences* with P.A. Nadeau and J.L. Palma as co-authors and is in review as of submission of this dissertation. Inclusion in this dissertation is warranted as the entirety of the manuscript was authored by P.A. Nadeau. Likewise, 90+% of the Matlab programming described in the manuscript was completed by P.A. Nadeau.

Chapter 3 (and Appendix E) was previously published as an article in *Geophysical Research Letters* authored by P.A. Nadeau, J.L. Palma, and G.P. Waite. Discussion of the subject with other authors was crucial, but P.A. Nadeau wrote 90+% of the manuscript and completed all of the SO₂ data processing, as well as the majority of the seismic data processing.

Chapter 4 and Appendix A represent parts of larger collaborations, but have not yet been published and the material included in this dissertation has been solely authored by P.A. Nadeau.

ACKNOWLEDGEMENTS

First and foremost, this dissertation would never have been possible without the generous financial support from a number of sources. My funding came primarily from the Remote Sensing for Hazard Mitigation and Resource Protection in Pacific Latin America project (NSF-PIRE 0530109), for which I am very grateful. Travel and field work was also made possible by supplementary funding from two Grants-In-Aid of Research from Sigma Xi, The Scientific Research Society; a Geological Society of America Graduate Student Research Grant; a grant from the Michigan Space Grant Consortium; and a DeVlieg Fellowship awarded through Michigan Technological University. I also benefited from additional travel support from the Graduate Student Government of Michigan Technological University; the Geological and Mining Engineering and Sciences Department of Michigan Technological University; and the Michigan Tech Earth, Planetary and Space Sciences Institute (EPSSI; formerly the Remote Sensing Institute, or RSI).

Despite an entire chapter devoted solely to a Matlab program, this project relied heavily on field work, which would have been impossible to conduct were it not for logistical and field support from many groups and individuals. Many thanks for facilitating work in Guatemala to Rudiger Escobar, John Lyons, INGUAT, and INSIVUMEH. Thanks for assistance with field work goes to Kyle Brill, Gustavo Chigna, Mari Dalton, Jemile Erdem, John Lyons, Josh Richardson, Jesse Silverman, and Elia Tapia. In Hawaii, I thank the National Park Service, Hawaii Volcanoes National Park, and the Hawaiian Volcano Observatory for accommodating me, especially Jeff Sutton, Tamar Elias, and Christine Sealing. I also thank David Fee, Milton Garces, Matt Patrick, Mike Poland, Wes Thelen, Dave Wilson, and Kelly Wooten for facilitating data sharing, and Cindy Werner for loaning an extra UV camera. Ian Brewer, Simon Carn, Elisabet Head, and Cindy Werner are also thanked for their help with data collection at Kilauea.

Work in Nicaragua was made possible with the help of Glyn Williams-Jones and his students and field assistants from Simon Fraser University, Parque Nacional Volcan Masaya, and Carlos Molina Palma and family. Of course, travel anywhere, and many other things, benefitted greatly from the logistical help of Amie Ledgerwood and Kelly McLean of the GMES Department at Michigan Tech.

It has been a love-hate relationship with the UV camera over the past five years, and I never would have made it through without a lot of help along the way. Many thanks to Mari Dalton for being my partner-in-crime, to Jose Luis Palma for helping with the seemingly endless coding task, and to Cindy Werner, Ian Brewer, Matt Watson, Jeremy Shannon, Pete Holland, Christoph Kern, Helen Thomas, and Kelby Hicks for many invaluable UV camera discussions.

I am incredibly thankful to have had Drs. Greg Waite and Simon Carn as my co-advisors. I doubt either one of them expected to have students already waiting for them upon their hiring, but I thank them for taking in an orphaned Ph.D. student and helping to make sure I was able to work on the type of project that I wanted to work on. They have both been immensely helpful along the way, especially during these final stages. I also thank Dr. Bill Rose, one of my committee members, for acting as an interim advisor and for sharing with me his vast knowledge and experience of volcanology. I'm also grateful for my external committee member, Dr. Glyn Williams-Jones, for following up on me after my Masters and seeing me through my Ph.D. While he was not on my committee, I also owe thanks to Dr. Jose Luis Palma. Without formal obligation to my dissertation, he dedicated a lot of time to helping me improve my work. Thanks also to the rest of the geology community at Michigan Tech for enriching my experience over the five years I spent there.

Finally, I would be remiss if I did not express my gratitude to all of my friends, family, and teammates, from Houghton to New York, and everywhere else. There is more to life than a dissertation sometimes; thank you all for helping me keep that in perspective, and for your unfailing support and encouragement over the past five years. A Ph.D. is never easy, but I would have been a lot worse for the wear were it not for all of you.

ABSTRACT

Magmatic volatiles play a crucial role in volcanism, from magma production at depth to generation of seismic phenomena to control of eruption style. Accordingly, many models of volcano dynamics rely heavily on behavior of such volatiles. Yet measurements of emission rates of volcanic gases have historically been limited, which has restricted model verification to processes on the order of days or longer.

UV cameras are a recent advancement in the field of remote sensing of volcanic SO₂ emissions. They offer enhanced temporal and spatial resolution over previous measurement techniques, but need development before they can be widely adopted and achieve the promise of integration with other geophysical datasets. Large datasets require a means by which to quickly and efficiently use imagery to calculate emission rates. We present a suite of programs designed to semi-automatically determine emission rates of SO₂ from series of UV images. Extraction of high temporal resolution SO₂ emission rates via this software facilitates comparison of gas data to geophysical data for the purposes of evaluating models of volcanic activity and has already proven useful at several volcanoes.

Integrated UV camera and seismic measurements recorded in January 2009 at Fuego volcano, Guatemala, provide new insight into the system's shallow conduit processes. High temporal resolution SO₂ data reveal patterns of SO₂ emission rate relative to explosions and seismic tremor that indicate tremor and degassing share a common source process. Progressive decreases in emission rate appear to represent inhibition of gas loss from magma as a result of rheological stiffening in the upper conduit. Measurements of emission rate from two closely-spaced vents, made possible by the high spatial resolution of the camera, help constrain this model.

UV camera measurements at Kilauea volcano, Hawaii, in May of 2010 captured two occurrences of lava filling and draining within the summit vent. Accompanying high lava stands were diminished SO_2 emission rates, decreased seismic and infrasonic tremor, minor deflation, and slowed lava lake surface velocity. Incorporation of UV camera data into the multi-parameter dataset gives credence to the likelihood of shallow gas accumulation as the cause of such events.

Chapter 1: INTRODUCTION

1.1 The role of gas in volcanism

Gases dissolved in magmas are a driving force behind volcanic processes from their initiation deep below the Earth's crust. At subduction zone volcanoes, an influx of water and other volatiles from a subducting, hydrated, oceanic plate to the mantle wedge above induces partial melting. The dissolved volatiles in the melts lead them to be less dense than the surrounding mantle, bringing about the buoyant rise of magma that is a precursor to volcanic activity. Rift and hot-spot volcanoes, where decompression melting induces magmatism, lack the enrichment of water by a subducting slab, but still contain significant dissolved volatiles.

As magma propagates upwards through the crust towards eruption, dissolved volatiles take on a role beyond magma generation: dictating eruption style. The solubilities of the two most prevalent volcanic volatiles, H_2O and CO_2 , in silicate melts relate directly to pressure [e.g., *Shinohara*, 2008]. As buoyant magmas near the surface and ambient pressure decreases, these, and other minor species, eventually reach saturation and begin to exsolve from the melt to create a discrete magmatic gas phase. Crystallization of anhydrous phases may also occur upon magma ascent, enriching the residual melt with volatiles, precipitating further gas exsolution. The behavior of such exsolved gases relative to the surrounding magma is what ultimately dictates eruption style at the surface. Exsolution of gas itself causes an increase in magma viscosity [e.g., *Whittington et al.*, 2000], which may hinder bubble escape. If magma becomes so viscous that bubbles cannot escape and segregate to the top of the magma column, an explosive eruption ensues [e.g., *Namiki and Manga*, 2005]. Likewise, if bulk magma rise rate is such that pressurized bubbles are entrained without escape, violent degassing results [e.g., *Parfitt and Wilson*, 1995]. Conversely, the independent buoyant rise of

bubbles within a magma column may cause mildly explosive (i.e., Strombolian) eruptions [e.g., *Jaupart and Vergnolle*, 1988], quiescent degassing with no magmatic output [e.g., *Stix*, 2007], or quiescent degassing with passive lava effusion [e.g., *Gerlach and Graeber*, 1985].

Aside from surficial eruptive activity, the behavior of bubbles, bubble clouds, and gas slugs in the subsurface influences geophysical phenomena at volcanoes. Long-period seismic events and tremor may occur as a result of resonance in fluid-filled cracks [*Chouet*, 1992] or as a result of bubble coalescence in the shallow magmatic conduit [*Ripepe and Gordeev*, 1999]. Very-long-period seismicity has also been attributed to the movement of gas in the subsurface, including passage of a slug through a change in conduit geometry [*James et al.*, 2006] and the opening of cracks by pressurized gas [*Chouet et al.*, 2005; *Lyons and Waite*, 2011]. Aside from seismicity, transient tilt events at some volcanoes may also be due to subsurface volatiles [*Lyons and Waite*, 2011; *Watson et al.*, 2000].

It may be possible to evaluate models of volcanic activity that implicate gas via integration of geophysical datasets with information regarding amounts of gas released by volcanoes, often a difficult variable to quantify. Some geophysical datasets lend themselves to indirect measurement of volcanic gas emissions: infrasound may be used to quantify the total volume of gas released during an explosion or bubble burst [*Firstov and Kravchenko*, 1996; *Johnson et al.*, 2004], though passively degassed emissions cannot be accounted for in the same manner. Similarly, thermal sensors (i.e., FLIR cameras) can be used to identify periods of increased gas emission, as with puffing [*Ripepe et al.*, 2002], but quantities of gas released cannot be readily determined. More commonly used methods to measure volcanic degassing itself exist and are described below.

1.2 Measurement of volcanic gases

The study of volcanic gases is not straightforward, and has thus typically lagged behind geophysical measurements in terms of usefulness and applicability to synoptic datasets or models of volcanic activity. Still, progress has been made, and continues to be

made since the advent of volcanic gas measurements many years ago. Below are brief summaries of the most common means of measuring volcanic gases, with specific focus on SO_2 . H_2O and CO_2 are proportionately the two dominant gases in volcanic emissions, but are also present in ambient atmosphere in significant amounts, thus making isolation of volcanogenic gas difficult. SO_2 is the easiest of volcanic gases to monitor, as it is the next most abundant volcanic gas after H_2O and CO_2 and is present in the ambient atmosphere in only negligible amounts.

1.2.1 Direct sampling

For over 100 years, scientists observing volcanic activity have collected samples of emitted gases for study. Direct collection of emitted gases themselves was, for many years, the only means by which to glean information about the gases released to the atmosphere by volcanoes. Obtaining these direct samples of volcanic gas is often dangerous; because gas from a magma must pass through and interact with surrounding rock, ground water, and air, volcanologists aim to sample the highest-temperature gas emissions as possible, seen as most representative of magmatic gas. Most often, such gases are emitted in highly active volcanic areas such as active summit craters. Sampling of such gases requires insertion of tubing (quartz or titanium for the highest temperature samples) into active fumaroles and filling evacuated vessels of some sort (e.g., sealed test tubes or specially designed Giggenbach bottles) with samples of gas for further analysis [Giggenbach, 1987]. This method offers only an instantaneous representation of the gas, which can be skewed via contamination by air or gases resulting from hydrothermal activity, but collected over time can yield important insight into changing chemical signatures of volcanic gases. Based on differential solubilities of various gas and elemental species, ratios like CO_2/SO_2 and Cl/S can offer insight into mechanisms of degassing and magma recharge at depth.

In the past decade, multi-gas sensors have been used in lieu of direct fumarole sample. Via electrochemical sensors placed directly in a volcanic plume, open vent plumes,

rather than solely fumarole emissions, may be analyzed [Shinohara, 2005]. Concentrations of species including SO_2 , CO_2 , and H_2O are measured over time, but like fumarole samples, the data yield no information about emission rates of the volcanic gas species.

1.2.2 Satellite measurements

In 1982, when El Chichón Volcano, Mexico erupted in a VEI 5 event, the Total Ozone Mapping Spectrometer (TOMS) instrument, aboard the Nimbus 7 satellite, seemingly detected anomalous amounts of ozone gas over the region [Krueger, 1983]. In actuality, ozone has absorption bands in the ultraviolet (UV) region of the spectrum that overlap those of SO_2 and the sensor was detecting the SO_2 cloud emitted by the eruption. Since then, TOMS and other satellite-based instruments (e.g., Ozone Monitoring Instrument, OMI; Atmospheric Infrared Sounder, AIRS; Advanced Spaceborne Thermal Emission and Reflection Radiometer, ASTER; Moderate Resolution Imaging Spectroradiometer, MODIS; Global Ozone Monitoring Experiment; GOME) have made measurements of SO_2 (and other gases) masses in volcanic clouds by exploiting absorption bands at both UV and infrared (IR) wavelengths [e.g., Carn *et al.*, 2008; Khokhar *et al.*, 2005; Watson *et al.*, 2004]. While the temporal and spatial resolutions of such instruments have improved since TOMS, pixels are still on the order of at least tens of meters, with repeat times of only up to twice per day [Thomas and Watson, 2010]. These specifications thus generally preclude detection of small, passive SO_2 plumes or time-series analysis with respect to short-lived volcanic phenomena, such as individual seismic transients. The Spin Enhanced Visible and Infrared Imager (SEVIRI) does provide SO_2 data every 15 minutes, but is limited to coverage of Europe and Africa [Prata and Kerkmann, 2007].

1.2.3 Ground-based remote sensing

Because of the well-characterized absorption spectrum of SO_2 in the UV range used by TOMS and other UV satellites, measurements can be, and have often been, made via

ground-based UV spectrometers as well. Beginning in the 1970s, this was accomplished with a correlation spectrometer (COSPEC) [Stoiber and Jepsen, 1973; Stoiber *et al.*, 1983]; more recently, newer, more portable Differential Optical Absorption Spectroscopy (DOAS)-based instruments, such as the mini-DOAS [Galle *et al.*, 2003] and the FLYSPEC [Horton *et al.*, 2006] have been used. However, each spectrometer measurement is restricted to a single, one-dimensional profile of the plume, which cannot account for or measure variability within the plume. Such profiles are most commonly measured at some distance from the vent. Between the source vent and the data acquisition site, a number of physical and chemical processes may take place (e.g., conversion to aerosols, deposition, dilution), thereby altering the amount of SO₂ within the plume. Estimations of SO₂ emission rate also rely directly on determination of the speed at which the measured plume propagates, often a difficult parameter to accurately quantify. Furthermore, road traverses with a traditional UV spectrometer generally take upwards of at least 5 minutes (up to an hour, in some cases) and stationary scans last on the order of a minute or two. Accordingly, comparison of SO₂ emission rates and other geophysical datasets has not always been straightforward, as instruments such as seismometers and tiltmeters yield continuous data at 1 Hz or higher, while SO₂ emission rates are generally reported as a handful of emission rates from a few traverses or a single daily mean emission rate. Such datasets of SO₂ emission rates have been used for long term comparison of gas emission and other geophysical parameters [e.g., Watson *et al.*, 2000; Williams-Jones *et al.*, 2001], but low temporal resolution limited the potential for comparison of SO₂ emission rates to distinct geophysical events and types (i.e., deflation-inflation events and tremor).

1.2.3.1 COSPEC

The 1970s saw the advent of correlation spectroscopy, using a few key wavelengths at which SO₂ absorbs, as a means of remotely sensing emission rates of sulfur dioxide (SO₂) [Moffat and Millan, 1971; Stoiber and Jepsen, 1973; Stoiber *et al.*, 1983]. Originally developed as a means to monitor industrial emissions, the COSPEC was quickly adopted by volcanologists.

Chapter 1 - Introduction

The instrument consists of a telescope with a narrow entrance slit; a sequence of collimating, dispersing, and focusing elements; exit masks for specific wavelengths of UV radiation, and a photodetector. Calibration cells containing SO_2 allow for the determination of the dependence of incoming light levels on the known quantities of SO_2 . Diffuse skylight is used as the UV source, with the instrument able to measure concentration path-lengths of SO_2 along the atmospheric path viewed by the instrument. By traversing beneath a volcanic plume or scanning a plume with the COSPEC on a tripod, profiles of SO_2 concentration path-length in the plume can be obtained and subsequently integrated to derive SO_2 emission rates. Via such measurements, the COSPEC provided an increased measure of safety for volcanologist, relative to direct sampling of gases, as measurements could be made kilometers away from any dangerous volcanic activity. Such measurements also yielded information concerning the variability of degassing rates, an improvement over direct samples, but were still limited in their temporal resolution and generally resulted in only a handful of emission rates calculated per day.

1.2.3.2 Miniature DOAS-based spectrometers

The late 1990s and early 2000s saw an improvement over COSPEC with the development of DOAS-based instruments [Galle *et al.*, 2003; Horton *et al.*, 2006] and small, automated scanning DOAS systems with the ability to measure emission rates of SO_2 on time scales of minutes [Edmonds *et al.*, 2003]. The instruments are typically built around small, USB spectrometers from Ocean Optics, and depending on configuration may include a fiber optic cable and telescope attachment, a collimating slit, a scanning attachment, calibration cells, and an integrated GPS unit [Nadeau and Williams-Jones, 2008]. Even including a laptop or netbook computer for instrument control, cost and weight for DOAS-based systems can be on the order of $\sim 10\%$ that of a COSPEC.

The many types of DOAS-based instrumentation offer a variety of improvements over the original COSPEC measurements of volcanic SO_2 emission rates; enhanced

temporal, spectral, and spatial resolutions exist in various combinations [Nadeau and Williams-Jones, 2008], but, ideally, measurements would include an expansive view of the plume and volcanic vent in tandem with a range of spectral information at a rate of ~ 1 Hz or better. I-DOAS offers low-spatial resolution (100×64 pixels) two-dimensional plume imagery over a wide spectral range, but requires a scan through the plume and is therefore not an instantaneous plume view and has a temporal resolution on the order of tens of minutes [Bobrowski *et al.*, 2006]. New wide field-of-view spectrometers also offer ~ 1 Hz data [Boichu *et al.*, 2010; McGonigle *et al.*, 2009] but lack the two dimensional nature that allows for evaluation of plume dynamics. Used together, multiple wide-angle DOAS instruments do, however, provide a means to derive plume speed [Boichu *et al.*, 2010; McGonigle *et al.*, 2009].

1.2.3.3 UV cameras

Recently developed UV cameras [Bluth *et al.*, 2007; Mori and Burton, 2006; Shannon, 2006] address the problematic issues of spectrometer-based measurements, resulting in improved datasets of SO_2 emission rate. The two-dimensional nature of a camera image allows for observation of variations within the plume at a given time. Emissions may be evaluated at the location of the vent in the image rather than downwind. Further, plume speed may be derived by tracking puffs or other features in the plume in a time-series of images. Temporal resolution approaching 1 Hz is a significant improvement on that of traditional spectrometers. While UV photography of SO_2 plumes has been conducted since at least the early 1970s [Klauber, 1973], only recently has the concept been used as a means by which to quantify emission rates of volcanic SO_2 [Bluth *et al.*, 2007; Mori and Burton, 2006]. Such cameras sacrifice the spectral information of a DOAS-based system in favor of a data acquisition rate on the order of 1 Hz and synoptic plume views via ~ 1 Mpx images [Bluth *et al.*, 2007; Mori and Burton, 2006]. Most recently, DOAS-based systems have been integrated into UV camera systems in order to obtain spectral information for a subset of the camera's pixels [e.g., Kern *et al.*, 2010b].

Chapter 1 - Introduction

UV cameras were first used at volcanoes in the mid-2000s and have since been adopted by an increasing number of research groups. Camera systems used thus far for volcanic gas measurement have typically been built around CCD cameras intended for astronomic imaging (Apogee Imaging Systems) [Bluth *et al.*, 2007; Mori and Burton, 2006; Tamburello *et al.*, 2011], though some newer models incorporate Hamamatsu cameras [Prata, 2011]. Lenses are quartz in order to transmit UV radiation and can be of variable focal length, depending on field geometry and targets. To isolate the sector(s) of the UV spectrum in which SO₂ absorbs, bandpass filters are incorporated into the camera system. A single filter (~310 nm center wavelength) is sufficient to identify SO₂ in a volcanic plume but cannot differentiate SO₂ from other absorbing or scattering species. Filters of other wavelengths outside the SO₂ absorption feature can be incorporated into the camera system in order to better isolate the absorption due to SO₂ (Figure 1.1). Any additional filters may be included in a filter wheel on a single camera for successive images with different filters, though this can be problematic in situations with rapidly changing plumes, as the intent is for images taken with different filters to be coregistered. Alternatively, multiple cameras can be used such that they take near-identical field-of-view images simultaneously, with each camera having a different wavelength filter. Slight offsets in the field of view between the two cameras can be easily corrected, allowing for proper alignment of the two images.

Initial work with the UV camera highlighted its potential as a volcano monitoring tool, but focused on individual images rather than sequences, presented different approaches (one vs. two UV bandpass filters), and offered few recommendations for a standard data acquisition methodology [Bluth *et al.*, 2007; Mori and Burton, 2006]. Accuracy and limitations of the UV camera method were not thoroughly addressed. Further testing of the UV camera method was carried out by Dalton *et al.* [2009], which resulted in recommendations for adequate image exposure times and also revealed retrieved SO₂ concentration path-lengths in imagery to be within 30% of independently measured values at a coal-fired power plant. Kern *et al.* [2010b] describe the functionality and limitations of the UV camera, recommending the

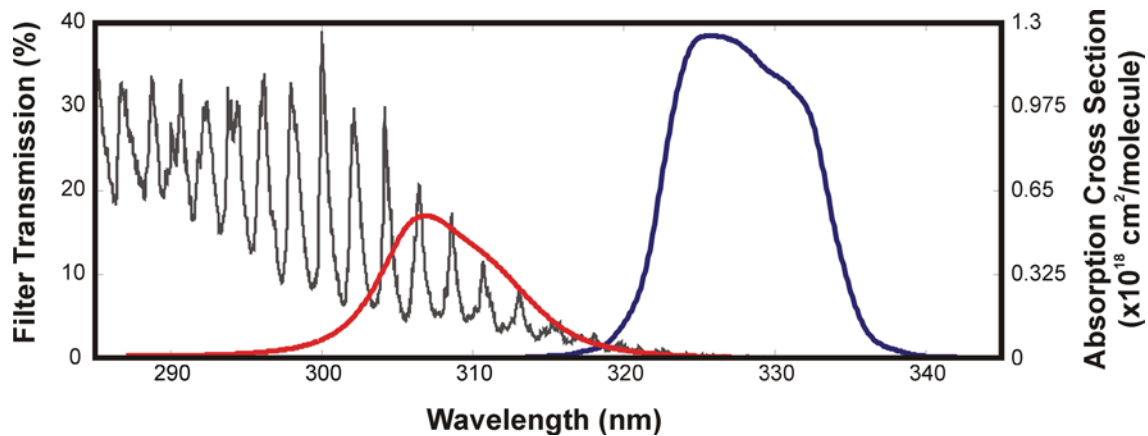


Figure 1.1: UV camera filter response and absorption cross section of SO_2 from 285-345 nm. Gray curve is SO_2 absorption, red curve is 307 nm filter, and blue curve is 326 nm filter. Figure created from data from Vandaele et al. [2009] and Andover Corporation (http://www.andovercorp.com/Web_store/Standard_BP/Std_BP_300nm.php).

integration of a DOAS-based system with the camera in order to achieve more accurate calibration of UV imagery.

Because UV cameras are still a fledgling technology in volcanology, high temporal resolution volcanic gas datasets are just beginning to show their potential in terms of better understanding volcanic activity. Integration of high temporal resolution SO₂ emission rate data with other continuous datasets may be beneficial for understanding of volcanic processes and associated hazards. It has already become possible to detect linkages between seismicity and degassing. A direct correlation between low-frequency seismic tremor and passive SO₂ emissions has been observed at Fuego volcano, Guatemala [Nadeau *et al.*, 2011]. Concurrent UV camera and seismic data at Asama volcano, Japan, also indicate a linkage between very-long-period seismic pulses and eruptive SO₂ emissions [Kazahaya *et al.*, 2011].

UV camera data have also made it possible to distinguish styles of degassing and their relationships to eruption mechanism. At Pacaya volcano, Guatemala, a discrepancy between SO₂ emissions as calculated from infrasound records of Strombolian bubble bursts and those from the UV camera indicated that a significant portion of degassing was a result of a process other than bubble bursts [Dalton *et al.*, 2010]. Via viscosity modeling and analysis of patterns in UV camera data, Holland *et al.* [2011] showed that explosions at Santiaguito volcano, Guatemala, are a result of shear fracturing rather than vent pressurization. In contrast, SO₂ emission rates from UV camera data at Fuego indicate inhibition of gas release prior to ash-rich explosions [Nadeau *et al.*, 2011].

Finally, the spatial resolution of the camera can allow for the extraction of unique SO₂ emission rates from multiple volcanic vents within the same image. Evaluation of UV imagery from Fuego led to the identification of a secondary, non-explosive vent with patterns of degassing that differed from those of the main vent (e.g., more dilute SO₂ to the right of the main puff at the summit in Figure 2b) [Nadeau *et al.*, 2011]. Tamburello *et al.* [2011] used a UV camera in tandem with a multi-gas sensor at the La Fossa fumarole field at Vulcano, Italy and were able to calculate distinct SO₂ emission rate time-series from four

fumarolic areas. Multiplication of the SO_2 emission rates by gas molar ratios from the multi-gas sensor yielded emission rates of H_2O , H_2S , and CO_2 .

1.3 Objectives

It was clear even from promising interdisciplinary studies using older SO_2 measurement techniques that much could be gleaned from studying the relationships between volcanic degassing and volcanic activity as a whole [e.g., *Fischer et al.*, 1994; *Fischer et al.*, 2002; *Watson et al.*, 2000]. Accordingly, SO_2 emission rate data of a higher temporal resolution may prove to be key in better understanding volcanic behavior, and in the longer term, forecasting eruptions and reducing volcanic hazards. To address this issue, work in the Geological and Mining Engineering and Sciences department prior to my arrival at Michigan Tech led to the development of a UV camera for measuring volcanic SO_2 at ~ 1 Hz. Yet a significant hurdle remained before such temporal resolutions could realistically be achieved. Developers of the MTU UV camera collected only individual images or small datasets. Each image was then processed individually to convert raw imagery to SO_2 emission rate, commonly taking upwards of 10 minutes per image and requiring large amounts of user input. At even 0.2 Hz, 8 hours of measurement per day over a two-week field campaign would yield over 75,000 individual images; faster sampling rates, longer days, and longer field campaigns would result in still more prohibitive and unwieldy amounts of data in the absence of an efficient means of data processing. The lack of timely data management and processing hindered the ability of UV cameras to provide an advantage over older measurement techniques in terms of multiparameter studies of volcanic activity.

With both volcanological and data processing questions in mind, upon undertaking my Ph.D. at Michigan Tech in 2007 my objectives were twofold:

- 1) To create a field methodology and semi-automatic suite of programs with which to more easily, quickly, and systematically acquire, display, and process UV

camera imagery such that large datasets collected at 1 Hz could be more easily collected and handled.

- 2) To test UV camera-derived SO₂ emission rates alongside other geophysical data in order to evaluate activity at multiple, diverse volcanoes and develop new models of volcanic behavior, thereby establishing and validating the tool as an advancement in the field of volcanology.

1.4 Study sites

In order to develop a field methodology and data processing program that would be applicable to a range of future datasets collected at a variety of volcanoes, data from Fuego, Pacaya, and Santiaguito volcanoes in Guatemala; Colima and Popocatepetl volcanoes in Mexico; Masaya volcano, Nicaragua; and Kilauea volcano, Hawaii, USA were collected. These were all instrumental in the creation of software for handling UV camera data, but the specific volcanoes were not necessarily relevant to code development. Of these sites, two volcanoes were selected for further study as a means to accomplish the second objective described above. Fuego and Kilauea volcanoes, while both basaltic systems, display exceedingly different morphologies, eruptive styles, and plume composition, among other things. Successful use of the camera at, and application of data from, two such different systems would efficiently demonstrate the relevance of the UV camera as a tool at a wide variety of volcanic systems.

1.4.1 Fuego volcano, Guatemala

1.4.1.1 Geologic setting

Fuego volcano (~3800 m a.s.l.) in Guatemala is one of the many volcanoes lining the western coast of Central America from Guatemala to Panama. This chain of volcanoes, or the Central American Volcanic Front (CAVF), is generated by the oblique subduction of the Cocos tectonic plate in the west beneath the Caribbean plate to the east. The CAVF

comprises a series of laterally offset linear segments of volcanoes $\sim 100 - 300$ km long, with Fuego residing on the central Guatemala segment [Carr *et al.*, 2003]. Fuego itself is a stratovolcano and just one of at least four volcanic centers making up the cross-arc Fuego-Acatenango complex [Chesner and Rose, 1984; Halsor and Rose, 1988]. The southernmost of the centers, Fuego is also the youngest volcano in the complex, and the only that is currently active. While older rocks of the complex are more silicic, historic activity has erupted basalt with high- Al_2O_3 [Chesner and Rose, 1984] and H_2O content ($\sim 3\text{-}5$ wt%) [Roggensack, 2001].

1.4.1.2 Recent volcanic activity

Historical activity at Fuego ranges from subplinian eruptions to persistent lower level activity. A VEI 4 subplinian eruption in 1974 is the most recent large eruption [Rose *et al.*, 1978], and was followed by lower-level Strombolian activity through the rest of the decade [Martin and Rose, 1981]. Infrequent VEI 1-2 explosions occurred from 1980 to 1999; the most recent phase of activity began in 1999 and involves periodic lava flows, Strombolian eruptions, and ashy, degassing explosions [Lyons *et al.*, 2010]. Seismic activity associated with the persistent volcanism is characterized by explosion events; ~ 2 Hz tremor with intermittent harmonic overtones; and other low-frequency events and very-low-frequency events [Lyons *et al.*, 2010; Lyons and Waite, 2011].

In 2009, specifically, continuous but varying passive gas emissions interrupted roughly twice per hour by ash-rich explosions characterized activity during the study. There was no lava extrusion. Explosion onsets ranged from emergence of a single pulse of ash from the summit area, appearing to be driven solely by buoyancy, to momentum-driven jets with sustained pulsing for up to $\sim 1.5 - 2$ minutes. Following an initial explosion onset, ash-rich columns rose buoyantly from the summit area. Explosions were variable in size, and estimated column heights reached a maximum of ~ 500 m above the summit, though strong winds periodically prevented accurate estimations. Increased column height often, but not strictly, corresponded to increased opacity of the column and a darker color; smaller plumes

appeared wispy. Explosions frequently ejected ballistic bombs, which were incandescent at night. The presence of bombs was generally restricted to larger explosions, though not all large explosions ejected bombs. Audible explosion volume varied inconsistently such that three closely-spaced (~ 3 minutes apart) explosions of similar size could consist of two loud explosions bracketing a non-audible one.

1.4.1.3 Previous Studies

Compared with well-studied volcanoes (e.g., Etna, Kilauea), knowledge about Fuego is relatively limited. Petrologic studies following the 1974 subplinian eruption indicated the likely presence of a zoned, elongated magma chamber that contained two mingled magmas and resulted in temporal variability of eruptive products over the course of the eruption [Roggensack, 2001; Rose *et al.*, 1978]. SO_2 emissions associated with the 1974 eruption averaged 4.9 kg/s (423 t/d) [Craddock, 1975], while seismicity recorded prior to and following the eruption included low-frequency events and tremor [McNutt and Harlow, 1983; Yuan *et al.*, 1984].

More attention has been paid to Fuego since the onset of the latest phase of activity in 1999. Berlo *et al.* [2011] analyzed eruptive products from 1999 – 2003 and were able to confirm that the same mingled parent magmas erupted during the 1974 eruption were being erupted nearly three decades later, albeit in a cooler, more differentiated, and volatile-depleted form. They postulate that current activity is driven by an influx of new magma at depth, which will arrive at the surface once residual magma from 1974 has been cleared from the system. SO_2 emissions from 1999 – 2002 were estimated at an average 3.9 kg/s (340 t/d) based on COSPEC measurements by Rodriguez *et al.* [2004]. Johnson *et al.* [2004] describe explosions as Vulcanian on the basis of a prolonged, tremor-like coda following explosion signals in infrasound records. A Vulcanian mechanism was also invoked for the explosions by Marchetti *et al.* [2009] on the basis of integration of infrasound and thermal imagery of ash plumes. Cyclic activity consisting of lava flows and small Strombolian eruptions; larger

paroxysmal eruptions; and ashy, degassing explosions have been identified in recent activity [Lyons *et al.*, 2010], as has a VLP seismicity source ~ 300 m below and ~ 300 m west of the summit crater [Lyons and Waite, 2011].

1.4.2 Kilauea volcano, Hawaii

1.4.2.1 Geologic setting

Kilauea volcano is a basaltic shield (~ 4000 m a.s.l.) volcano on the island of Hawaii, the Eastern-most subaerial volcano on the Eastern-most island in the Hawaiian-Emperor volcanic chain. The chain of volcanoes was formed by motion of the Pacific tectonic plate over a hot spot mantle plume, with ages from Emperor Seamounts indicating the presence of volcanism at the Northwestern end of the chain at 75-80 Ma [Clague and Dalrymple, 1987], and younging to present-day at Kilauea, and nearby Loihi seamount. The onset of volcanism at Kilauea is thought to have been 300,000 – 600,000 years before present, with the earliest subaerial activity occurring at 50,000 – 100,000 years before present (HVO, <http://hvo.wr.usgs.gov/kilauea/>). Kilauea is currently in the late shield-building stage of the general evolutionary trend of Hawaiian volcanoes, from seamount-building, through shield-building, erosional, and atoll/late seamount [Peterson and Moore, 1987].

Kilauea's general structure consists of the summit region with a summit caldera, the East Rift Zone (ERZ), and the Southwest Rift Zone. Seaward of the rift zones is the South flank, which is slowly moving seaward via a series of downstepping faults known as the Koae fault system [Holcomb, 1987]. A well-mixed chamber ~ 2 -4 km beneath the summit comprises the magma reservoir [Garcia *et al.*, 2003]. Upon ascent, magma is frequently injected at shallower levels into the rift zones, such that eruptions can occur either at the summit or along the rifts.

1.4.2.2 Recent volcanic activity

Approximately 90% of the surface of Kilauea consists of rocks younger than 1,100 years old, with ~70% younger than 500 years [Holcomb, 1987]. Historic records of activity date back to 1823, at which time an active lava lake occupied the summit crater. Series of long, sustained summit eruptions dominated the next 100 years, during which the current summit crater, Halema`uma`u, was formed. Retreat of the shallow magma and a series of 17 days of phreatic explosions in Halema`uma`u marked activity in 1924. Following the 1924 summit activity, sporadic and relatively short-lived eruptions took place at both the summit and along the rift zones. The last sustained summit activity of the period took place in mid-1968, following which flank activity began to dominate. Sustained activity along the mid- to upper-East Rift built the parasitic Mauna Ulu shield from 1969-1974. The remainder of the 1970s was marked by intermittent rift zone activity, followed by very brief summit lava flows in 1981 and 1982. In late 1982, magma was injected into the ERZ, culminating in the onset of activity in the mid-ERZ that led to the growth of the Pu`u `O`o cone [Holcomb, 1987, and references therein]. Activity at Pu`u `O`o has persisted since its start in 1983, continuing to this writing in late 2011.

Current activity at Kilauea involves two separate eruption sites. As mentioned, activity at Pu`u `O`o continues, but additionally, the summit region of Kilauea volcano is presently in the midst of its first eruptive activity since 1982 [Wilson *et al.*, 2008]. Following elevated summit tremor and gas emissions in late 2007, the new summit eruption began with the opening of a new gas vent on March 12, 2008 and a small explosive event on March 19, 2008. Activity continues to date with interspersed small ashy explosions, elevated SO₂ emission rates, and glowing vents or a lava lake at variable levels within the new vent (HVO, <http://volcanoes.usgs.gov/hvo/activity/archive.php>). Though lava is periodically visible within the vent, little solid material (juvenile or lithic) has been erupted (< 0.01 km³) [Houghton *et al.*, 2009]; a persistent gas plume indicates that the activity is predominantly a “gas eruption.”

Chapter 1 - Introduction

During the study period (May 2010), shallow magma was sometimes visible (via a webcam stationed on the crater rim) through fume in a small vent within the main Halema`uma`u crater, and a strong gas plume with intermittent ash and elevated SO₂ emission rate persisted (HVO, <http://volcanoes.usgs.gov/hvo/activity/archive.php>). Beginning in mid-May 2010, prolonged periods of elevated lava level within the vent, or high stands, began to occur, with lava remaining high (~15-20 m above base level) in the vent for hours before quickly draining over a period of only minutes. Both the summit and the rift zone degassed persistently; exhibited tremor, and experienced sporadic inflation and deflation (HVO, <http://volcanoes.usgs.gov/hvo/activity/archive.php>).

1.4.2.3 Previous and Relevant Studies

The near-constant activity and accessibility of Kilauea, along with the presence of the Hawaiian Volcano Observatory (HVO) at its summit has made the volcano an ideal location for the study of many aspects of basaltic volcanism. Eruption sites along the ERZ and, more recently, in the summit caldera have each been studied in depth; some key findings are summarized below.

1.4.2.3.1 Gas studies at Kilauea

Direct sampling of volcanic gas at Kilauea led to the identification of a two-stage degassing process and the classification of two main types of gases at Kilauea. Type I gases, emitted at the summit, represent a deep-sourced CO₂-rich (C/S = ~4) chamber gas that has equilibrated with magma stored in the summit chamber, while CO₂-poor type II gases are released along the ERZ and represent the second of a two-stage degassing process whereby magma already depleted in CO₂ via summit degassing is injected into the ERZ where it releases more soluble SO₂ and H₂O [Gerlach and Graeber, 1985]. HVO staff makes frequent measurements of SO₂ emission rate at both the summit and ERZ eruption sites, as well as occasional CO₂ emission rate measurements at the summit. Average SO₂ emission rates for 2003-2007 for the summit and ERZ were, respectively, 140 t/d and 1700 t/d; summit

emission rates from early 2010, as reported by HVO, were variable but highly elevated ($\sim 1000 - 2000$ t/d) and ERZ emissions were somewhat less than the 2003-2007 average ($\sim 750 - 1000$ t/d), but are variable as well (HVO, <http://volcanoes.usgs.gov/hvo/activity/archive.php>).

Other gases at Kilauea have been sporadically measured using Fourier Transform Infrared Spectroscopy (FTIR) [McGee and Gerlach, 1998; McGee *et al.*, 2005], though mostly for quantification of emission rates of subordinate volatile species such as CO, HCl, and HF [McGee *et al.*, 2005] that degas at very shallow levels [Edmonds *et al.*, 2009]. Edmonds and Gerlach [2007] obtained FTIR data for three distinct types of vapor loss at Pu'u 'O'o and were able to distinguish between large, CO₂-rich bubbles (gas piston events) sourced at depth and small, H₂O-rich bubbles (spattering) that formed in a shallower portion of the conduit.

1.4.2.3.2 Seismo-acoustic studies at Kilauea

At the summit of Kilauea, Kumagai *et al.* [2005] used a dense array of broadband seismometers to characterize the source of long-period (LP) events. Waveform inversions and modeling indicated that the source of the event was likely a resonating crack filled with fluid (bubbly water or steam) at a depth of ~ 150 m on the rim of Halema'uma'u crater. Increased heat from below, leading to fluid discharge, and associated vibrations are invoked as the driving force behind the event. Hydrothermal origins for tremor and LP events were also indicated by array analysis of summit seismicity by Almendros *et al.* [2001]. Three zones of LP event generation in the vicinity of Halema'uma'u were identified, with the most shallow (< 200 m below caldera floor) also found to be the source of tremor. A resonating, fluid-filled crack was again the best fit for the data, with heated gases from depth suggested to be the cause of excitation in the hydrothermal system. Deeper (5-15 km) LP events also occur, have a weak high-frequency onset, and were suggested to be evidence of a trigger event (e.g., rock fracturing by pressurized magma) causing resonance in a magma-filled volume [Battaglia *et al.*, 2003].

Chapter 1 - Introduction

It is important to note that previous studies of summit activity were conducted at times when there was no surficial eruptive activity. Given the summit's current lava-filled vent, studies of the active vents at Pu'u 'O'o may be more analogous to current activity at Halema'uma'u. The most recent seismic array analysis at Pu'u 'O'o was carried out by *Goldstein and Chouet* [1994]. Results of the installation of two dense seismic arrays indicated that the highest seismic amplitudes were correlated with the highest bubble-bursting activity (gas pistoning). Data were best fit by a model of a point-source or resonating crack located within or near the surficial layers of Pu'u 'O'o, at a maximum depth of ~ 1 km. It was also found that spectra of such point sources are depth-sensitive, leading to the possibility that source depth variations may be tracked from a single record.

Garcés et al. [2003] collected infrasonic data at Pu'u 'O'o for nine days in late 2002. Two microphones were placed on the crater rim, with another 4-element array ~ 2 km away in a small kipuka. Both sets of instruments detected significant tremor from 1-10 Hz, with no identifiable transient signals aside from air traffic and earthquakes. The high tremor amplitude and extension of source azimuth directions down the lava tube system at the base of Pu'u 'O'o led to the interpretation that tremor is near to the surface, consistent with the work of *Goldstein and Chouet* [1994]. *Fee and Garcés* [2007] conducted a similar experiment in 2005 and identified similar infrasonic tremor in the 0.5-3 Hz band. Sources from arrival azimuths appeared to be predominantly from Pu'u 'O'o, with a much smaller lava tube component than found by *Garcés et al.* [2003]. Diurnal variations in tremor spectral amplitudes were noted, indicating that wind and other tropospheric changes can affect ambient noise, signal-to-noise ratios, and detectability [*Fee and Garcés*, 2007].

Most recently, studies of seismicity at Kilauea have focused on very long period (VLP) events associated with the summit activity. *Chouet et al.* [2010], *Fee et al.* [2010], and *Patrick et al.* [2011b] examine ashy “degassing bursts” within the summit vent and the simultaneous occurrence of VLP signals in both the seismic and infrasonic records. While *Chouet et al.* [2010] contend that VLPs associated with the bursts are triggered by the

response of the shallow magma conduit to the passage and bursting of a large gas slug, *Patrick et al.* [2011b] utilize video records in conjunction with seismic records to implicate conduit response to the violent release of a shallow accumulated layer of gas as the cause of the VLPs. Smaller, episodic tremor bursts are also thought to be caused by the release of accumulated gas [*Patrick et al.*, 2011b]. Interpretation of infrasonic records by *Fee et al.* [2010] does not favor one degassing burst model over the other, but does indicate that infrasonic tremor from the summit vent is the result of Helmholtz resonance in a large, subsurface cavity.

1.4.2.3.3 Integration of gas and geophysics at Kilauea

Despite the wealth of data collected by HVO and independent researchers, little has been done to evaluate relationships between seismicity and outgassing. *Sutton et al.* [2001] found a positive relationship between summit SO₂ emission rates and the occurrence of shallow, short-period seismic events within the summit caldera of Kilauea during the period of constant lava effusion from mid-1986 to 1998. Rather than a fluid-source and ensuing long-period seismicity that correlates with SO₂ emissions, the short-period events were interpreted as tectonic response to magma pressure changes, with a gradual decline of both event number and SO₂ emission rate representing structural maturation of the dike system between the summit and the ERZ. A period of positive correlation from 1992-1998 between ERZ SO₂ emissions and upper- to mid-ERZ seismicity was also noted.

More recently, *Edmonds and Gerlach* [2007] used solubility models for H₂O and CO₂ to determine that gas released during gas piston events at Pu'u 'Ō'o were slugs that had equilibrated with melt at depths of 600-900 m, consistent with the tremor depths found by *Goldstein and Chouet* [1994].

Given the reliance on gas of recent models for VLP events as they relate to current summit activity, it is of note that none of the studies addressing the models involve measurements of gas emission itself.

1.5 Dissertation format

The UV camera is a fledgling technology in the field of volcanology. As such, knowledge and usage of it as a tool in volcano studies and monitoring efforts is rapidly evolving. In order to keep pace with the state-of-the-art and to keep interested parties apprised of my work, chapters in this dissertation have been written as independent journal manuscripts. With the increasing popularity of UV cameras as a means of measuring SO₂ emission rates, a need for a standard means of image processing and, accordingly, software to undertake such processing arose. A manuscript comprising Chapter 2, Appendix B, and Appendix C was recently submitted to *Computers & Geosciences* and is currently under review. Pending publication, the article and its associated computer program will provide a platform for UV camera users worldwide to process data in a consistent manner. Chapter 3 (including Appendix D) has already been published in *Geophysical Research Letters* and includes the first documentation of a direct link between low-frequency volcanic tremor and SO₂ emissions, noted on a time scale of seconds. Chapter 4 and Appendix A further highlight the usefulness of UV camera data alongside other geophysical datasets. Each will be submitted as, or as part of, a publication in coming months. Because of the nature of chapters as stand-alone journal articles, some repetition between chapters is unavoidable, especially in instances of background information and methodology.

1.6 References

- Almendros, J., B. Chouet, and P. Dawson (2001), Spatial extent of a hydrothermal system at Kilauea Volcano, Hawaii, determined from array analyses of shallow long-period seismicity - 1. Method, *Journal of Geophysical Research-Solid Earth*, 106(B7), 13565-13580.
- Battaglia, J., J.-L. Got, and P. Okubo (2003), Location of long-period events below Kilauea Volcano using seismic amplitudes and accurate relative relocation, *Journal of Geophysical Research*, 108(B12), 2553.
- Berlo, K., J. Stix, K. Roggensack, and B. Ghaleb (2011), A tale of two magmas, Fuego, Guatemala, *Bulletin of Volcanology*, 1-14.

Chapter 1 - Introduction

- Bluth, G. J. S., J. M. Shannon, I. M. Watson, A. J. Prata, and V. J. Realmuto (2007), Development of an ultra-violet digital camera for volcanic SO₂ imaging, *Journal of Volcanology and Geothermal Research*, 161(1-2), 47-56.
- Bobrowski, N., G. Hönniger, F. Lohberger, and U. Platt (2006), IDOAS: A new monitoring technique to study the 2D distribution of volcanic gas emissions, *Journal of Volcanology and Geothermal Research*, 150(4), 329-338.
- Boichu, M., C. Oppenheimer, V. Tsanev, and P. R. Kyle (2010), High temporal resolution SO₂ flux measurements at Erebus volcano, Antarctica, *Journal of Volcanology and Geothermal Research*, 190(3-4), 325-336.
- Carn, S. A., A. J. Krueger, S. Arellano, N. A. Krotkov, and K. Yang (2008), Daily monitoring of Ecuadorian volcanic degassing from space, *Journal of Volcanology and Geothermal Research*, 176(1), 141-150.
- Carr, M. J., M. D. Feigenson, L. C. Patino, and J. A. Walker (2003), Volcanism and geochemistry in Central America: Progress and problems, in *Inside the Subduction Factory*, edited by J. Eiler, pp. 153-174, AGU, Washington, D.C.
- Chesner, C. A., and W. I. Rose (1984), Geochemistry and evolution of the fuego volcanic complex, Guatemala, *Journal of Volcanology and Geothermal Research*, 21(1-2), 25-44.
- Chouet, B. A. (1992), A seismic model for the source of long-period events and harmonic tremor, in *Volcanic Seismology*, edited by P. Gasparini, R. Scarpa and K. Aki, pp. 133-156, Springer, New York.
- Chouet, B. A., P. Dawson, and A. Arciniega-Ceballos (2005), Source mechanism of Vulcanian degassing at Popocatepetl Volcano, Mexico, determined from waveform inversions of very long period signals, *Journal of Geophysical Research*, 110(B7), B07301.
- Chouet, B. A., P. B. Dawson, M. R. James, and S. J. Lane (2010), Seismic source mechanism of degassing bursts at Kilauea Volcano, Hawaii: Results from waveform inversion in the 10-50 s band, *Journal of Geophysical Research*, 115(B9), B09311.
- Clague, D. A., and G. B. Dalrymple (1987), The Hawaiian-Emperor Volcanic Chain - Part I: Geologic Evolution, in *Volcanism in Hawaii*, U.S. Geological Survey Professional Paper 1350, pp. 5-54.
- Crafford, T. (1975), SO₂ emission of the 1974 eruption of Volcán Fuego, Guatemala, *Bulletin of Volcanology*, 39(4), 536-556.
- Dalton, M. P., I. M. Watson, P. A. Nadeau, C. Werner, W. Morrow, and J. M. Shannon (2009), Assessment of the UV camera sulfur dioxide retrieval for point source plumes, *Journal of Volcanology and Geothermal Research*, 188(4), 358-366.

Chapter 1 - Introduction

- Dalton, M. P., G. P. Waite, I. M. Watson, and P. A. Nadeau (2010), Multiparameter quantification of gas release during weak Strombolian eruptions at Pacaya Volcano, Guatemala, *Geophysical Research Letters*, 37(9), L09303.
- Edmonds, M., R. A. Herd, B. Galle, and C. M. Oppenheimer (2003), Automated, high time-resolution measurements of SO₂ flux at Soufrière Hills Volcano, Montserrat, *Bulletin of Volcanology*, 65(8), 578-586.
- Edmonds, M., and T. M. Gerlach (2007), Vapor segregation and loss in basaltic melts, *Geology*, 35(8), 751-754.
- Edmonds, M., T. M. Gerlach, and R. A. Herd (2009), Halogen degassing during ascent and eruption of water-poor basaltic magma, *Chemical Geology*, 263(1-4), 122-130.
- Fee, D., and M. Garcés (2007), Infrasonic tremor in the diffraction zone, *Geophys. Res. Lett.*, 34(16), L16826.
- Fee, D., M. Garcés, M. Patrick, B. Chouet, P. Dawson, and D. Swanson (2010), Infrasonic harmonic tremor and degassing bursts from Halema'uma'u Crater, Kilauea Volcano, Hawaii, *J. Geophys. Res.*, 115(B11), B11316.
- Firstov, P. P., and N. M. Kravchenko (1996), Estimation of the amount of explosive gas release in volcanic eruptions using airwaves, *Volcanology & Seismology*, 17(4-5), 547-560.
- Fischer, T. P., M. M. Morrissey, M. L. Calvache, D. Gomez, R. Torres, J. Stix, and S. N. Williams (1994), Correlations between SO₂ flux and long-period seismicity at Galeras Volcano, *Nature*, 368(6467), 135-137.
- Fischer, T. P., K. Roggensack, and P. R. Kyle (2002), Open and almost shut case for explosive eruptions: Vent processes determined by SO₂ emission rates at Karymsky volcano, Kamchatka, *Geology*, 30(12), 1059-1062.
- Galle, B., C. Oppenheimer, A. Geyer, A. J. S. McGonigle, M. Edmonds, and L. Horrocks (2003), A miniaturised ultraviolet spectrometer for remote sensing of SO₂ fluxes: a new tool for volcano surveillance, *Journal of Volcanology and Geothermal Research*, 119(1-4), 241-254.
- Garcés, M., A. Harris, C. Hetzer, J. B. Johnson, S. Rowland, E. Marchetti, and P. Okubo (2003), Infrasonic tremor observed at Kilauea Volcano, Hawai'i, *Geophysical Research Letters*, 30(20), 2023.
- Garcia, M. O., A. J. Pietruszka, and J. M. Rhodes (2003), A Petrologic Perspective of Kilauea Volcano's Summit Magma Reservoir, *Journal of Petrology*, 44(12), 2313-2339.

Chapter 1 - Introduction

- Gerlach, T. M., and E. J. Graeber (1985), Volatile budget of Kilauea volcano, *Nature*, 313(6000), 273-277.
- Giggenbach, W. F. (1987), Redox processes governing the chemistry of fumarolic gas discharges from White Island, New Zealand, *Applied Geochemistry*, 2(2), 143-161.
- Goldstein, P., and B. Chouet (1994), Array Measurements and Modeling of Sources of Shallow Volcanic Tremor at Kilauea Volcano, Hawaii, *Journal of Geophysical Research-Solid Earth*, 99(B2), 2637-2652.
- Halsor, S. P., and W. I. Rose (1988), Common Characteristics of Paired Volcanoes in Northern Central America, *Journal of Geophysical Research*, 93(B5), 4467-4476.
- Holcomb, R. T. (1987), Eruptive History and Long-Term Behavior of Kilauea Volcano, in Volcanism in Hawaii, U.S. Geological Survey Professional Paper 1350, pp. 261-350.
- Holland, A. S. P., I. M. Watson, J. C. Phillips, L. Caricchi, and M. P. Dalton (2011), Degassing processes during lava dome growth: Insights from Santiaguito lava dome, Guatemala, *Journal of Volcanology and Geothermal Research*, 202(1-2), 153-166.
- Horton, K. A., G. Williams-Jones, H. Garbeil, T. Elias, A. J. Sutton, P. Mouginis-Mark, J. N. Porter, and S. Clegg (2006), Real-time measurement of volcanic SO₂ emissions: validation of a new UV correlation spectrometer (FLYSPEC), *Bulletin of Volcanology*, 68(4), 323-327.
- Houghton, B. F., D. A. Swanson, and R. J. Carey (2009), Products of short-lived pyroclastic events during the 2008-2009 Halema`uma`u eruption, Kilauea: Implications for eruption process and hazards, *Geological Society of America Abstracts with Programs*, 41(7), 231.
- James, M. R., S. J. Lane, and B. A. Chouet (2006), Gas slug ascent through changes in conduit diameter: Laboratory insights into a volcano-seismic source process in low-viscosity magmas, *Journal of Geophysical Research*, 111(B5), B05201.
- Jaupart, C., and S. Vergnolle (1988), Laboratory models of Hawaiian and Strombolian eruptions, *Nature*, 331(6151), 58-60.
- Johnson, J. B., R. C. Aster, and P. R. Kyle (2004), Volcanic eruptions observed with infrasound, *Geophysical Research Letters*, 31(14), L14604.
- Kazahaya, R., T. Mori, M. Takeo, T. Ohminato, T. Urabe, and Y. Maeda (2011), Relation between single very-long-period pulses and volcanic gas emissions at Mt. Asama, Japan, *Geophysical Research Letters*, 38(11), L11307.

Chapter 1 - Introduction

- Kern, C., F. Kick, P. Lübcke, L. Vogel, M. Wöhrbach, and U. Platt (2010b), Theoretical description of functionality, applications, and limitations of SO₂ cameras for the remote sensing of volcanic plumes, *Atmospheric Measurement Techniques*, 3(3), 733-749.
- Khokhar, M. F., C. Frankenberg, M. Van Roozendaal, S. Beirle, S. Köhl, A. Richter, U. Platt, and T. Wagner (2005), Satellite observations of atmospheric SO₂ from volcanic eruptions during the time-period of 1996–2002, *Advances in Space Research*, 36(5), 879-887.
- Klauber, G. M. (1973), Ultraviolet photography of sulfur dioxide plumes, *Environmental Science & Technology*, 7(10), 953-954.
- Krueger, A. J. (1983), Sighting of El Chichón sulfur dioxide clouds with the Nimbus 7 Total Ozone Mapping Spectrometer, *Science*, 220(4604), 1377-1379.
- Kumagai, H., B. A. Chouet, and P. B. Dawson (2005), Source process of a long-period event at Kilauea volcano, Hawaii, *Geophysical Journal International*, 161(1), 243-254.
- Lyons, J. J., G. P. Waite, W. I. Rose, and G. Chigna (2010), Patterns in open vent, strombolian behavior at Fuego volcano, Guatemala, 2005-2007, *Bulletin of Volcanology*, 72(1), 1-15.
- Lyons, J. J., and G. P. Waite (2011), Dynamics of explosive volcanism at Fuego volcano imaged with very long period seismicity, *Journal of Geophysical Research*, 116(B9), B09303.
- Marchetti, E., M. Ripepe, A. J. L. Harris, and D. Delle Donne (2009), Tracing the differences between Vulcanian and Strombolian explosions using infrasonic and thermal radiation energy, *Earth and Planetary Science Letters*, 279(3-4), 273-281.
- Martin, D. P., and W. I. Rose (1981), Behavioral patterns of Fuego volcano, Guatemala, *Journal of Volcanology and Geothermal Research*, 10(1-3), 67-81.
- McGee, K. A., and T. M. Gerlach (1998), Airborne volcanic plume measurements using a FTIR spectrometer, Kilauea Volcano, Hawaii, *Geophysical Research Letters*, 25(5), 615-618.
- McGee, K. A., T. Elias, A. J. Sutton, M. P. Doukas, P. G. Zemek, and T. M. Gerlach (2005), Reconnaissance gas measurements on the East Rift Zone of Kilauea volcano, Hawai'i by Fourier transform infrared spectroscopy, U.S. Geological Survey Open File Report 2005-1062.
- McGonigle, A. J. S., A. Aiuppa, M. Ripepe, E. P. Kantzas, and G. Tamburello (2009), Spectroscopic capture of 1 Hz volcanic SO₂ fluxes and integration with volcano geophysical data, *Geophysical Research Letters*, 36, L21309.

Chapter 1 - Introduction

- McNutt, S., and D. Harlow (1983), Seismicity at Fuego, Pacaya, Izalco, and San Cristobal Volcanoes, Central America, 1973–1974, *Bulletin of Volcanology*, 46(3), 283-297.
- Moffat, A. J., and M. M. Millan (1971), The applications of optical correlation techniques to the remote sensing of SO₂ plumes using sky light, *Atmospheric Environment*, 5(8), 677-690.
- Mori, T., and M. Burton (2006), The SO₂ camera: A simple, fast and cheap method for ground-based imaging of SO₂ in volcanic plumes, *Geophysical Research Letters*, 33(24), L24804.
- Nadeau, P. A., and G. Williams-Jones (2008), Beyond COSPEC - Recent advances in SO₂ monitoring technology, in *The COSPEC Cookbook: Making SO₂ Measurements at Active Volcanoes*, edited by G. Williams-Jones, J. Stix and C. Hickson, pp. 219-233, IAVCEI.
- Nadeau, P. A., J. L. Palma, and G. P. Waite (2011), Linking volcanic tremor, degassing, and eruption dynamics via SO₂ imaging, *Geophysical Research Letters*, 38(1), L01304.
- Namiki, A., and M. Manga (2005), Response of a bubble bearing viscoelastic fluid to rapid decompression: Implications for explosive volcanic eruptions, *Earth and Planetary Science Letters*, 236(1-2), 269-284.
- Parfitt, E. A., and L. Wilson (1995), Explosive volcanic eruptions-IX. The transition between Hawaiian-style lava fountaining and Strombolian explosive activity, *Geophysical Journal International*, 121(1), 226-232.
- Patrick, M. R., D. Wilson, D. Fee, T. Orr, and D. Swanson (2011b), Shallow degassing events as a trigger for very-long-period seismicity at Kilauea Volcano, Hawai'i, *Bulletin of Volcanology*, 1-8.
- Peterson, D. W., and R. B. Moore (1987), Geologic history and evolution of geologic concepts, Island of Hawaii, in *Volcanism in Hawaii*, U.S. Geological Survey Professional Paper 1350, pp. 149-189.
- Prata, A. J., and J. Kerkmann (2007), Simultaneous retrieval of volcanic ash and SO₂ using MSG-SEVIRI measurements, *Geophysical Research Letters*, 34(5), L05813.
- Prata, A. J. (2011), UV Ground-based imaging camera: EnviCam, presented at Open Vent Volcanoes PASI Workshop, San Jose, Costa Rica, 15 January 2011.
- Ripepe, M., and E. Gordeev (1999), Gas bubble dynamics model for shallow volcanic tremor at Stromboli, *Journal of Geophysical Research-Solid Earth*, 104(B5), 10639-10654.

Chapter 1 - Introduction

- Ripepe, M., A. J. L. Harris, and R. Carniel (2002), Thermal, seismic and infrasonic evidences of variable degassing rates at Stromboli volcano, *Journal of Volcanology and Geothermal Research*, 118(3-4), 285-297.
- Rodriguez, L. A., I. M. Watson, W. I. Rose, Y. K. Branan, G. J. S. Bluth, G. Chigna, O. Matias, D. Escobar, S. A. Carn, and T. P. Fischer (2004), SO₂ emissions to the atmosphere from active volcanoes in Guatemala and El Salvador, 1999-2002, *Journal of Volcanology and Geothermal Research*, 138(3-4), 325-344.
- Roggensack, K. (2001), Unraveling the 1974 eruption of Fuego volcano (Guatemala) with small crystals and their young melt inclusions, *Geology*, 29(10), 911-a-914.
- Rose, W. I., A. T. Anderson, L. G. Woodruff, and S. B. Bonis (1978), October 1974 basaltic tephra from Fuego Volcano - Description and history of the magma body, *Journal of Volcanology and Geothermal Research*, 4(1-2), 3-53.
- Shannon, J. M. (2006), Development and application of new techniques for sulfur dioxide monitoring at active volcanoes, Michigan Technological University, Houghton, Michigan.
- Shinohara, H. (2005), A new technique to estimate volcanic gas composition: plume measurements with a portable multi-sensor system, *Journal of Volcanology and Geothermal Research*, 143(4), 319-333.
- Shinohara, H. (2008), Excess degassing from volcanoes and its role on eruptive and intrusive activity, *Reviews of Geophysics*, 46(4), RG4005.
- Stix, J. (2007), Stability and instability of quiescently active volcanoes: The case of Masaya, Nicaragua, *Geology*, 35(6), 535-538.
- Stoiber, R. E., and A. Jepsen (1973), Sulfur dioxide contributions to the atmosphere by volcanoes, *Science*, 182(4112), 577-578.
- Stoiber, R. E., L. L. Malinconico, and S. N. Williams (1983), Use of the correlation spectrometer at volcanoes, in *Forecasting volcanic events*, edited by H. Tazieff and J. C. Sabroux, pp. 424-444, Elsevier, New York.
- Sutton, A. J., T. Elias, T. M. Gerlach, and J. B. Stokes (2001), Implications for eruptive processes as indicated by sulfur dioxide emissions from Kilauea Volcano, Hawaii, 1979-1997, *Journal of Volcanology and Geothermal Research*, 108(1-4), 283-302.
- Tamburello, G., E. P. Kantzas, A. J. S. McGonigle, A. Aiuppa, and G. Giudice (2011), UV camera measurements of fumarole field degassing (La Fossa crater, Vulcano Island), *Journal of Volcanology and Geothermal Research*, 199(1-2), 47-52.

Chapter 1 - Introduction

- Thomas, H., and I. Watson (2010), Observations of volcanic emissions from space: current and future perspectives, *Natural Hazards*, 54(2), 323-354.
- Vandaele, A. C., C. Hermans, and S. Fally (2009), Fourier transform measurements of SO₂ absorption cross sections: II.: Temperature dependence in the 29000–44000 cm⁻¹ (227–345 nm) region, *Journal of Quantitative Spectroscopy and Radiative Transfer*, 110(18), 2115-2126.
- Watson, I. M., C. Oppenheimer, B. Voight, P. W. Francis, A. Clarke, J. Stix, A. Miller, D. M. Pyle, M. R. Burton, S. R. Young, G. Norton, S. Loughlin, and B. Darroux (2000), The relationship between degassing and ground deformation at Soufriere Hills Volcano, Montserrat, *Journal of Volcanology and Geothermal Research*, 98(1-4), 117-126.
- Watson, I. M., V. J. Realmuto, W. I. Rose, A. J. Prata, G. J. S. Bluth, Y. Gu, C. E. Bader, and T. Yu (2004), Thermal infrared remote sensing of volcanic emissions using the moderate resolution imaging spectroradiometer, *Journal of Volcanology and Geothermal Research*, 135(1-2), 75-89.
- Whittington, A., P. Richet, and F. Holtz (2000), Water and the viscosity of depolymerized aluminosilicate melts, *Geochimica Et Cosmochimica Acta*, 64(21), 3725-3736.
- Williams-Jones, G., J. Stix, M. Heiligmann, J. Barquero, E. Fernandez, and E. D. Gonzalez (2001), A model of degassing and seismicity at Arenal Volcano, Costa Rica, *Journal of Volcanology and Geothermal Research*, 108(1-4), 121-139.
- Wilson, D., T. Elias, T. Orr, M. Patrick, J. Sutton, and D. Swanson (2008), Small Explosion From New Vent at Kilauea's Summit, *Eos Transactions American Geophysical Union*, 89(22), 203.
- Yuan, A. T. E., S. R. McNutt, and D. H. Harlow (1984), Seismicity and eruptive activity at Fuego Volcano, Guatemala: February 1975 –January 1977, *Journal of Volcanology and Geothermal Research*, 21(3-4), 277-296.

Chapter 2: A MATLAB PROGRAM FOR DERIVING EMISSION RATES OF VOLCANIC SO₂ FROM UV IMAGERY*

2.1 Abstract

UV cameras are a recent advancement in the field of remote sensing of volcanic SO₂ emissions, offering enhanced temporal and spatial resolution over previous measurement techniques. Datasets can become prohibitively large and thus require a means by which to quickly and efficiently use imagery to calculate emission rates. We present a suite of programs designed to not only semi-automatically determine emission rates of SO₂ from series of UV images, but also to facilitate data analysis through inspection of individual images, creation of video files from images, and display of previously processed data. Extraction of high temporal resolution SO₂ emission rates via this program facilitates comparison of gas data to geophysical data for the purposes of evaluating models of volcanic activity and has already proven useful at several volcanoes. Results obtained via this program are in agreement with data from traditional measurement techniques.

2.2 Introduction

Gases dissolved in magmas are the driving force behind volcanic eruptions and their behavior can dictate the style and explosivity of eruptions [Jaupart and Vergnolle, 1988; Parfitt and Wilson, 1995]. Measurement of gases emitted by volcanoes can therefore yield crucial information about a volcano's activity. Sulfur dioxide (SO₂) is the third most abundant gas species in most volcanic emissions and the most abundant gas that is present at negligible

* This chapter, along with Appendices B, C, and D, is in review as:
Nadeau, P. A. and Palma, J.L., A Matlab Program for Deriving Emission Rates of Volcanic SO₂ from UV imagery. *Computers & Geosciences*.

Chapter 2 – UVCamSO₂ Program

levels in the ambient atmosphere, which makes its identification and measurement as a volcanic gas straightforward relative to other species such as water and carbon dioxide. While direct sampling of volcanic gas is possible, SO₂ has been measured remotely since the 1970s [Stoiber and Jepsen, 1973; Stoiber *et al.*, 1983] by exploitation of its absorption bands in the ultraviolet (UV) range of wavelengths. Instruments such as COSPEC, FLYSPEC, and other UV spectrometers [Elias *et al.*, 2006; Galle *et al.*, 2003; Horton *et al.*, 2006; Stoiber *et al.*, 1983] are the established means of measuring SO₂ emission rates at volcanoes. Such measurements have been used to interpret volcanic activity worldwide, greatly contributing to eruption forecasting and a better understanding of subsurface magmatic processes [e.g., Fischer *et al.*, 1994; Palma *et al.*, 2011; Watson *et al.*, 2000].

Recently developed UV camera systems [e.g., Bluth *et al.*, 2007; Mori and Burton, 2006] build on traditional remote sensing of volcanic SO₂ by offering synoptic views of plumes, allowing a better tracking of variations in gas emissions at a much higher temporal resolution (~ 1 Hz) than previous methods. These improvements allow direct comparison of SO₂ emissions with other geophysical datasets of high temporal resolution and have already proven valuable in assessing volcanic degassing as it relates to generation of infrasound and seismicity [e.g., Dalton *et al.*, 2010; Nadeau *et al.*, 2011].

In order for the ~ 1 Hz temporal resolution of the UV camera datasets to be realistically realized, a means for handling and processing large amounts of imagery is necessary. A single day of measurements may yield over 10,000 images; full field campaigns would result in unwieldy amounts of data in the absence of an efficient means of data management. Accordingly, automation of UV image processing is needed, and it may also prove important if volcano observatories adopt UV cameras for volcano surveillance in the future. This paper describes the algorithms used in a MATLAB program (UVCamSO₂) developed to quickly and semi-automatically derive emission rates of volcanic SO₂ from time-series of UV imagery. The program can accommodate data from one or two bandpass

filters simultaneously, and has already proven useful in multiple interdisciplinary studies [Dalton *et al.*, 2010; Nadeau *et al.*, 2011].

2.3 Methodology and algorithms

The UV camera system used for this code development consists of an Apogee Alta U6 camera with a Kodak KAF-1001E-2 1024×1024 pixel CCD. We outfitted the camera with a 105 mm CoastalOpt UV lens (angular field of view, 13.3578°) and a 10 nm FWHM (full width, half-max) bandpass filter centered at 307 nm from Andover Optics. For dual-filter imaging, we used a second, identical camera with a bandpass filter centered at 326 nm. The two cameras were attached to a single metal fixture, which was then mounted on a single tripod. Shutters were synchronized via I/O (miniDIN) ports. The single- or dual-camera system is then connected via USB to a small laptop computer running the camera-controlling software, MaxIm DL, from Diffraction Limited (supplied with Apogee systems). Raw images are acquired in FITS (Flexible Image Transport System) format [Pence *et al.*, 2010] for the purposes of this study and program, although MaxIm DL does offer the capability of acquiring other data formats. Plume imagery is obtained at a frequency of ~ 1 Hz, with interspersed clear sky and calibration images taken of quartz gas cells with known concentration path-length (units of ppm·m) of SO₂ for calibration of plume imagery. Plume images can then be converted from raw pixel brightness maps to concentration path-length maps via Beer’s Law:

$$A = -\log_{10} (I/I_0) \quad [1]$$

where A represents absorbance; I is equal to the light intensity, or raw pixel brightness value, after passing through SO₂; and I_0 is the unattenuated light intensity, taken to be the equivalent pixel brightness in the same location of the background image. The same equation is applied to calibration cell images, where known concentration path-lengths of SO₂ will have specific absorbances to construct a calibration curve that is then applied to maps of plume absorbance in order to convert them into SO₂ concentration path-length

images of the plume. Readers are referred to *Bluth et al.* [2007], *Dalton et al.* [2009], *Kantzas et al.* [2010], and *Kern et al.* [2010b] for more detailed descriptions and discussions on the use of UV cameras.

UVCamSO2 was developed using MATLAB R2008b and comprises seven main modules or subprograms, each of which addresses some aspect of UV camera image analysis and SO₂ emission rate extraction. The most basic of the modules are an image display program and a video creation tool. More advanced algorithms include programs to derive integrated column amounts (ICAs) of SO₂ and plume speeds from series of images. Other modules permit combination of ICA and plume speed files into emission rate time series, as well as display of previously processed data. A simplified schematic diagram of the program is shown in Figure 2.1.

2.3.1 Image and sequence viewing

Files used in this set of programs have a specific naming convention such that plume images have a single common prefix for all files, followed by sequential numbers (i.e., prefix_###.fits; file names are formatted as such during acquisition with MaxIm DL). In the case of two sets of images obtained with different bandpass filters, each filter requires its own filename prefix, with simultaneous images from different cameras sharing the same number (i.e., prefix307_###.fits and prefix326_###.fits). Clear sky (background sky) images and calibration cell images have the same prefix as the main sets of plume imagery, and share the sequential number of the plume image taken immediately before it, but also have suffixes of ‘_bg’ and ‘_cc’, respectively. This system of consistent prefixes and suffixes facilitates automation of the program such that the user is not forced to frequently browse for files during the processing.

Upon launching UVCamSO2.m, a graphical user interface (GUI) with a menu of options becomes available to the user (Figure 2.2). To simply view single images, the button ‘Display UV imagery’ is selected. Within this subroutine, the user is presented with the

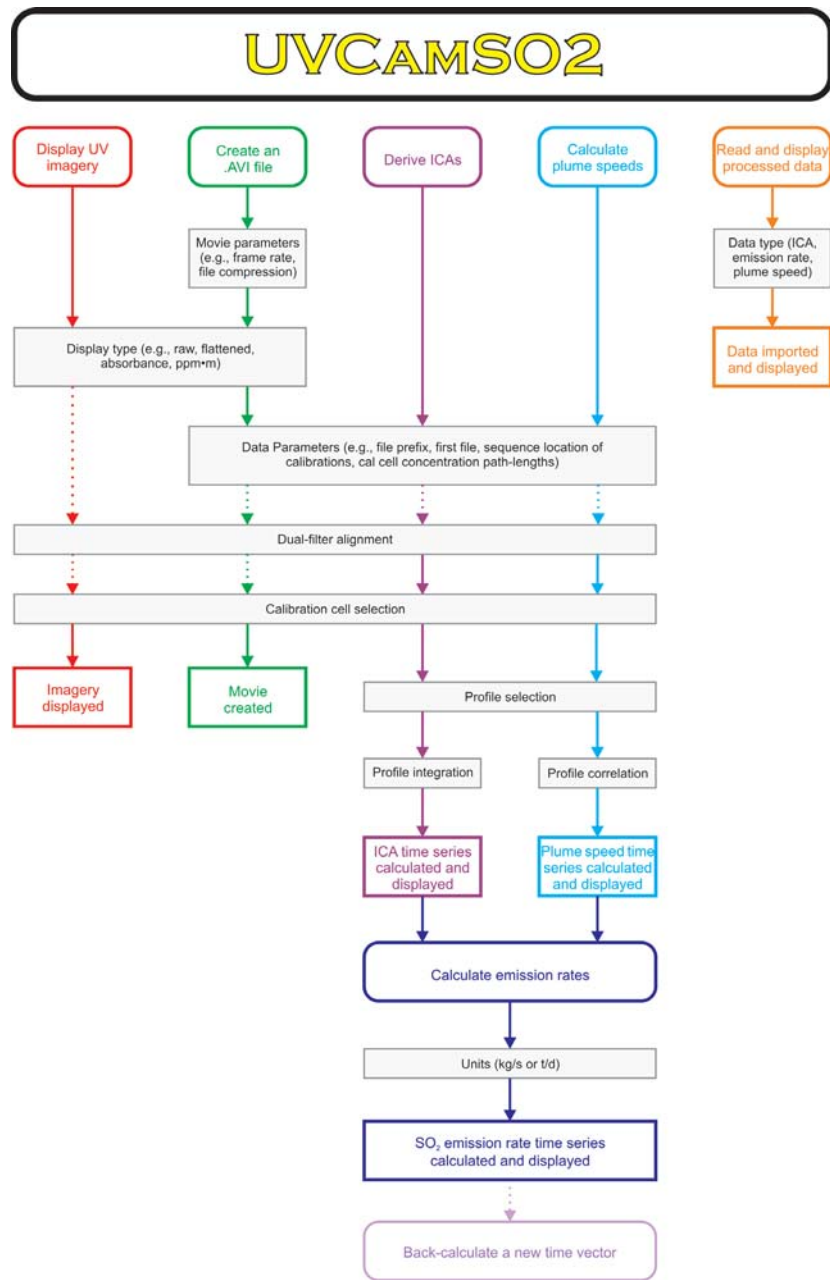


Figure 2.1: Schematic diagram of UVCamSO2 program and subroutines. Rounded boxes represent main modules and empty rectangles their associated outputs. Gray rectangles represent interactive user inputs and critical steps in the program. Many more intermediate steps exist, but are excluded from the diagram for clarity. Dotted arrows point to optional steps in the program flow. Note the absence of lateral steps on the diagram; processes follow directly from top to bottom in the image.

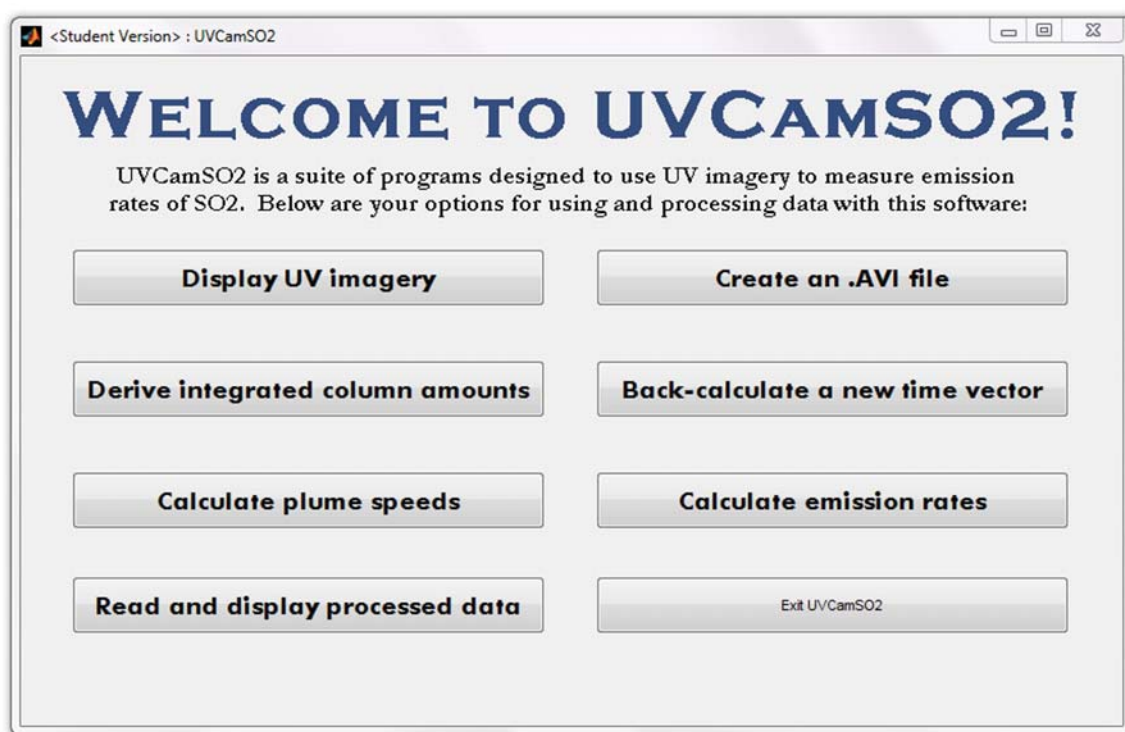


Figure 2.2: Main GUI window for UVCamSO2 program. All options may be run independently of each other, though emission rate calculations and data display require input of previously processed data files.

Chapter 2 – UVCamSO2 Program

option of displaying a raw image, a vignetting-corrected image (using a clear sky background image in addition to the plume image), an image converted to an absorbance map via Beer's Law (Equation 1), or an image converted to a map of concentration path-length of SO₂. Each of these options is available for a single-filter image or a dual-filter image pair. For each option, dialogue boxes prompt the user to select the plume image of interest, along with the appropriate background and calibration cell images, if necessary. Selecting the concentration path-length requires an extra step of identifying the calibration cells in the calibration cell image (Figure 2.3), and any dual-filter option requires an added step to register the slightly different fields of view of the two cameras. Registration is accomplished by prompting the user to register two sample images (one from each camera) manually or via cross-correlation. If the manual option is selected, the user identifies a stationary feature in one image and clicks it. The equivalent feature is then clicked in the second camera's image and the second image shifted relative to the first accordingly. The cross-correlation option removes potential user error by requiring the user to click on a feature in only the first camera's image. The image is subset to a 100×100 pixel area surrounding the click, and the same pixels are subset in the second camera's image as well. A Canny edge detection algorithm [Canny, 1986] is performed on each subset to delineate features. Two-dimensional cross-correlation of the edge maps provides the required image shift for alignment. To avoid erroneous correlations, the sample aligned image is displayed to the user prior to proceeding, such that the cross-correlation may be overridden with a manual alignment, if necessary.

A tool to convert sequences of images into AVI movie files is also available in the main code window, via the 'Create .AVI movie' button. The program prompts the user for the directory containing the imagery of interest, and requires user input such as file name prefix, number of images to include, image number at which to start the movie, and frame rate (Figure 2.4a). Options also include using background images to remove the vignetting effect in the movie's imagery as well as converting images into concentration path-length of SO₂ via the additional steps mentioned for individual image display. Images display

Chapter 2 – UVCamSO2 Program

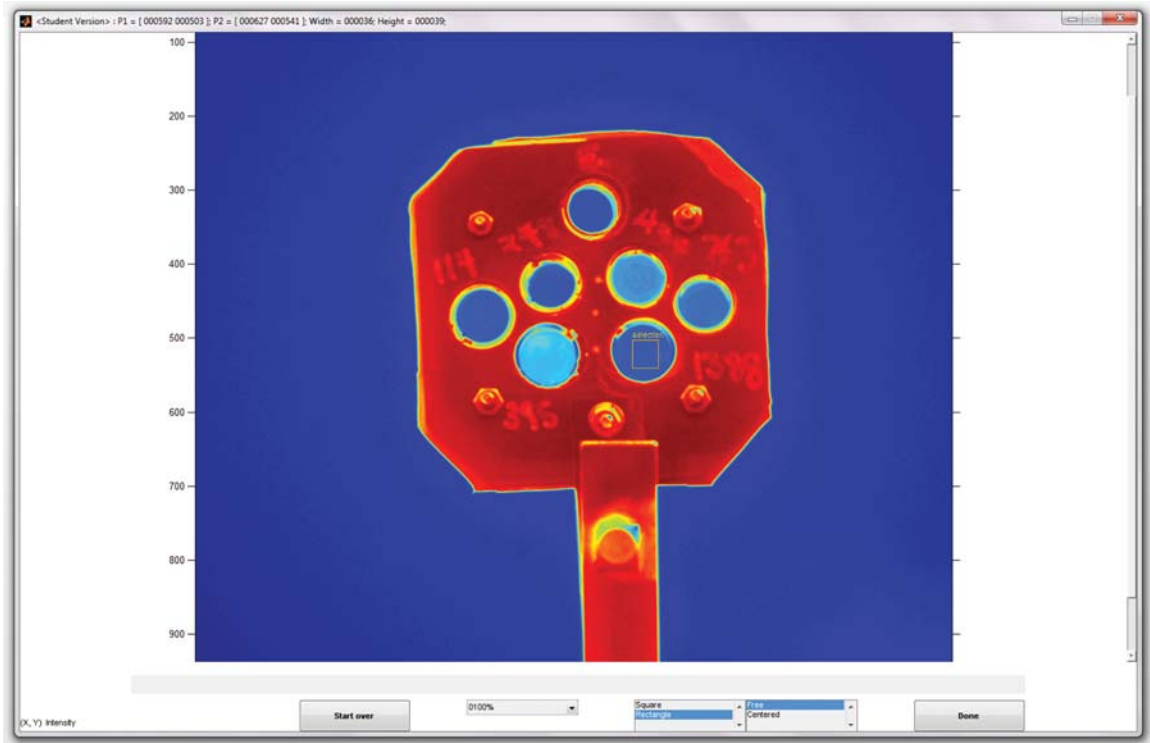


Figure 2.3: Calibration cell selection. The user dictates the dimensions of the rectangle selected, and may zoom in or re-do their selection as necessary using the buttons at the bottom of the image window.

sequentially on-screen as the code runs and each frame is stamped with the image number as well as time and date of image acquisition as recorded in the FITS file header. Final AVI files can be compressed, if desired, using the CinePak Pro (CVID) video codec.

2.3.2 SO₂ column amount extraction

Conversion of the raw imagery to column amounts of SO₂ is performed by the main processing routine, 'multi_image_processing_code.m'. Via user interaction, sequences of images and associated metadata are imported in to the program.

2.3.2.1 Initial input

The user is asked to select single- or dual-filter mode, following which, the code prompts the user for information regarding the files and initial data acquisition. These user-defined variables include the distance of the camera from the volcano's summit, points in the sequence at which calibrations were performed, and the concentration path-lengths of the calibration cells that were employed, of which there may be any number (Figure 2.4b). The program also includes an option of applying a distance, or 'air light,' correction [Bluth *et al.*, 2007] to account for scattering between the plume and the camera, which attenuates the absorption signal of SO₂. Next, if the dual-filter option is selected, the user must select the same feature on sample coincident plume images from each filter in order to co-register the imagery from each camera.

2.3.2.2 Profile selection

Once the images are properly aligned, the user then selects profile lines (ideally) perpendicular to the direction of plume propagation and as close as possible to the degassing vent while still covering the full width of the plume. These profiles are sampling lines for the plume in each image; the SO₂ column amounts will be integrated over the length of the profile line and later converted to the emission rate of SO₂. The images for which the

Chapter 2 – UVCamSO2 Program

a)

<Student Version> : Input specs

What is the prefix on your 307 file names?

What is the prefix on your 326 file names?

How many files are going to be processed?

What is the sequence number of the first file?

Do you want to examine all images? Every 2nd one? Every 6th one? Enter the corresponding integer (e.g., 1,2,6, etc.)

What frame rate do you want your movie to have, in frames per second?

At which numbers in the sequence did the field of view of the cameras change (including the first image)? Enter as a vector (i.e., [...300 600...]).

OK Cancel

b)

<Student Version> : Initial input for UV camera data processing:

What is the prefix on your 307 file names?

What is the prefix on your 326 file names?

How many files (for each filter) are going to be processed?

What is the number at the end of the first file? (if includes zeros, as will 006 or 035, DO NOT include the zeros)

Do you want to examine all images? Every 2nd one? Every 6th one? Enter the corresponding integer (e.g., 1,2,6, etc.)

How far was the camera from the plume in meters?

Please enter, as a vector, the locations in the sequence of your background images (i.e., if you took background images after images 300, 600, and 900, enter [300 600 900]). For pre-sequence background, use a zero. If there were 2 background images at the same spot in the sequence, add a "2" to the second one (i.e., [... 600 600 2 ...]).

Please enter, as a vector, the locations in the sequence of your cal cell images (i.e., if you took cal cell images after images 300, 600, and 900, enter [300 600 900]). For pre-sequence (assuming your sequence starts at 1) cal cells, use a zero. If there were 2 cal cell images at the same spot in the sequence, add a "2" to the second one (i.e., [... 600 600 2 ...]).

Now enter, as a vector, the image numbers that you want to use for clicking profile endpoints. These should essentially be the first image you took after having moved the camera, whether there is a usable background or cal cell image there or not. So for this vector, you do not need to deal with the .2 stuff from the other vectors.

Enter, as a vector and in increasing order, the concentration pathlengths of your calibration cells in ppm.

OK Cancel

Figure 2.4: Sample input windows for subroutines of UVCamSO2. (a) Movie making input window. (b) Main ICA derivation input window. Other subroutines utilize similar input windows.

profiles are selected are determined by user input from the initiation of the code. At least one profile is necessary, but further profiles may be required to account for changing plume geometry or camera movement. Each profile selected is maintained until either the end of the sequence or until the next image with a profile selected is reached.

2.3.2.3 Calibration

Once all profiles are chosen, images must be calibrated in units of concentration path-length. First, each calibration image is converted into a map of absorbance via Beer's Law (Equation 1). The user is then prompted, for each calibration image (and for each filter, if dual-filter processing was selected), to select a small rectangular area within each calibration cell. The image window has zoom capabilities for enhanced precision in selection (Figure 2.3). Once boxes have been selected for each cell, mean absorbance values from the user-selected areas in each cell in the calibration images are used with the known concentration path-length values of the cells to derive a linear calibration curve relating absorbance to concentration path-length (Figure 2.5). The calibration curves determined for each calibration image are then applied to plume absorbance values to convert each plume image in the sequence into a map of concentration path-length of SO₂. At this point in the processing, pre-processing user input is complete and the code runs independently until post-processing.

2.3.2.4 Integrated column amount (ICA) derivation

Each converted map of plume concentration path-length is sampled along the previously selected input profile lines, yielding a profile of SO₂ concentration path-length. Upon completion of the processing for all images, the series of profiles is plotted in an image as a stack (Figure 2.6). At this stage, background drift (a result of variations in sun illumination) and non-zero backgrounds may be corrected for via user designation of SO₂-free areas of the profile stack. A single-sided option, for a grounded plume or one of

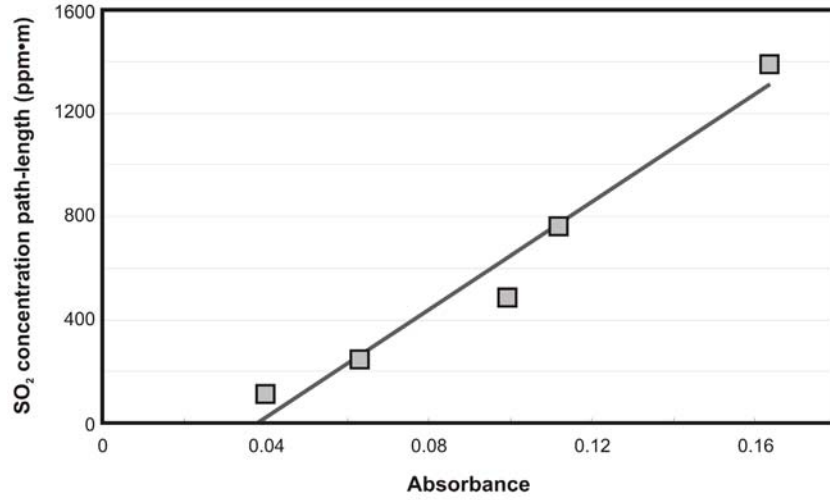


Figure 2.5: A sample calibration curve derived from calibration cell selection. Linear curves are fit to the absorbance data, having been shown to be valid for concentration path-lengths of up to ~1500 ppm·m [Dalton *et al.*, 2009].

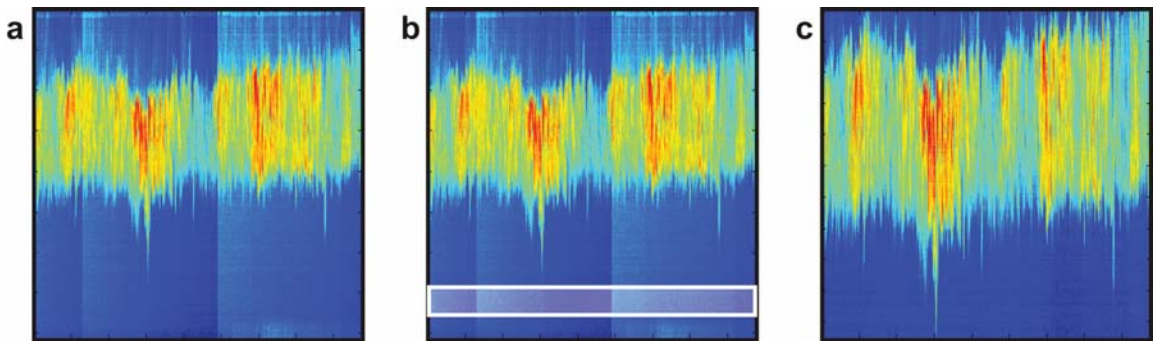


Figure 2.6: Stack of profiles from successive images for background drift correction. a) Profiles from successive images are stacked; time increases to the right. Note variable brightness of background sky pixels on either side of plume trace including gradual drift as a result of brightening sky and sharp transitions reflecting exposure time changes. b) Representative ranges of background pixels are designated by the user. Average values for background pixels for each individual profile are calculated and subtracted from each pixel in the profile. c) Background drift has been mostly eliminated and background sky values have been set to zero.

Chapter 2 – UVCamSO2 Program

uniform background illumination, involves selecting range of pixels in each stack to be designated as SO₂-free. The mean of these background values for each profile is subtracted from all values in the profile. The background pixels are therefore set to zero, with the same offset applied to all pixels, including those containing SO₂. In the case of a lofting plume with different degrees of background sky brightness on either side (as can be the case early or late in the day), a small range of pixels may be selected on each side of the plume. The mean of each range is then calculated, and a linear trend between them determined. The code then uses the calculated trend to determine the associated offset for each pixel in the profile and then corrects accordingly for each individual profile in the stack. The user may also subset the stack of profiles to eliminate any erroneous features that were sampled by the profile, such as the volcano edifice, meteorological clouds, people, or wind-blown debris. At this stage an option exists for delineating multiple gas sources in the profile stack, as it is sometimes possible to distinguish more than one plume or vent within UV imagery [Nadeau *et al.*, 2011; Tamburello *et al.*, 2011]. Divisions between any number of plumes are drawn interactively by the user so that each plume is later integrated separately. Next, each corrected (and subset, if necessary) profile is integrated using a cumulative trapezoidal approximation to yield an ICA of SO₂ (units of ppm·m²) for each image in the sequence. If multiple plumes were delineated, they are integrated both individually and as a single bulk plume. Final ICA results are written to a text file for future use in the same directory as the image files using the time that the file is written as a unique file identifier. A full matrix of line profile stacks is also saved. Segments with multiple plumes are saved with a similar format, including the identifier ‘multiICA’. Finally, a metadata file including a record of input and other information, such as profile line and calibration cell coordinates, is written. Examples of these ICA data and metadata files, as well as other types of data files mentioned below, are given in the appendix, including column headings.

2.3.3 Plume speed determination

To calculate an emission rate of SO₂ from ICAs of SO₂, the following equation is necessary:

$$\text{Emission Rate of SO}_2 = [\text{SO}_2]_{\text{pl}} * \cos \theta * d_{\text{seg}} * v_{\text{pl}} * C_F \quad [2]$$

where $[\text{SO}_2]_{\text{pl}}$ is the average concentration path-length of SO₂ (ppm·m) in a given profile through the plume, θ (°) is the deviation from perpendicularity of the slice of plume with respect to the gas plume's direction of propagation and d_{seg} is the width (m) of the plume over that profile. The term v_{pl} is the plume speed (m/s) and C_F is a factor to convert ppm·m³/s into metric tonnes per day (t/d) or kilograms per second (kg/s). $[\text{SO}_2]_{\text{pl}}$ and d_{seg} have already been combined into ICA via the integration of full profiles in the previous section of code, thus requiring only plume speed and a cosine correction factor to arrive at an emission rate. Given that profiles should be drawn perpendicular to the plume during profile selection, $\cos \theta$ should be equivalent to 1.

To derive plume speed, another subroutine uses nearly identical initial input as the main processing code (e.g., Figure 2.4b). Initial input is entered by the user and, in place of profiles perpendicular to the plume, longitudinal profiles of the plume are selected and applied to the maps of SO₂ concentration path-length. In cases of complicated plume geometry within the image such that the initial ICA profile cannot be drawn at 90° to the direction of plume propagation, the plume speed profile should be selected perpendicular to the ICA profile rather than the exact vector of the plume's propagation such that cosine correction factors for both would be equivalent and cancel. Sampled concentration path-length profiles are smoothed using a window size set by the user, after which, in a modification of the method of plume speed derivation of *Williams-Jones et al.* [2006], profiles from successive images are iteratively fit to maximize the coefficient of determination (r^2). The spatial lag at which this maximum occurs is combined with the temporal resolution of the imagery to derive a plume speed for each pair of images. Because of potential fitting problems with ambiguous signals, such as sinusoidal profiles or other repetitive signals, a

Chapter 2 – UVCamSO2 Program

maximum reasonable lag is set in the code. In the case of large gaps in time between successive profiles, the subsequent plume speed is substituted for the image following the time gap. The same substitution is made for pairs of profiles that yield a poor fit. Finally, the plume speed time-series is smoothed using a Hanning window of user-defined length in order to reduce noise within the dataset. Results are written to a text file in the same directory in which the images are stored. In the case of multiple plumes in single images, the plume speed code may also be run multiple times, treating each plume separately.

Time stamps associated with the SO₂ ICAs are initially the time of the image acquisition, but the measured SO₂ has already traveled a distance from the vent to the profile. Derived plume speeds, in combination with the known location of the gas source and the original ICA profile line, can then be used in order to back-calculate the time series to the source by determining the amount of time a measured parcel of SO₂ took to reach the measurement profile. Times are adjusted to yield a vector of estimated times of SO₂ emission from the vent; the plume speed derived from a pair of images is used to determine where the parcel of plume on the profile line in the second image would have been in the first image of the pair. This process repeats iteratively using plume speeds from previous images until a time has been determined for when the parcel of plume that was originally on the profile measurement line would theoretically have been emitted at the volcanic vent. Early in a time series or following long gaps in the image acquisition, when there is not sufficient information to determine earlier plume speeds for a given plume parcel, the plume speed obtained following the data gap is extended to apply to those images as well.

2.3.4 SO₂ emission rate calculations

The smoothed time-series of back-calculated plume speeds is then multiplied by the time-series of ICAs and a conversion factor to yield a time-series of SO₂ emission rates via equation 2. The program allows for the selection of previously processed plume speed and SO₂ ICA files and subsequently converts them into SO₂ emission rates in units of either kg/s

or t/d, based on the user's selection. The same images must comprise the data in each of the files, with the vectors in the files being the same length, so that the ICA and plume speed information for each image are correctly paired with each other. Emission rates are plotted and also written to new text files, following a similar naming convention as other types of files.

2.3.5 Other programs

Also included in the package of codes is a program via which the user may select a previously processed file, either ICA, plume speed, or emission rate, and with or without back-calculated times. The program imports the pre-processed data for further analysis, if desired, in addition to plotting the data on a graph.

2.4 Validation

2.4.1 SO₂ emission rates

As the UV camera is a relatively new technology in the field of volcanology, validation of the instrument and data processing algorithms is necessary. In March of 2008, a multi-instrument field campaign was carried out at Masaya volcano, Nicaragua. Masaya is frequently the subject of volcanic gas studies, as it has been continuously degassing with a robust, ash-free plume for years and is highly accessible [Burton *et al.*, 2000; Martin *et al.*, 2010; Nadeau and Williams-Jones, 2009]. On the March 19, 2008, 11 FLYSPEC measurements were made simultaneously with UV camera data acquisition as a means to validate the UV camera and this processing algorithm. The FLYSPEC was mounted on a car and driven beneath the plume on a road approximately 5 km downwind (west) of the active vent. UV camera images were acquired using a 307 nm filter from a location on the north rim of Masaya Caldera, approximately 4.5 km from the vent, at a rate of ~ 0.25 Hz. Single-filter imagery would not normally be ideal for comparison to the data from an instrument with wide spectral range, as with FLYSPEC, but periodic images acquired with a 326 nm filter indicate little to no

absorption by the plume in that wavelength interval; we therefore assume little interference from gas or aerosol species other than SO₂, making single-filter imagery an accurate representation of SO₂ emission rates.

Imagery was processed using the codes described above with a profile location chosen at the edge of the volcanic cone complex containing the degassing crater. The discrepancy between camera and FLYSPEC measurement sites is a possible cause of erroneous or mismatched values for emission rates; simultaneous measurements from each of the two instruments also do not measure the same portions of the plume. A puff would have been measured by the UV camera earlier, prior to traveling downwind 5 km to the FLYSPEC traverse route. To compensate for the timing offset, we used the plume speed derived from UV camera imagery to back-calculate FLYSPEC times, similar to the camera data back-calculation previously described. Examination of the plot reveals that most of the FLYSPEC ICAs fall within the range of the varying camera-derived ICAs around the same time (Figure 2.7). Mixing and advection within the plume, as well as different plume speeds at the different measurement sites [e.g., *Nadeau and Williams-Jones*, 2009], could account for discrepancies, and we find the comparable results encouraging.

2.4.2 Plume speed

For validation of the plume speed program, we processed 12 days (May 5, 6, 11, 12, 13, 14, 20, 21, 22, 24, 25, and 26, 2010) of UV camera data from the summit vent of Kilauea Volcano, Hawaii, for which we had simultaneous 10-minute averages of wind speed from a permanent anemometer (~3 m above ground surface) stationed at the Hawaiian Volcano Observatory, located near the volcano's summit. Sample data are shown in Figure 2.8. Data on most dates coincide well, though there are instances of both over- and under-estimation of anemometer wind speeds by the plume speed algorithm. Such discrepancies are likely due to the fact that the anemometer measures near-ground level wind speeds, whereas the plume speed code is actually measuring the (apparent) velocity vector of the plume that lies in the

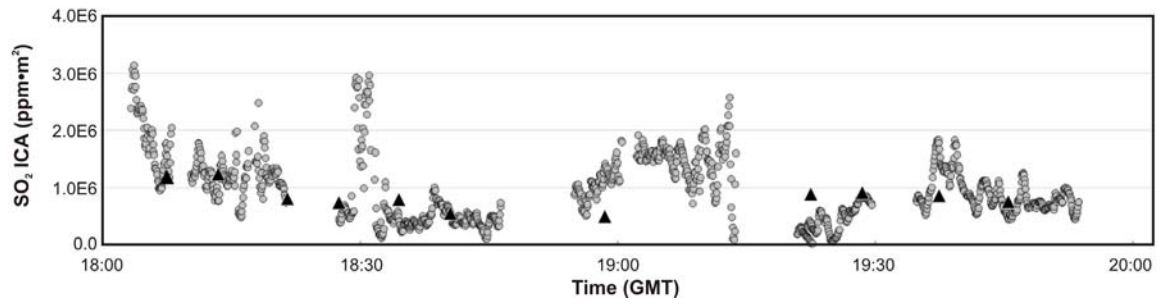


Figure 2.7: ICA data from UV camera and FLYSPEC at Masaya Volcano, Nicaragua on March 18, 2008. Camera data are represented by gray circles; FLYSPEC data points (back-calculated to the approximate time of emission at the volcanic vent) are shown as black triangles

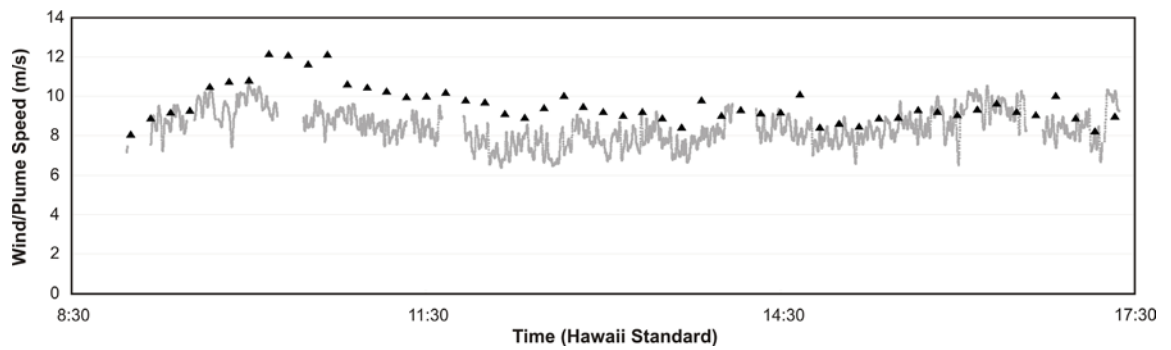


Figure 2.8: Coincident UV camera-derived plume speeds (gray dots) and 10-minute average anemometer wind speeds (black triangles) from weather station located ~2 km from the plume at the Hawaiian Volcano Observatory. Data are from May 22, 2010.

plane of the image and is also generally well above ground level, which therefore may have a different magnitude and direction from that of the ground-based wind speed. Excluding three days on which calculated plume speeds were more akin to rise rates than representative of plume speed, the mean percent difference between 10-minute anemometer averages and coincident 10-minute UV camera averages on any given day ranged from only 5 to 15%.

2.4.3 Associated errors

Sources of error in UV camera measurements have been identified by *Dalton et al.* [2009] and *Kern et al.* [2010b]. Further, we note that inaccuracy of the calibration cell concentration path-length and uncertainty in the distance from the camera to the plume may also induce errors into the UV camera method. Though such errors may cause derived emission rates to suffer with respect to accuracy, error sources are not likely to vary on time scales on the order of image acquisition frequency. Accordingly, precision is not affected; relative changes are well preserved within the data. While accurate representations of SO₂ emission rate are the ultimate goal of UV camera measurements and this data processing algorithm, relative variations in emission rate are still valuable when comparing emission rate time-series with geophysical data [*Nadeau et al.*, 2011].

In general, it is important to note that some of these errors are difficult to quantify or even avoid, and the UV camera method is still under development and the subject of current research. The code will be adapted in the future as these problems are better understood and it is clearer how to circumvent them.

2.5 Conclusions

The lack of high temporal resolution volcanic gas data has previously hampered attempts to link various geophysical and volcanic phenomena to a gas-phase source, limiting such studies to long term comparisons [*Fischer et al.*, 1994; *Palma et al.*, 2008; *Williams-Jones et al.*, 2001]. The advent of UV cameras has significantly improved both the spatial and

Chapter 2 – UVCamSO2 Program

temporal resolution of volcanic SO₂ emission rate measurements and via the program package we describe in this paper, UV camera data processing is manageable and can be performed at a reasonable rate. The program can handle upwards of 10,000 images or pairs of images (~1 day of data) at a time and requires minimal user interaction following the initial phase of user input. Output is written to small text files and includes metadata if later replication of the processing is desired. Use of this UV camera and processing program has already made it possible to identify correlations between SO₂ degassing patterns, low-frequency seismicity, and ash-rich explosions at Fuego volcano, Guatemala [Nadeau *et al.*, 2011]. UV camera systems have led to exciting results at other volcanoes [Dalton *et al.*, 2010; Holland *et al.*, 2011; Kazahaya *et al.*, 2011; Tamburello *et al.*, 2011], and this program has already been employed at least in part by two such studies [Dalton *et al.*, 2010; Nadeau *et al.*, 2011]. We expect that this program will facilitate further use of UV cameras at volcanoes worldwide.

Future developments of this program include the addition of an optical flow algorithm to better constrain plume speed and the spatial variability of plume speed. While the temporal resolution of UV imagery is generally on the order of 0.25 – 1 Hz, derived emission rate measurements of higher resolution are also possible. Current codes evaluate parcels of plume along a single chosen profile to yield an emission rate at the moment of image capture. Inter-image emission rate information is preserved in successive images such that modifications could be made to evaluate additional profiles on a single image to achieve the higher temporal resolution. Other additions may include an option for calibration or correction via the incorporation of spectral data from a DOAS-based instrument collocated with the UV camera system [Kern *et al.*, 2010b]. Adaptations for other image formats are also possible, if necessary.

UVCamSO2 is open-source and available from the authors. It is also available for registered users at Vhub.org (<http://vhub.org/resources/1069>). Because the UV camera is a new technique in the field of volcanology, the data processing code will undergo continued development as new datasets are acquired; updated versions will be available in the ‘Offline

Tools' section of the VHub.org database, where the authors can also receive reviews, suggestions for improvement, and notification of any modifications or other applications by users.

2.6 Acknowledgements

Work on this project was supported by NSF PIRE 0530109. Supplemental funding for PAN included a Grant-In-Aid of Research from Sigma Xi, The Scientific Research Society; a Geological Society of America Graduate Student Research Grant; and a grant from the Michigan Space Grant Consortium. JLP has also been supported during the preparation of this paper by NSF CDI 0940831. We would like to thank M. Dalton, A. Graettinger, and L. Porritt for assistance with field work and data collection; G. Williams-Jones for FLYSPEC use; INGUAT, INSIVUMEH, Hawaii Volcanoes National Park, and the Hawaiian Volcano Observatory for logistical support; M. Dalton, I.M. Watson, J. Shannon, H. Thomas, M. Patrick, C. Kern, C. Werner, I. Brewer, K. Hicks, and P. Holland for useful discussions and program testing; G. Waite and S. Carn for advice; and the National Park Service for sharing wind speed data.

2.7 References

- Bluth, G. J. S., J. M. Shannon, I. M. Watson, A. J. Prata, and V. J. Realmuto (2007), Development of an ultra-violet digital camera for volcanic SO₂ imaging, *Journal of Volcanology and Geothermal Research*, 161(1-2), 47-56.
- Burton, M. R., C. Oppenheimer, L. A. Horrocks, and P. W. Francis (2000), Remote sensing of CO₂ and H₂O emission rates from Masaya volcano, Nicaragua, *Geology*, 28(10), 915-918.
- Canny, J. (1986), A Computational Approach to Edge Detection, *Pattern Analysis and Machine Intelligence, IEEE Transactions on*, PAMI-8(6), 679-698.
- Dalton, M. P., I. M. Watson, P. A. Nadeau, C. Werner, W. Morrow, and J. M. Shannon (2009), Assessment of the UV camera sulfur dioxide retrieval for point source plumes, *Journal of Volcanology and Geothermal Research*, 188(4), 358-366.

Chapter 2 – UVCamSO₂ Program

- Dalton, M. P., G. P. Waite, I. M. Watson, and P. A. Nadeau (2010), Multiparameter quantification of gas release during weak Strombolian eruptions at Pacaya Volcano, Guatemala, *Geophysical Research Letters*, 37(9), L09303.
- Elias, T., A. J. Sutton, C. Oppenheimer, K. A. Horton, H. Garbeil, V. Tsanev, A. J. S. McGonigle, and G. Williams-Jones (2006), Comparison of COSPEC and two miniature ultraviolet spectrometer systems for SO₂ measurements using scattered sunlight, *Bulletin of Volcanology*, 68(4), 313-322.
- Fischer, T. P., M. M. Morrissey, M. L. Calvache, D. Gomez, R. Torres, J. Stix, and S. N. Williams (1994), Correlations between SO₂ flux and long-period seismicity at Galeras Volcano, *Nature*, 368(6467), 135-137.
- Galle, B., C. Oppenheimer, A. Geyer, A. J. S. McGonigle, M. Edmonds, and L. Horrocks (2003), A miniaturised ultraviolet spectrometer for remote sensing of SO₂ fluxes: a new tool for volcano surveillance, *Journal of Volcanology and Geothermal Research*, 119(1-4), 241-254.
- Holland, A. S. P., I. M. Watson, J. C. Phillips, L. Caricchi, and M. P. Dalton (2011), Degassing processes during lava dome growth: Insights from Santiaguito lava dome, Guatemala, *Journal of Volcanology and Geothermal Research*, 202(1-2), 153-166.
- Horton, K. A., G. Williams-Jones, H. Garbeil, T. Elias, A. J. Sutton, P. Mouginiis-Mark, J. N. Porter, and S. Clegg (2006), Real-time measurement of volcanic SO₂ emissions: validation of a new UV correlation spectrometer (FLYSPEC), *Bulletin of Volcanology*, 68(4), 323-327.
- Jaupart, C., and S. Vergnolle (1988), Laboratory models of Hawaiian and Strombolian eruptions, *Nature*, 331(6151), 58-60.
- Kantzas, E. P., A. J. S. McGonigle, G. Tamburello, A. Aiuppa, and R. G. Bryant (2010), Protocols for UV camera volcanic SO₂ measurements, *Journal of Volcanology and Geothermal Research*, 194(1-3), 55-60.
- Kazahaya, R., T. Mori, M. Takeo, T. Ohminato, T. Urabe, and Y. Maeda (2011), Relation between single very-long-period pulses and volcanic gas emissions at Mt. Asama, Japan, *Geophysical Research Letters*, 38(11), L11307.
- Kern, C., F. Kick, P. Lübcke, L. Vogel, M. Wöhrbach, and U. Platt (2010b), Theoretical description of functionality, applications, and limitations of SO₂ cameras for the remote sensing of volcanic plumes, *Atmospheric Measurement Techniques*, 3(3), 733-749.

Chapter 2 – UVCamSO₂ Program

- Martin, R. S., G. M. Sawyer, L. Spampinato, G. G. Salerno, C. Ramirez, E. Ilyinskaya, M. L. I. Witt, T. A. Mather, I. M. Watson, J. C. Phillips, and C. Oppenheimer (2010), A total volatile inventory for Masaya Volcano, Nicaragua, *Journal of Geophysical Research*, 115(B9), B09215.
- Mori, T., and M. Burton (2006), The SO₂ camera: A simple, fast and cheap method for ground-based imaging of SO₂ in volcanic plumes, *Geophysical Research Letters*, 33(24), L24804.
- Nadeau, P. A., and G. Williams-Jones (2009), Apparent downwind depletion of volcanic SO₂ flux-lessons from Masaya Volcano, Nicaragua, *Bulletin of Volcanology*, 71(4), 389-400.
- Nadeau, P. A., J. L. Palma, and G. P. Waite (2011), Linking volcanic tremor, degassing, and eruption dynamics via SO₂ imaging, *Geophysical Research Letters*, 38(1), L01304.
- Palma, J. L., E. S. Calder, D. Basualto, S. Blake, and D. A. Rothery (2008), Correlations between SO₂ flux, seismicity, and outgassing activity at the open vent of Villarrica volcano, Chile, *Journal of Geophysical Research-Solid Earth*, 113(B10), B10201.
- Palma, J. L., S. Blake, and E. S. Calder (2011), Constraints on the rates of degassing and convection in basaltic open-vent volcanoes, *Geochemistry Geophysics Geosystems*, 12(11), Q11006.
- Parfitt, E. A., and L. Wilson (1995), Explosive volcanic eruptions-IX. The transition between Hawaiian-style lava fountaining and Strombolian explosive activity, *Geophysical Journal International*, 121(1), 226-232.
- Pence, W. D., L. Chiappetti, C. G. Page, R. A. Shaw, and E. Stobie (2010), Definition of the Flexible Image Transport System (FITS), version 3.0, *Astronomy & Astrophysics*, 524, A42.
- Stoiber, R. E., and A. Jepsen (1973), Sulfur dioxide contributions to the atmosphere by volcanoes, *Science*, 182(4112), 577-578.
- Stoiber, R. E., L. L. Malinconico, and S. N. Williams (1983), Use of the correlation spectrometer at volcanoes, in *Forecasting volcanic events*, edited by H. Tazieff and J. C. Sabroux, pp. 424-444, Elsevier, New York.
- Tamburello, G., E. P. Kantzas, A. J. S. McGonigle, A. Aiuppa, and G. Giudice (2011), UV camera measurements of fumarole field degassing (La Fossa crater, Vulcano Island), *Journal of Volcanology and Geothermal Research*, 199(1-2), 47-52.

Chapter 2 – UVCamSO2 Program

- Watson, I. M., C. Oppenheimer, B. Voight, P. W. Francis, A. Clarke, J. Stix, A. Miller, D. M. Pyle, M. R. Burton, S. R. Young, G. Norton, S. Loughlin, and B. Darroux (2000), The relationship between degassing and ground deformation at Soufriere Hills Volcano, Montserrat, *Journal of Volcanology and Geothermal Research*, 98(1-4), 117-126.
- Williams-Jones, G., J. Stix, M. Heiligmann, J. Barquero, E. Fernandez, and E. D. Gonzalez (2001), A model of degassing and seismicity at Arenal Volcano, Costa Rica, *Journal of Volcanology and Geothermal Research*, 108(1-4), 121-139.
- Williams-Jones, G., K. A. Horton, T. Elias, H. Garbeil, P. J. Mougini-Mark, A. J. Sutton, and A. J. L. Harris (2006), Accurately measuring volcanic plume velocity with multiple UV spectrometers, *Bulletin of Volcanology*, 68(4), 328-332.

Chapter 3: LINKING VOLCANIC TREMOR, DEGASSING, AND ERUPTION DYNAMICS VIA SO₂ IMAGING*

3.1 Abstract

Recently developed UV cameras offer improvement in remote sensing of volcanic SO₂, with temporal resolutions of ~1 Hz and synoptic plume views. Integrated UV camera and seismic measurements recorded in January 2009 at Fuego volcano, Guatemala, provide new insight into the system's shallow conduit processes. High temporal resolution SO₂ data reveal patterns of SO₂ emission rate relative to explosions and seismic tremor that indicate tremor and degassing share a common source process. Progressive decreases in emission rate appear to represent inhibition of gas loss from magma as a result of rheological stiffening in the upper conduit. Measurements of emission rate from two closely-spaced vents, made possible by the high spatial resolution of the camera (1024 × 1024 pixels), help constrain this model. This inter-disciplinary approach illuminates eruptive processes at Fuego and holds promise for gaining similar understanding at other volcanic systems.

3.2 Introduction

Volatiles play a crucial role in volcanism; their segregation from melts is fundamental in determining subsurface and eruptive processes. Bubbles affect generation of low-frequency seismicity and seismic tremor is typically attributed to interaction of multiphase magmatic or hydrothermal fluids and conduit walls [Chouet, 1996; Ripepe and Gordeev, 1999], and eruptive style varies depending on gas-melt dynamics [Jaupart and Vergnolle, 1988; Parfitt

* This chapter, along with Appendix E, was previously published as:

Nadeau, P. A., J. L. Palma, and G. P. Waite (2011), Linking volcanic tremor, degassing, and eruption dynamics via SO₂ imaging, *Geophysical Research Letters*, 38(1), L01304.

Copyright 2011 by the American Geophysical Union. See Appendix F for a copy of the copyright transfer agreement.

and Wilson, 1995]. Though many models of volcanic phenomena depend on gas behavior, volcanic gas release has historically been difficult to quantify. Ground-based measurements of SO₂ emission rate made by ultraviolet (UV) spectrometers have been common since the 1970s, but generally lack temporal resolution sufficient for evaluation alongside continuous geophysical data. Previous studies have linked seismicity with SO₂ emission rates [Fischer *et al.*, 1994; Palma *et al.*, 2008; Williams-Jones *et al.*, 2001], but over time-scales of months to years and based on sporadic SO₂ measurements. Integrated studies have thus been limited to interpretation of long-term degassing trends [Palma *et al.*, 2008; Williams-Jones *et al.*, 2001].

With images collected nearly every second, UV cameras [Bluth *et al.*, 2007; Dalton *et al.*, 2009; Mori and Burton, 2006] facilitate studies of volcanic degassing on unparalleled timescales. Accordingly, high-resolution SO₂ emission rate time-series can be used to corroborate models of tremor generation or eruption dynamics involving gas. In addition, two-dimensional images provide spatial context to observe variations within plumes and to identify multiple vents with distinct behaviors. As volatile segregation provides the driving force for volcanic eruptions, knowledge of how gas escape relates to other geophysical phenomena is essential for a comprehensive understanding of volcanic behavior.

Here we show that enhanced resolutions of UV camera data, both temporal and spatial, allow SO₂ data to be jointly interpreted with seismic and visual video records to give unprecedented insight into degassing and eruption dynamics. We present results from a January 2009 field campaign using seismometers, visual observations, and a UV camera to study Fuego volcano's activity and relationships between degassing and seismic tremor. Fuego is a basaltic-andesite stratovolcano (~3800 m a.s.l.) in central Guatemala. Historical volcanism ranges from basaltic subplinian eruptions, most recently in 1974 [Rose *et al.*, 1978; Rose *et al.*, 2008], to persistent lower-level activity, the current phase of which began in 1999 and involves periodic lava flows, passive degassing, and explosions [Lyons *et al.*, 2010].

3.3 Methods

We collected digital UV images from ~ 1 km north of, and ~ 200 m below, the summit using an Apogee Alta U6 camera outfitted with a CoastalOpt 105 mm UV lens and an Andover Optics bandpass filter centered at 307 nm. Our field methodology followed *Bluth et al.* [2007] and recommendations by *Dalton et al.* [2009] for ideal exposure times and calibrations and resulted in ~ 0.5 Hz image data (dictated by ambient light and computer speed) with ~ 0.25 m pixels. We discarded images with ash present in the plume (Figure 3.1) or clouds in front of the edifice. To retrieve SO_2 emission rates from series of images, we used 5 calibration cells to convert raw images to SO_2 concentration path-length. Integrated profiles of the plume were multiplied by internally derived plume speeds following *Bluth et al.* [2007]. Plume speeds were also used to back-calculate emission rates from profile location to the vent. For a more detailed explanation of UV image processing, see auxiliary material.

We installed broadband seismometers on Fuego’s flanks, with the closest station ~ 700 m from the summit vent. We restricted our analysis to a band-limited (1–5 Hz) 10 second average seismic amplitude (RSAM) [*Endo and Murray*, 1991] time-series from the closest station (a 30 second Gralp CMG-40T with a Reftek 130 digitizer) to highlight variation on the order of minutes and to bracket the dominant tremor frequencies.

3.4 Results

Continuous but varying passive gas emissions were interrupted roughly twice per hour by ash-rich explosions (Figure 3.1, Figure 3.2a, b, Figure E.2). Owing to poor weather (e.g., high winds, clouds), UV image acquisition was restricted to 12, 14, and 21 January 2009, with 169, 3447, and 5277 images in 0.25, ~ 8 , and ~ 8.5 hours, respectively. Measured SO_2 emission rates range from 0.0014 kg/s to 6.5 kg/s with daily means of 0.86, 1.5, and 0.59 kg/s and an overall mean of 0.94 kg/s (81 t/d), comparable to 1.9 kg/s (160 t/d) and 3.9 kg/s (340 t/d) reported for Fuego in previous years [*Andres et al.*, 1993; *Rodriguez et al.*, 2004]. While explosive SO_2 emissions cannot be quantified due to ash interference, many



Figure 3.1: Examples of activity at Fuego volcano, Guatemala. (a) Ultraviolet (UV) camera imagery of variable gas emissions from two vents prior to an explosion. Times are GMT on 21 January 2009; UV image width is ~ 260 m and view is to the south. (b) Example of an ash-rich explosion plume (~ 450 m in height above summit). Explosions were variable in size; column heights reached a maximum of ~ 500 m above the summit. Explosion onsets ranged from emergence of a single pulse of ash from the summit area driven solely by buoyancy to momentum-driven jets with sustained pulsing for up to ~ 2 minutes.

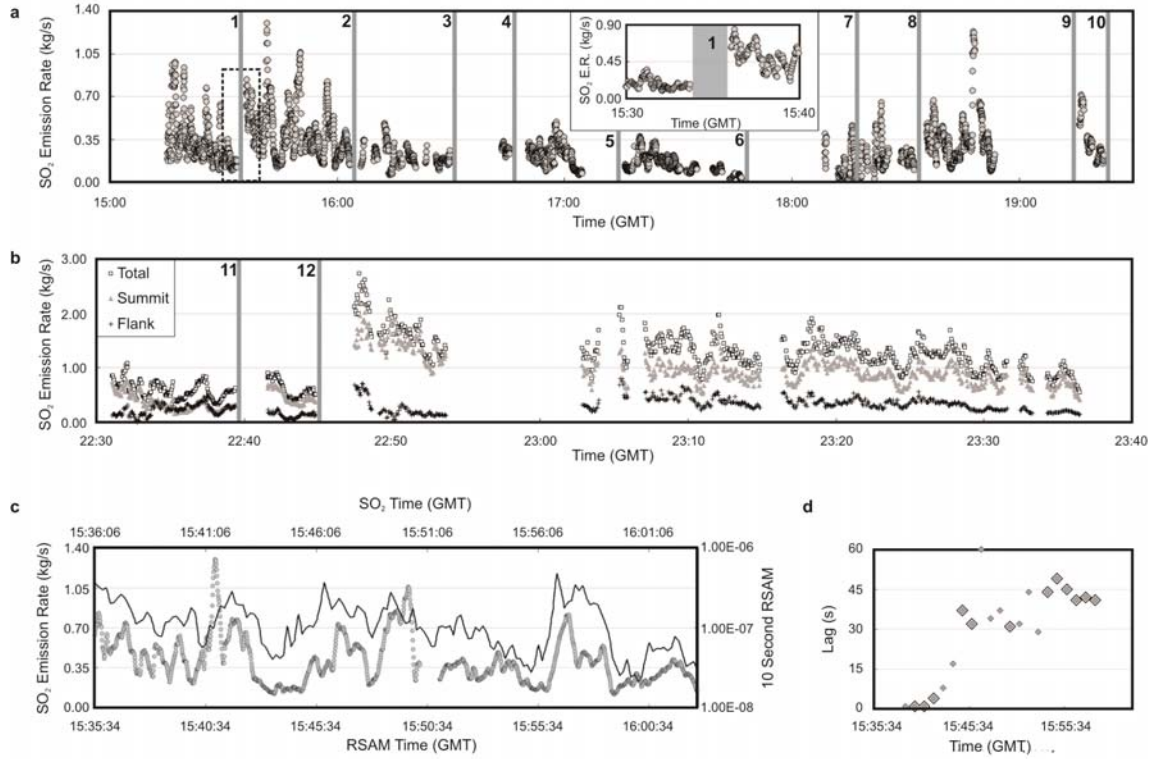


Figure 3.2: SO_2 emission rates from Fuego volcano on 21 January 2009. Portions of plots with no SO_2 data reflect periods of meteorological cloud or ash in the field of view or pauses in data acquisition for calibration. Note different x- and y-scales for a, b, and c. (a) Emission rates of SO_2 (circles) plotted alongside explosion occurrences (vertical gray lines; numbered for reference). Dashed box denotes subset region shown in inset. (b) Emission rates of SO_2 when emissions from distinct plumes were identified. (c) Example of ~ 30 minute period of similarity between SO_2 emission rate (circles) and low-frequency 10 second average seismic amplitude (RSAM; black line). Note 32 s offset between x-axes to compensate for overall lag. (d) Increasing lag between RSAM and SO_2 emission rate for time period in c. Lags were calculated using a moving 6.5-minute window with 5.5-minute overlap. Diamonds with outline represent lags with a correlation coefficient greater than 0.65.

explosions were followed by increased gas emissions (Figure 3.2a, b, Figure E.2). Though atmospheric effects (e.g., ponding of gas in the crater before buoyant rise) may cause variations in measurements, they are likely negligible given the small crater size.

Under favorable conditions, two vents with distinct eruptive and degassing behaviors (Figure 3.1a, Figure 3.2b) could be distinguished: one at the summit and one <100 m west on the flanks. Passive emissions were variable and included periods of high correlation between the vents' emission patterns (Figure 3.2b). While explosions originated only from the summit vent (left in Figure 3.1a) and summit vent emissions usually dominated, we also observed a short time (~5 min prior to explosion 11) during which summit emissions decreased such that flank emissions equaled or exceeded summit emissions. For the short time distinct plumes were visible, flank vent degassing appeared mostly unaffected by pre-explosive summit activity.

Explosion signals and continuous ~1–5 Hz tremor of variable amplitude dominated seismicity. Tremor was occasionally harmonic with >10 overtones and particle motions were consistent with surface waves, suggesting a relatively shallow source. We also find that seismic tremor and SO₂ emission rate correlate on a scale of minutes (Figure 3.2c). Though correlation is not always present, it appears repeatedly over the course of the measurements and persists over time scales ranging from ~10 minutes to ~2 hours. This correlation occurs during both harmonic (HT) and non-harmonic tremor (NHT), though is more commonly associated with NHT. The datasets are most similar when the magnitude of each is relatively high; this may be a consequence of smaller puffs (i.e., small emission rate changes relative to low background) in SO₂ data being diluted or mixed with ambient air to the extent that their integrity is lost prior to rising above the crater rim to the point of measurement by the UV camera. During periods of uniformly high RSAM, correlation is less obvious. In such instances, SO₂ emission rate varies while RSAM remains high, possibly indicating another source of seismicity overprinting the gas-sourced signature.

We quantified the similarity between the RSAM and SO₂ time-series, calculated time lags, and evaluated possible implications. One instance of data similarity occurred over ~30 minutes between explosions 1 and 2; cross-correlation of data from this interval yielded a maximum correlation of 0.6 with SO₂ lagging 32 s behind seismicity. Other periods had lags between 5 and 83 s. Application of smaller moving windows (3-9 min) to the ~30 minute dataset revealed increasing lags, from a few to ~60 s (Figure 3.2d). The progressive increase implies increasing distance between the tremor generation depth and the vent, decreasing rise speed of SO₂ from a stationary site of tremor generation, or both.

3.5 Discussion and Conclusions

We observe correlation between RSAM and SO₂ emission rates that links degassing and seismogenic tremor processes. Fluid flow [Julian, 1994; 2000], bubble coalescence [Ripepe and Gordeev, 1999], oscillation of bubbles or bubble clouds [Chouet, 1996], and conduit resonance [Chouet, 1992] have previously been invoked to explain HT and NHT signals. Tremor has also been linked to outgassing activity [Metaxian *et al.*, 1997; Palma *et al.*, 2008]. A resonant crack containing bubbly fluid can possess a sufficiently large impedance contrast to sustain tremor [Kumagai and Chouet, 2000]. In most such tremor models, higher bubble concentrations or more rapid flow of bubbles and bubble-rich fluid generate stronger tremor. It follows that more numerous or larger volumes of bubbles producing larger amplitude tremor signals would, after rising through the conduit, result in a greater SO₂ emission rate (Figure 3.2c). These processes are non-destructive and may be continuous, in agreement with the persistence of tremor both prior to and immediately following explosions at Fuego.

In addition to correlation with tremor, both long- and short-term decreases in SO₂ emissions were observed prior to explosions (Figure 3.2a, Figure E.2): from 6.4 kg/s to 0.31 kg/s over ~1.5 hrs (explosion 14), and from 2.6 to 0.36 kg/s in ~4 min (explosion 16). One way to explain this is by variable gas supply, which could result from variable magma and/or

bubble ascent rates, variable spatial distribution of gas in the conduit, or both. Non-uniform distribution of gas in magma is not unreasonable; bubbles in basaltic melts may concentrate into layers or clusters with instabilities causing further variability in bubble distribution [Manga, 1996]. If bubble layers collapse into large gas slugs, the slugs could burst through crater backfill, causing ash-rich explosions [Patrick *et al.*, 2007]. However, when time-series from separate vents are examined, similarity between degassing patterns at the two vents, which indicates some degree of coupling, disappears prior to explosion 11 (Figure 3.2b); the only anticorrelation between emissions from the vents occurred immediately prior to explosion 11 ($r = -0.51$ for 179 samples over ~ 8 minutes), when flank vent emissions were relatively high. In contrast, the highest correlation occurred immediately following explosion 12 ($r = 0.76$ for 100 samples over ~ 6 minutes). If short-term variations in SO_2 emission rate are the surface expression of variable bubble concentrations within the magma column, instances when highly correlated SO_2 emission rates dominate may be indicative of uninhibited gas release from both vents, while periods of dissimilar SO_2 time-series may represent inhibition of gas release from the summit.

Based on our observations of Fuego's activity, we have developed a model for small, ash-rich explosions (Figure 3.3). We consider background activity to be free degassing from both vents (Figure 3.3a). Given the absence of effusive activity, we assume magma supply was low during our field campaign, and such conditions may lead to enhanced cooling, degassing, crystallizing, or 'stiffening' of magma in the conduit. These rheological changes would hinder bubble ascent, partially sealing the main conduit as bubbles accumulate under a rheological boundary below the summit vent (Figure 3.3b). Increased viscosity in the upper conduit may slow magma convection, thereby further decreasing the supply of gas to the summit. Small variations in SO_2 emission overprinting longer-term (~ 30 min) trends would represent heterogeneous distribution of gas in the conduit, minor variations in gas-rich magma ascent rates, or both. Once sufficient pressurized gas collected beneath the stiffened layer to overcome the confining pressure of the viscous magma, an explosion would occur,

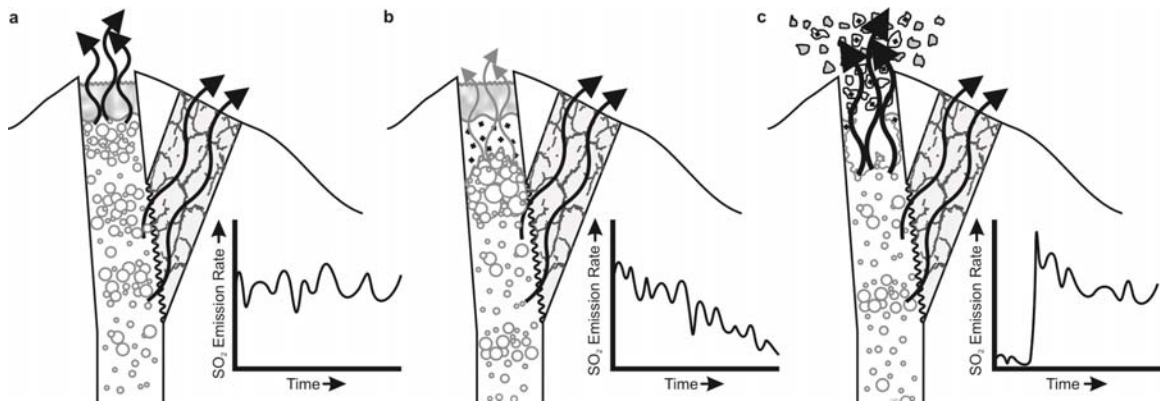


Figure 3.3: Schematic model of gas release and explosion generation for small ash-rich explosions at Fuego volcano, with theoretical SO₂ release over time. (a) Both vents degas freely. (b) Rheological stiffening in upper conduit inhibits gas release from summit; flank degassing is unaffected. (c) Pressure beneath stiffened magma overcomes confining pressure, resulting in ash-rich explosion and release of accumulated gas before a return to free degassing.

ejecting ash and bombs comprising mostly-solidified magma from the upper conduit and previously ejected crater infill. Gas emissions would peak initially, reflecting release of gas collected beneath the stiffened layer, and then drop to levels associated with gas release from the free magma surface (Figure 3.3c).

The general increase in lag between tremor and SO₂ time series that accompanies decreasing SO₂ emission is consistent with our model of progressive rheological stiffening. The increased lag suggests that the tremor source deepens or the velocity of escaping gas decreases following large explosions. Progressive cooling and/or crystallization would propagate downward through time from the top of the magma column, gradually inhibiting upward migration of gas and possibly increasing the depth of the tremor source. Variable inter-explosion times may be due to arrivals of varying amounts of pressurized gas beneath sealing layers with different degrees of stiffening and confining pressures, and instances of sustained jetting may reflect a relatively large build-up of bubbles such that their extended release is akin to the collapsing foam of *Jaupart and Vergnolle* [1988]. Flank degassing may be a result of persistent degassing through a crack network in magma solidified following a lava flow in mid-2008 (Figure 3.3b), which would not be subject to stiffening and would be largely unaffected by summit activity.

Similar magma stiffening or solidification in the upper conduit and subsequent pressurization has been inferred to be the source of ash-rich explosions in eruption sequences at Mt. Etna (Italy) [*Tadducci et al.*, 2004]. Ash-rich explosions and associated SO₂ emissions at Karymsky volcano (Russia) have been attributed to the repeated presence of viscous, capping plugs [*Fischer et al.*, 2002], while gas pistoning at Kilauea volcano (Hawaii) is also theorized to be caused by a build-up of gas beneath a rheological boundary [*Johnson et al.*, 2005] despite magma of a relatively low viscosity; similar stiffening of magma and ensuing inhibition of gas release is thus also conceivable at Fuego.

Work conducted at Fuego volcano highlights the impact of integrating UV cameras into volcanological field campaigns. By supplementing seismic and visual observations with

high-resolution SO₂ emission rates, we identified the presence of linked source processes for tremor and degassing; isolated vents with distinct behaviors; and detected gas emission decreases prior to explosions that likely result from rheological stiffening within the upper conduit. This interdisciplinary approach involving UV cameras may yield similar results at other volcanoes, thereby providing new information about eruption mechanism and aiding model validation.

3.6 Acknowledgements

Research was supported by NSF PIRE 0530109. Additional funding included a Grant-In-Aid of Research from Sigma Xi, The Scientific Research Society; a Geological Society of America Graduate Student Research Grant; and a grant from the Michigan Space Grant Consortium. We thank E. Barrios, K. Brill, A. Calderas, G. Chigna, M. Dalton, J. Erdem, J. Lyons, J. Richardson, and J. Silverman for assistance with field work; INGUAT and INSIVUMEH for logistical support; M. Dalton, and R. Escobar Wolf for useful discussions; and J. Johnson and K. Roggensack for constructive reviews that improved this paper.

3.7 References

- Andres, R. J., W. I. Rose, R. E. Stoiber, S. N. Williams, O. Matías, and R. Morales (1993), A summary of sulfur dioxide emission rate measurements from Guatemalan volcanoes, *Bull. Volcanol.*, 55(5), 379-388.
- Bluth, G. J. S., J. M. Shannon, I. M. Watson, A. J. Prata, and V. J. Realmuto (2007), Development of an ultra-violet digital camera for volcanic SO₂ imaging, *Journal of Volcanology and Geothermal Research*, 161(1-2), 47-56.
- Chouet, B. A. (1992), A seismic model for the source of long-period events and harmonic tremor, in *Volcanic Seismology*, edited by P. Gasparini, R. Scarpa and K. Aki, pp. 133-156, Springer, New York.
- Chouet, B. A. (1996), New methods and future trends in seismological volcano monitoring, in *Monitoring and Mitigation of Volcano Hazards*, edited by R. Scarpa and R. Tilling, pp. 23-98, Springer-Verlag, Berlin.

Chapter 3 – Linking Tremor, Degassing, and Eruption Dynamics

- Dalton, M. P., I. M. Watson, P. A. Nadeau, C. Werner, W. Morrow, and J. M. Shannon (2009), Assessment of the UV camera sulfur dioxide retrieval for point source plumes, *Journal of Volcanology and Geothermal Research*, 188(4), 358-366.
- Endo, E. T., and T. Murray (1991), Real-Time Seismic Amplitude Measurement (RSAM) - a volcano monitoring and prediction tool, *Bulletin of Volcanology*, 53(7), 533-545.
- Fischer, T. P., M. M. Morrissey, M. L. Calvache, D. Gomez, R. Torres, J. Stix, and S. N. Williams (1994), Correlations between SO₂ flux and long-period seismicity at Galeras Volcano, *Nature*, 368(6467), 135-137.
- Fischer, T. P., K. Roggensack, and P. R. Kyle (2002), Open and almost shut case for explosive eruptions: Vent processes determined by SO₂ emission rates at Karymsky volcano, Kamchatka, *Geology*, 30(12), 1059-1062.
- Jaupart, C., and S. Vergnolle (1988), Laboratory models of Hawaiian and Strombolian eruptions, *Nature*, 331(6151), 58-60.
- Johnson, J. B., A. J. L. Harris, and R. P. Hoblitt (2005), Thermal observations of gas pistonning at Kilauea Volcano, *Journal of Geophysical Research-Solid Earth*, 110, B11201.
- Julian, B. R. (1994), Volcanic tremor - Nonlinear excitation by fluid-flow, *Journal of Geophysical Research-Solid Earth*, 99(B6), 11859-11877.
- Julian, B. R. (2000), Period doubling and other nonlinear phenomena in volcanic earthquakes and tremor, *Journal of Volcanology and Geothermal Research*, 101(1-2), 19-26.
- Kumagai, H., and B. A. Chouet (2000), Acoustic properties of a crack containing magmatic or hydrothermal fluids, *Journal of Geophysical Research-Solid Earth*, 105(B11), 25493-25512.
- Lyons, J. J., G. P. Waite, W. I. Rose, and G. Chigna (2010), Patterns in open vent, strombolian behavior at Fuego volcano, Guatemala, 2005-2007, *Bulletin of Volcanology*, 72(1), 1-15.
- Manga, M. (1996), Waves of bubbles in basaltic magmas and lavas, *Journal of Geophysical Research-Solid Earth*, 101(B8), 17457-17465.
- Metaxian, J. P., P. Lesage, and J. Dorel (1997), Permanent tremor of Masaya Volcano, Nicaragua: Wave field analysis and source location, *Journal of Geophysical Research-Solid Earth*, 102(B10), 22529-22545.
- Mori, T., and M. Burton (2006), The SO₂ camera: A simple, fast and cheap method for ground-based imaging of SO₂ in volcanic plumes, *Geophysical Research Letters*, 33(24), L24804.

Chapter 3 – Linking Tremor, Degassing, and Eruption Dynamics

- Palma, J. L., E. S. Calder, D. Basualto, S. Blake, and D. A. Rothery (2008), Correlations between SO₂ flux, seismicity, and outgassing activity at the open vent of Villarrica volcano, Chile, *Journal of Geophysical Research-Solid Earth*, 113(B10), B10201.
- Parfitt, E. A., and L. Wilson (1995), Explosive volcanic eruptions-IX. The transition between Hawaiian-style lava fountaining and Strombolian explosive activity, *Geophysical Journal International*, 121(1), 226-232.
- Patrick, M. R., A. J. L. Harris, M. Ripepe, J. Dehn, D. A. Rothery, and S. Calvari (2007), Strombolian explosive styles and source conditions: insights from thermal (FLIR) video, *Bulletin of Volcanology*, 69(7), 769-784.
- Ripepe, M., and E. Gordeev (1999), Gas bubble dynamics model for shallow volcanic tremor at Stromboli, *Journal of Geophysical Research-Solid Earth*, 104(B5), 10639-10654.
- Rodriguez, L. A., I. M. Watson, W. I. Rose, Y. K. Branan, G. J. S. Bluth, G. Chigna, O. Matias, D. Escobar, S. A. Carn, and T. P. Fischer (2004), SO₂ emissions to the atmosphere from active volcanoes in Guatemala and El Salvador, 1999-2002, *Journal of Volcanology and Geothermal Research*, 138(3-4), 325-344.
- Rose, W. I., A. T. Anderson, L. G. Woodruff, and S. B. Bonis (1978), October 1974 basaltic tephra from Fuego Volcano - Description and history of the magma body, *Journal of Volcanology and Geothermal Research*, 4(1-2), 3-53.
- Rose, W. I., S. Self, P. J. Murrow, C. Bonadonna, A. J. Durant, and G. G. J. Ernst (2008), Nature and significance of small volume fall deposits at composite volcanoes: Insights from the October 14, 1974 Fuego eruption, Guatemala, *Bulletin of Volcanology*, 70(9), 1043-1067.
- Taddeucci, J., M. Pompilio, and P. Scarlato (2004), Conduit processes during the July-August 2001 explosive activity of Mt. Etna (Italy): inferences from glass chemistry and crystal size distribution of ash particles, *Journal of Volcanology and Geothermal Research*, 137(1-3), 33-54.
- Williams-Jones, G., J. Stix, M. Heiligmann, J. Barquero, E. Fernandez, and E. D. Gonzalez (2001), A model of degassing and seismicity at Arenal Volcano, Costa Rica, *Journal of Volcanology and Geothermal Research*, 108(1-4), 121-139.

Chapter 4: EXAMINING THE ROLE OF DEGASSING IN RECENT SUMMIT ACTIVITY, KILAUEA VOLCANO, HAWAII

4.1 Abstract

UV camera measurements at Kilauea volcano, Hawaii, in May of 2010 captured two occurrences of lava filling and draining within the summit vent. During high lava stands we observed diminished SO₂ emission rates, decreased seismic and infrasonic tremor, minor deflation of the entire summit area, and slowed motion of the convecting lava lake surface. Similar events at Kilauea and other volcanoes, and in modeling experiments, have been linked to deep gas slug rise, gas accumulation beneath a viscous crust, cyclic pressure variations, and variable convection regimes. Incorporation of UV camera data into a multi-parameter dataset gives credence to the likelihood of shallow gas accumulation as the cause of such events. Further, high stand events are just one type of degassing on a spectrum of degassing intensity that trigger VLP seismicity in a similar manner.

4.2 Introduction

Kilauea volcano is the youngest subaerial volcano along the Hawaiian hotspot track. Located on the Big Island of Hawaii on the southeastern flank of the larger Mauna Loa volcano, Kilauea has been in a constant state of eruption since 1983, and activity is diverse, ranging from fissure eruptions with multiple lava fountains, to lava lakes, to more passive effusion via tubes and channels. Since March 2008, simultaneous summit and flank eruptions have marked activity. An increase in summit SO₂ emission rates and tremor beginning in late 2007 culminated with a small explosive event on March 19, 2008. The explosion resulted in the opening of a ~35 m wide vent in the Halema`uma`u summit crater [Wilson *et al.*, 2008]. A persistent gas plume emanates from the vent, often carrying with it very small amounts of juvenile tephra. In the early stages of the eruption, passive degassing was interrupted from

Chapter 4 – Kilauea Degassing and Summit Activity

time to time by explosive degassing bursts, during which the normally white plume was darkened by increased amounts of ash and ejecta.

The degassing bursts generate VLP events in both the seismic and infrasound records, which have been the subject of multiple studies. *Chouet et al.* [2010] identify a dual-crack model at ~1 km depth as the likely source of VLP seismicity, with the rise, expansion, and bursting of a large gas slug stimulating the VLP oscillations and inducing the ashy degassing bursts. *Patrick et al.* [2011b] also assert that VLP seismicity associated with the degassing bursts is brought about by the bursts themselves, but contend that accumulation of gas beneath a rheological boundary and subsequent violent overturn of the gas-rich layer are responsible for the degassing bursts. Video records indicate that the collapse of large chunks of the crater wall can trigger such overturns, as well as smaller episodes of vigorous degassing and tremor [*Patrick et al.*, 2011b].

Despite the reliance of both models on the release of gas, absent from work thus far is a multi-parameter approach that integrates seismic and other geophysical data with gas emission rate information. Using high temporal resolution SO₂ emission rate data from May 2010, we describe a variant of the episodic tremor events of *Patrick et al.* [2011b]. Episodic tremor events were described by *Patrick et al.* [2011b] as five high amplitude tremor bursts over a 30 minute period (average duration ~3 minutes). Tremor amplitudes were double that of background tremor and bursts were separated by quiet periods of similar length during which tremor amplitude dropped to levels below background. The peak frequency of all tremor, including the bursts, was ~0.5 Hz. Bursts were also accompanied by VLP signals and lava level variations that displayed an inverse relationship to tremor amplitude such that lava level fell during the bursts and remained high during the quiet periods. The behavior is described as “gas pistoning” on the basis of its similarity to previous events documented at Kilauea [e.g., *Edmonds and Gerlach*, 2007; *Johnson et al.*, 2005; *Swanson et al.*, 1979].

In contrast to the short, repetitive degassing and tremor events associated with gas pistoning, longer “high stand” events began on May 18, 2010. At approximately 7:15 pm local time, the surface of the lava lake in the summit vent rose ~20 m over the course of a

few minutes. Tremor amplitude decreased markedly coincident with the rise, as during the episodic tremor cycles of *Patrick et al.* [2011b]. Once the lava lake reached its highest level, instead of releasing gas vigorously in a matter of minutes, the unperturbed lava lake remained at a constant, high level within the vent for approximately 1.25 hrs. The lava level then dropped, accompanied by vigorous degassing and a spike in tremor akin to episodic tremor. Three similar events took place in succession on May 22, 2010, with each high stand lasting 1 – 2 hrs. Inter-event periods were ~ 2.5 and 3.5 hrs, respectively. Four more events occurred from May 23 to 24, 2010, with high stands of a similar duration but only ~ 20 mins between events.

We examine SO_2 emission rates as they relate to two consecutive high-stand events on May 22, 2010. Supplementing the gas data are seismic and radial tilt data, and imagery from a web camera located on the edge of the summit crater. Seismic and web camera data are also examined for the 6 additional high-stand events for which we do not have gas data. In taking a multi-parameter approach to studying these events, we aim to determine the role of degassing in dictating the occurrence of the high-stands.

4.3 Methodology

SO_2 emission rate data were obtained via a dual-UV camera system deployed 7 km south of the degassing vent, on a scarp on Hilina Pali Road. Two Apogee Alta U6 cameras, with a 1024×1024 pixel, 16-bit, Kodak KAF-1001E-2 CCD arrays, were mounted side-by-side on a single tripod. We employed identical 105 mm focal length CoastalOpt quartz lenses, each with an angular field of view of 13.3578° , on the cameras. Each lens was outfitted with a 10 nm full-width half-max UV bandpass filter from Andover Optics. One filter had a central wavelength of 307 nm, in one of the characteristic absorption bands of SO_2 . In order to isolate the UV absorption signal of SO_2 , the second camera's filter was centered at 326 nm, where the absorption of SO_2 is ~ 2 orders of magnitude less than that at shorter wavelengths. Camera shutters were synchronized via their I/O (mini-DIN) ports, with a one second delay between image pairs to allow for data transfer to a single computer.

Calibration (using a set of seven calibration cells ranging from 0 ppm·m to 1388 ppm·m) and background sky images were collected with both cameras approximately once every two hours, or as frequently as ambient sky conditions permitted. We performed imagery post-processing for extraction of SO₂ emission rates with the UVCamSO2 suite of Matlab codes described in Chapter 2.

Seismic data were recorded by a network of permanent broadband seismometers at the summit of Kilauea. Instruments are three-component 60s Guralp CMG-40Ts collecting data at a rate of 100 Hz. Data analyzed are from the NPT station, the closest to the active vent at a distance of just under 1 km. Radial tilt data were also recorded by a tiltmeter (UWE station) located ~2 km northwest of the active vent. A map of field instrument locations relative to the Kilauea's summit features is shown in Figure 4.1.

4.4 Results

4.4.1 SO₂ emissions

Poor weather conditions limited the number of days on which UV camera data could be collected; of days with useable data, many were only partial days. In total, we were able to acquire useable camera data on 11 dates between May 5 and May 26, 2010. As the camera relies on the sunlit sky as its source of UV, data collection was also restricted to the brightest ~8-10 hours around solar noon. Because of these limiting factors, we were able to measure near-continuous SO₂ emission rate data coincident with high-stand events only on May 22. Approximately 8000 image pairs were acquired from 9:00 – 17:30 HST and we discarded ~200 that displayed interference by meteorological clouds. Data transfer speed limited the temporal resolution of imagery to ~0.3 Hz.

Measured emission rates of SO₂ on May 22 ranged from a minimum of ~0 kg/s to a maximum of 76.67 kg/s (Figure 4.2), with an overall mean of 12.75 ± 10.64 kg/s, comparable to emission rate measurements by HVO, which range from daily mean values of 9.83 kg/s (800 t/d) to 13.89 kg/s (1200 t/d) for the month of May 2010 (HVO,

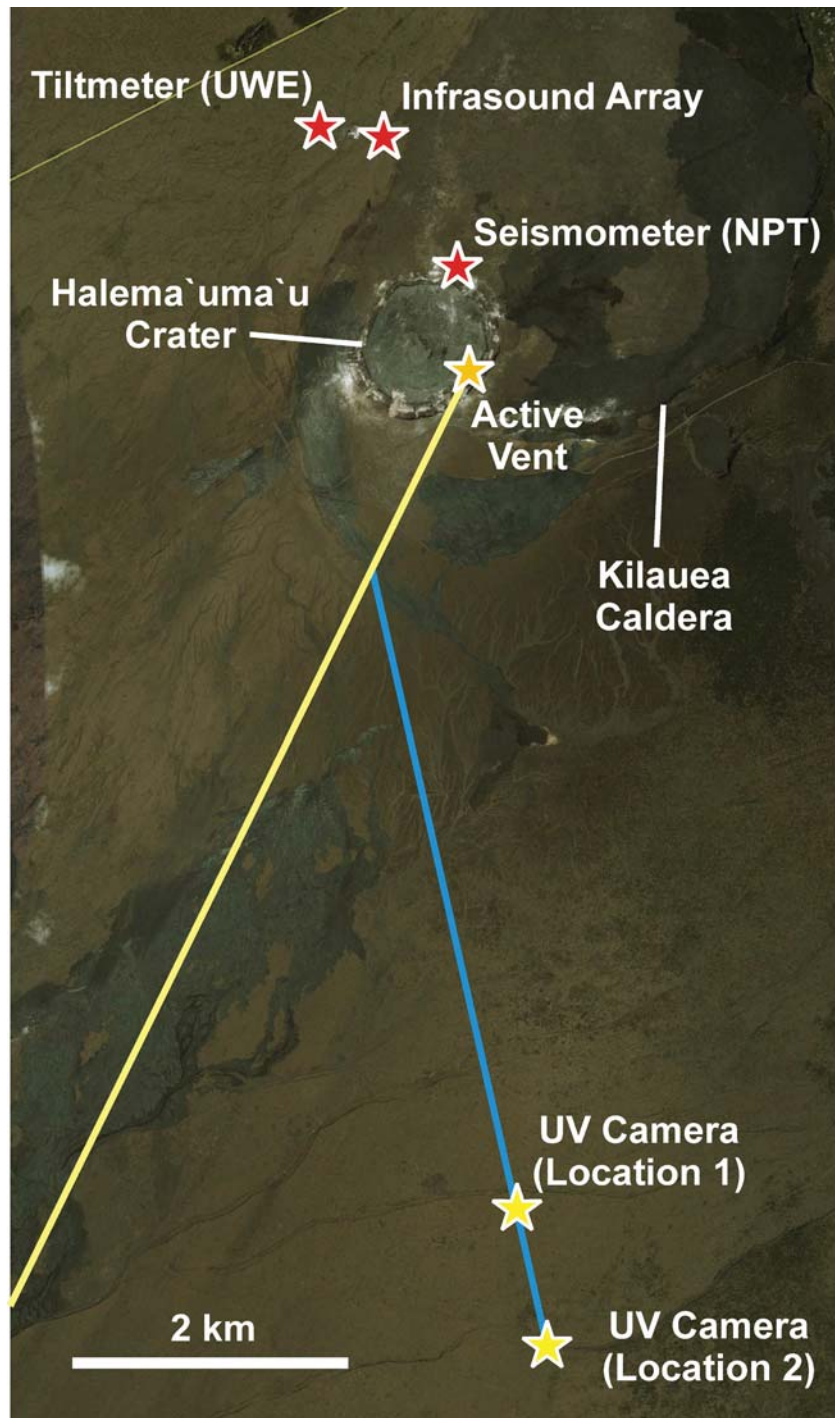


Figure 4.1: Map of Kilauea summit, showing instrument locations. Pale yellow line indicates approximate plume direction under trade wind conditions and blue line is approximate UV camera look direction.

<http://volcanoes.usgs.gov/hvo/activity/archive.php>). Of note are the striking periods of decreased emission rate that coincide with lava high stands at ~10:20 – 12:20 and ~14:50 – 16:15 HST. Mean SO₂ emissions during the two high stands are 2.99 ± 1.82 kg/s and 4.34 ± 2.47 kg/s, respectively, while the mean of SO₂ emissions, excluding the high stands, is 19.71 ± 9.11 kg/s, ~5 times that of the high stand emissions. The mean emission rate prior to the onset of the first high stand was 13.67 ± 6.79 kg/s, within 1 kg/s of the mean of the full day's emission rates.

4.4.1.1 Potential errors

While the minimum emission rate reported here is 0 kg/s of SO₂, this is an artifact of measurement geometry both at the volcano and within the imagery, and puff or other structures within the plume. Emission rates at the vent are unlikely to ever be exactly 0 kg/s and those reported here are more likely representative of inter-puff gaps within the plume following advection downwind of the vent. Also important is potential underestimation of emission rates as a result of Kilauea's low topographical profile. The plume emanates from a lava lake in a deep pit on the floor of Halema'uma'u crater, which itself is nested in the summit caldera. This fact, coupled with the Mauna Loa and Mauna Kea blocking portions of the background sky and variable topography of the summit region, limited potential locations for data acquisition. The UV camera was ultimately located 7 km south of the degassing vent, on a scarp on Hilina Pali Road. While the entirety of the plume was often lofted up into the field of view of the camera (Figure 4.3a), underestimation of emission rates likely occurs during periods when the plume was low-lying and partially obscured by topography (Figure 4.3b).

4.4.2 Seismicity

Seismicity relating to lava high stands has three distinct phases: background; high stand; and lake draining (Figure 4.4a). Background seismicity prior to the high stands is dominated by tremor below 1 Hz, with a mean tremor amplitude of $\sim 3.8 \mu\text{m/s}$. Spectral

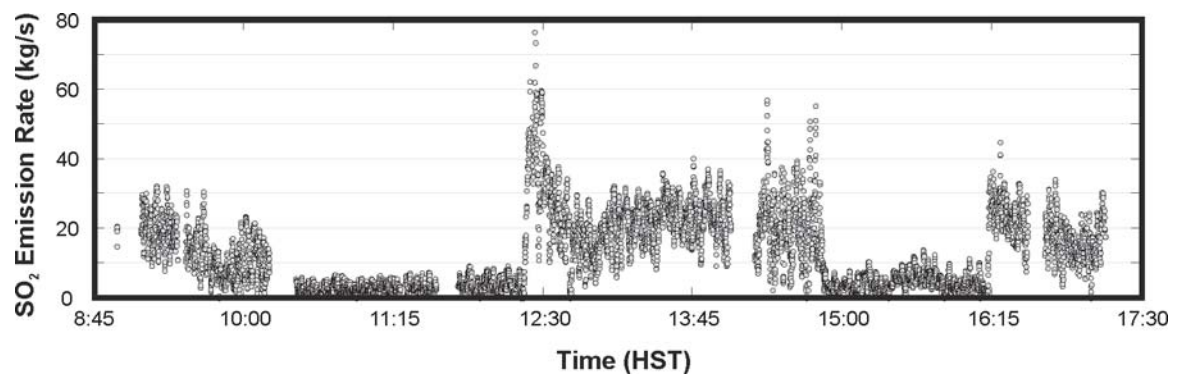


Figure 4.2: SO₂ emission rate time series from Kilauea volcano, May 22, 2010

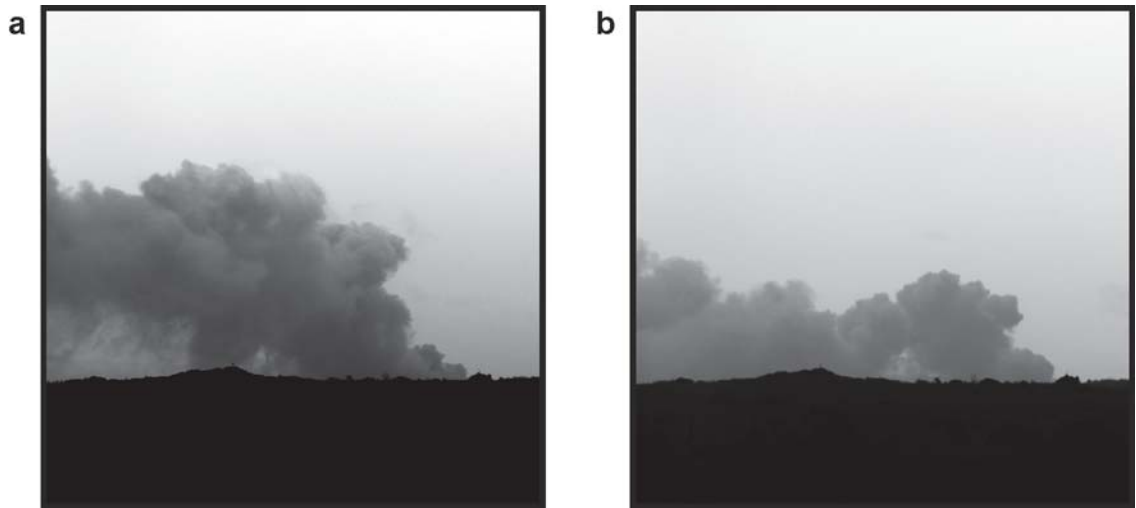


Figure 4.3: Sample plume imagery from May 22, 2010. (a) Lofting plume (b) Grounded plume, which may lead to underestimation of emission rates. Image field of view is approximately 1440 m.

analysis of the background tremor reveals consistent peaks at approximately 0.04 Hz, 0.22 Hz, 0.36 Hz, and 0.55 Hz (Figure 4.4b). These peaks are similar to dominant peaks in seismicity associated with degassing bursts in the early stages of the summit activity noted by *Chouet et al.* [2010] and *Dawson et al.* [2010]. Subordinate peaks near 1.35 and 1.5 Hz are also intermittently present. Upon onset of the high lava stand, tremor amplitude drops by a factor of four to $\sim 1.1 \mu\text{m/s}$ over the course of <120 seconds. Once at high stand, all tremor bands drop off markedly except 0.22 Hz, which appears unaffected by the lava lake activity (Figure 4.4c). Intermittent higher frequency transient events that do not affect the high stand also may occur. The end of the high stand is marked by a sudden burst of broadband energy. Amplitude increases to an average of $8 \mu\text{m/s}$ over $\sim 20 - 40$ seconds. Dominant tremor bands similar to those of pre-high stand seismicity return (though the 0.36 and 0.55 Hz peaks appear to either merge into a single broader peak centered near 0.41 Hz or retain the 0.36 Hz peak while the 0.55 Hz peak independently shifts lower to 0.41 Hz), at higher amplitudes than previously, with the addition of enhanced signals at ~ 1.3 and ~ 1.5 Hz (Figure 4.4d). After a period of ~ 5 minutes, tremor returns to levels at or near that of pre-high stand background with the same spectral signature.

4.4.3 Infrasound and tilt

A small (~ 30 m) 3-microphone infrasound array was deployed near HVO, ~ 2 km from the degassing vent. However, ambient wind levels contributed much noise to the data on May 22, making any signal related to the high stand events unidentifiable. *Patrick et al.* [2010] report that infrasound data recorded ~ 7 km from Halema`uma`u during similar events in November of 2010 mimic seismic traces, with sudden drop-offs in amplitude coincident with the onset of the lava lake high stands and bursts of energy upon termination of the high stand. Even in the absence of a distinct signal corresponding to the high stands on May 22 in infrasound traces, the dominant 0.3 Hz signal present in infrasound recorded at ~ 7 km during background degassing disappears during high stands, indicating the cessation of normal degassing (D. Fee, pers. comm., 2011).

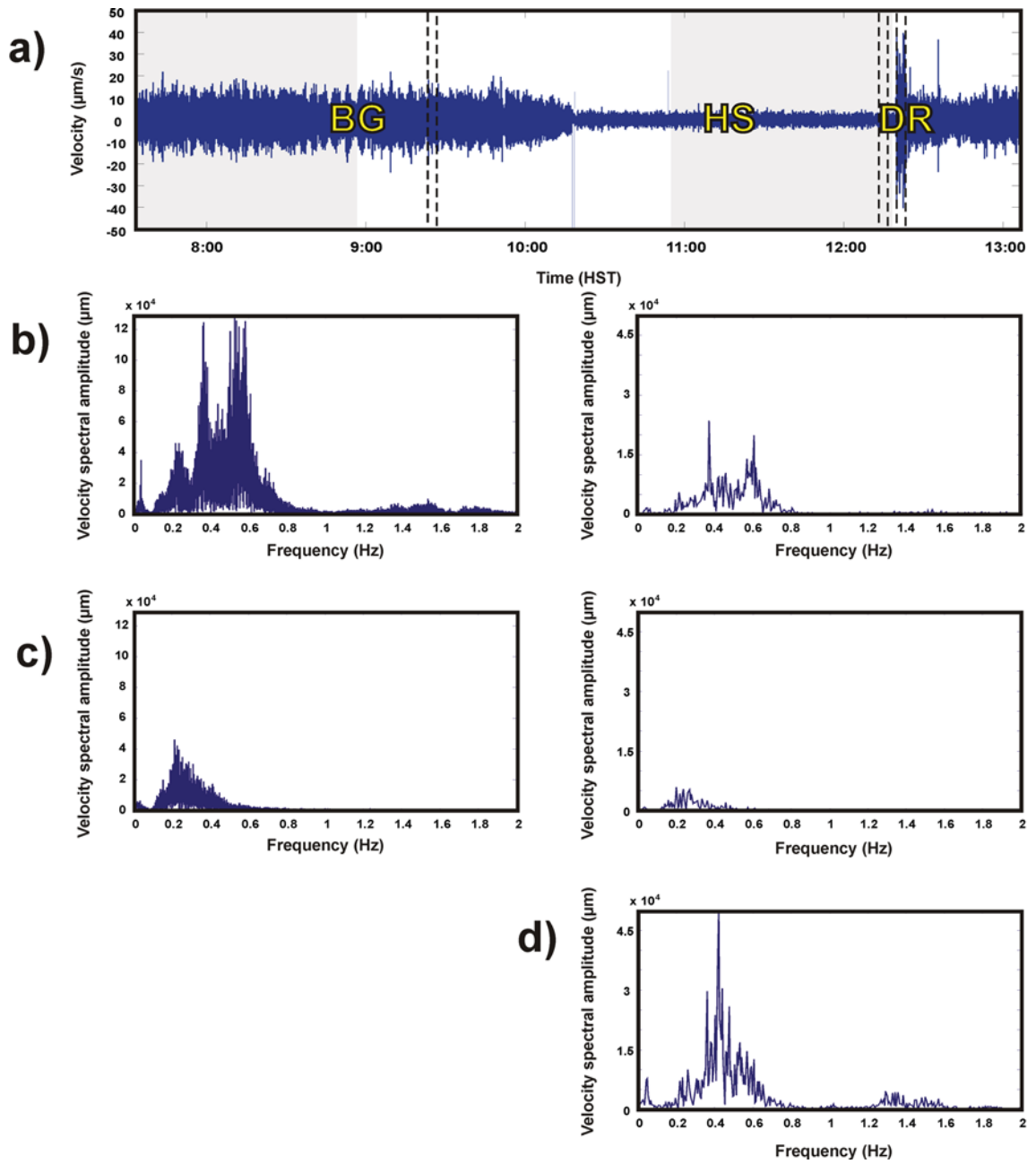


Figure 4.4: Three phases of high stand seismicity, with spectral characteristics. (a) Seismic trace spanning first high stand on May 22, 2010. BG denotes background level tremor prior to the high stand, HS is high stand, and D is draining. Shaded areas indicate the 5000 s duration subsets used for calculation of long-term spectra; dashed boxes are 200 s subsets for short-term spectra. (b) Spectra for background tremor over 5000 and 200 s, left to right. (c) Spectra for high stand tremor over 5000 and 200 s, left to right. (d) Spectrum for draining over 200 s. A longer 5000 s spectrum could not be determined, as draining events occur over a short duration.

Chapter 4 – Kilauea Degassing and Summit Activity

Radial tilt data from the Uwekahuna vault, ~2 km from the vent, also reveals changes coincident with lava high stands. Although superimposed on much longer and larger amplitude changes in tilt related to frequent deflation-inflation (DI) events (which themselves may be related to variability in the supply of gas-rich magma from depth [Poland *et al.*, 2011]), the initiation of high stands are typically marked by a small (~ 0.02 μrad) deflation of the entire summit area. Termination of the high stands coincides with a compensatory small inflation.

4.4.4 Vent rim camera

A low-light sensitive web camera was installed on the rim of Halema`uma`u crater, overlooking the active vent and lava surface on September 11, 2009. Lava lake level rise is observable in the imagery for May 2010, though daytime imagery, including on May 22, is often obscured by the thick gas plume (Figure 4.5). Nighttime imagery is much clearer and displays the ~ 20 m height change from events similar to those measured on May 22 (Figure 4.6). Web imagery is refreshed on the public website every 5 minutes with higher resolution data (4 frames/second) archived by HVO. A software mishap resulted in overwriting of the high resolution imagery from April and May of 2010 and data was thus unavailable for further analysis for the specific high stands being examined here (K. Wooten, pers. comm., 2011). Analysis of other high stand events, via tracking of movements of cracks in the solid lava lake surface, indicates that surface motion of the lava lake slows during the increase in lava level and remains below average until the cessation of the high stand [Patrick *et al.*, 2010]. Imagery from a second web camera stationed at HVO overlooking the summit of Kilauea indicates that despite the depth of the lava lake surface in the vent, bright glow typically emanates from the vent at night. During high stands, though lava is closer to the surface, glow as seen from HVO is markedly diminished, likely a result of the diminished plume opacity providing less opportunity for reflection and scattering of the lake surface's glow.

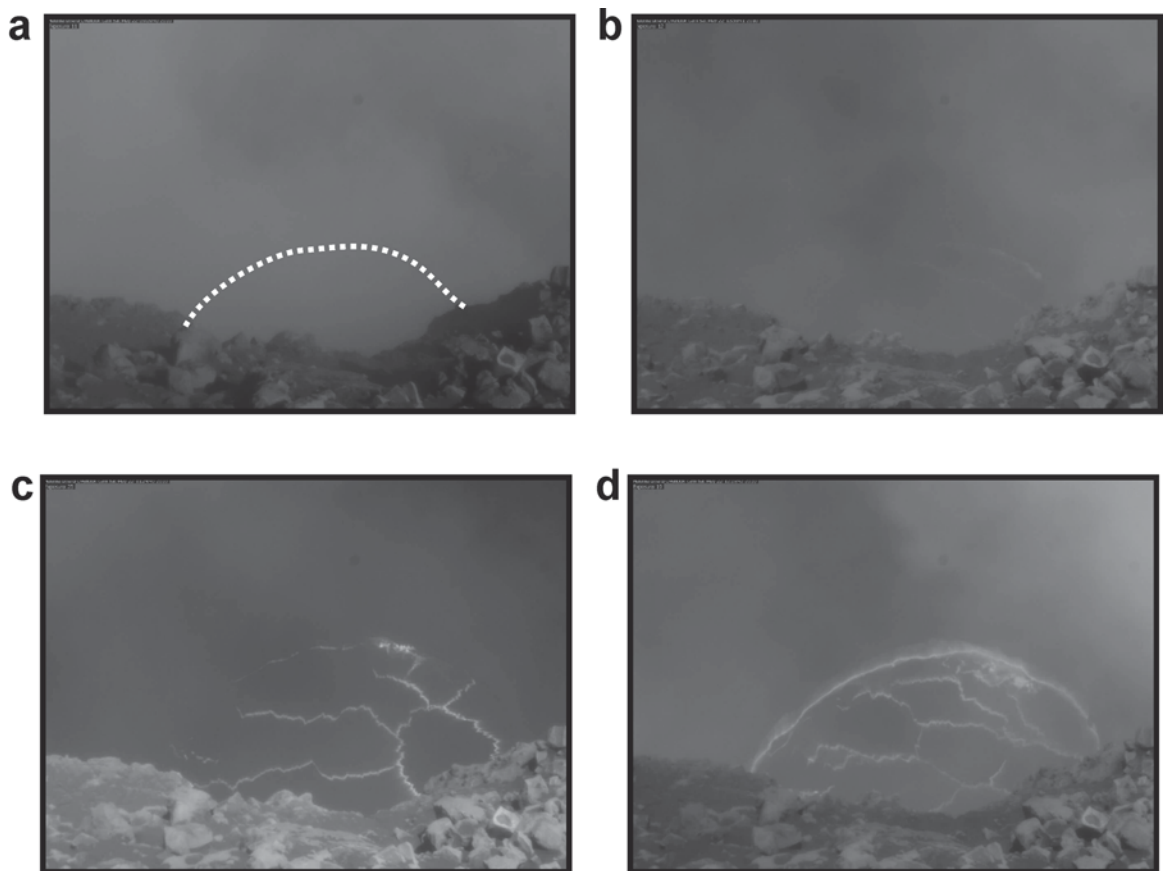


Figure 4.5: Sequence of HVO web camera images from a high stand on May 22, 2010, during UV camera data acquisition. (a) Lava at low stand, or base level, obscured by the plume. Dotted line indicates edge of lava lake. (b) Lava at low stand, barely visible through plume. (c) Lava at high stand. Note brightly-lit rocks in image foreground, as plume is diminished, allowing sunlight to illuminate ground surface. (d) Onset of lava draining.

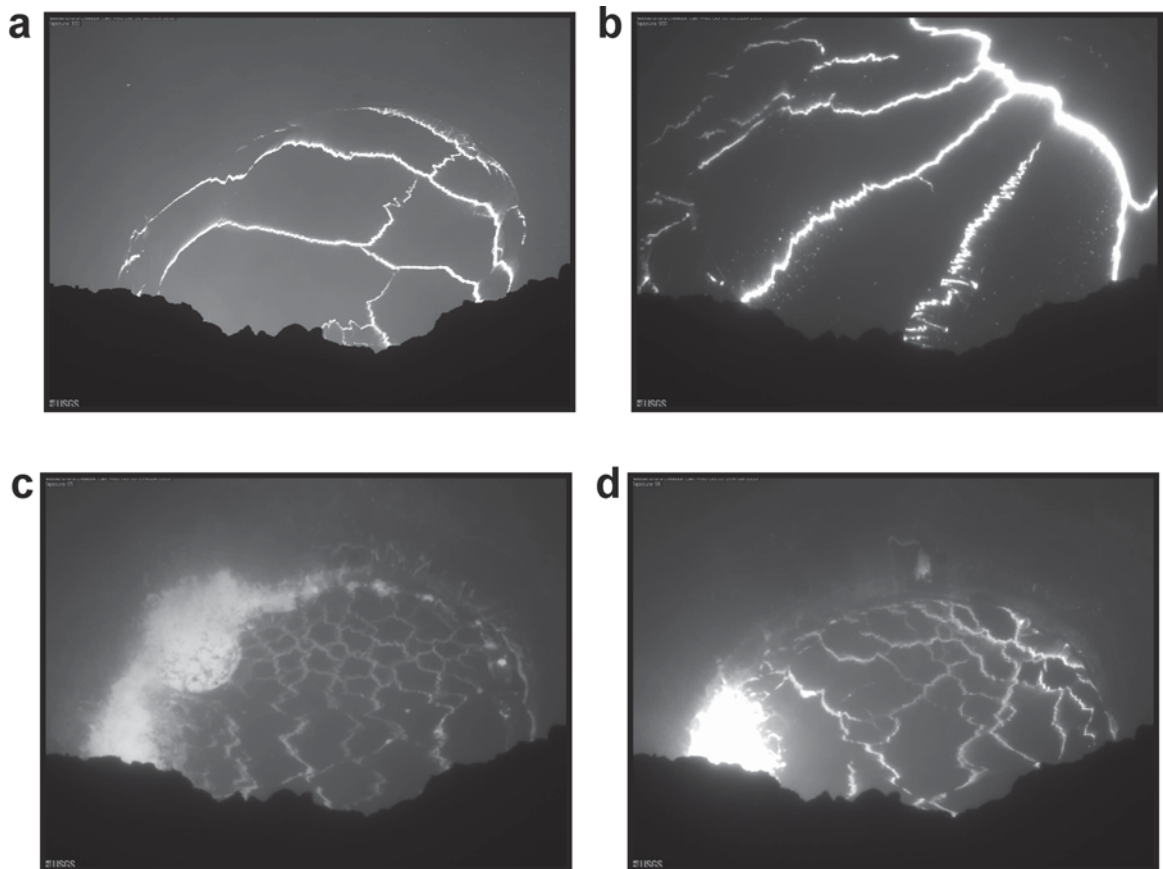


Figure 4.6: Sequence of HVO web camera images from a high stand during the night of October 5 – 6, 2010, illustrating clarity of web camera in the absence of sunlight. (a) Lava at low stand, or base level. (b) Lava ~20-30 m higher in vent at high stand. (c) Lava draining back to base level. Note preferential spattering and gas escape at edge of lake along conduit wall. (d) Lava post-high stand, back down to near base level, with some continued spatter along conduit wall.

4.4.5 High stand summary

Eight times during the measurement period in May, 2010, the lava lake level in the vent in Halema`uma`u crater increased by ~20 m. Lava remained at the high level for 1 – 2 hours each time before dropping suddenly back to its base level. In Table 4.1 we summarize pertinent observations relating to the high stands. Coincident datasets for the rise and fall phases of the second high stand on May 22, 2010 are shown in Figure 4.7 and Figure 4.8 respectively.

4.5 Discussion

4.5.1 Models for gas pistoning

Rise and fall of lava lakes in various manners, or “gas pistoning,” has been noted at Kilauea many times, associated with different eruptions for at least a century [e.g., *Barkeet et al.*, 2003; *Edmonds and Gerlach*, 2007; *Johnson et al.*, 2005; *Patrick et al.*, 2011a; *Perret*, 1913; *Swanson et al.*, 1979]. The events are generally described as the slow rise of the lava free surface within a narrow conduit, driven by a buoyant gas slug or high concentration of bubbles. Upon lava reaching the top of the conduit, lava spills over to the surrounding area, thereby thinning the lava overburden above the gas pocket and allowing the pressurized gas beneath to break through the lava above. The gas is released violently, accompanied by lava spatter and heightened seismicity in a characteristic spindle shape [*Chouet and Shaw*, 1991; *Ferrazzini et al.*, 1991], until the gas is depleted and, depending on vent morphology, lava has drained back into the conduit [*Johnson et al.*, 2005; *Swanson et al.*, 1979]. Several models have been proposed to explain gas pistoning at Kilauea specifically, as well as similar activity at other volcanoes. Below we examine these models as they pertain to our observations of lava high stands and assess the plausibility of each as the mechanism driving the high stands.

4.5.1.1 Slug rise

Edmonds and Gerlach [2007] were able to determine the gas compositions associated with several styles of degassing at Pu`u `O`o from late 2005 to early 2005. Fourier

Chapter 4 – Kilauea Degassing and Summit Activity

Table 4.1: Summary of geologic observations of lava high stand events

	<u>Background</u>	<u>High Stand</u>	<u>Draining</u>
Lava Level	~150 m deep	↑ (~20 m)	↓ (~20 m)
Seismic Amplitude	~2 $\mu\text{m/s}$	↓ (factor of ~4)	↑↑, then ↓ to background
SO₂ Emissions	~14 kg/s	↓ (factor of ~4)	↑↑, then ↓ to background
Lake Surface Velocity	0.2 – 0.6 m/s	↓	↑
Tilt	Variable	↓ (0.02 μrad)	↑
Infrasound	Variable, with wind	↓	↑↑, then ↓ to background
Vent Glow (Night)	Bright	↓	↑
Plume Appearance	Thick, whitish	Wispy to invisible	Very thick

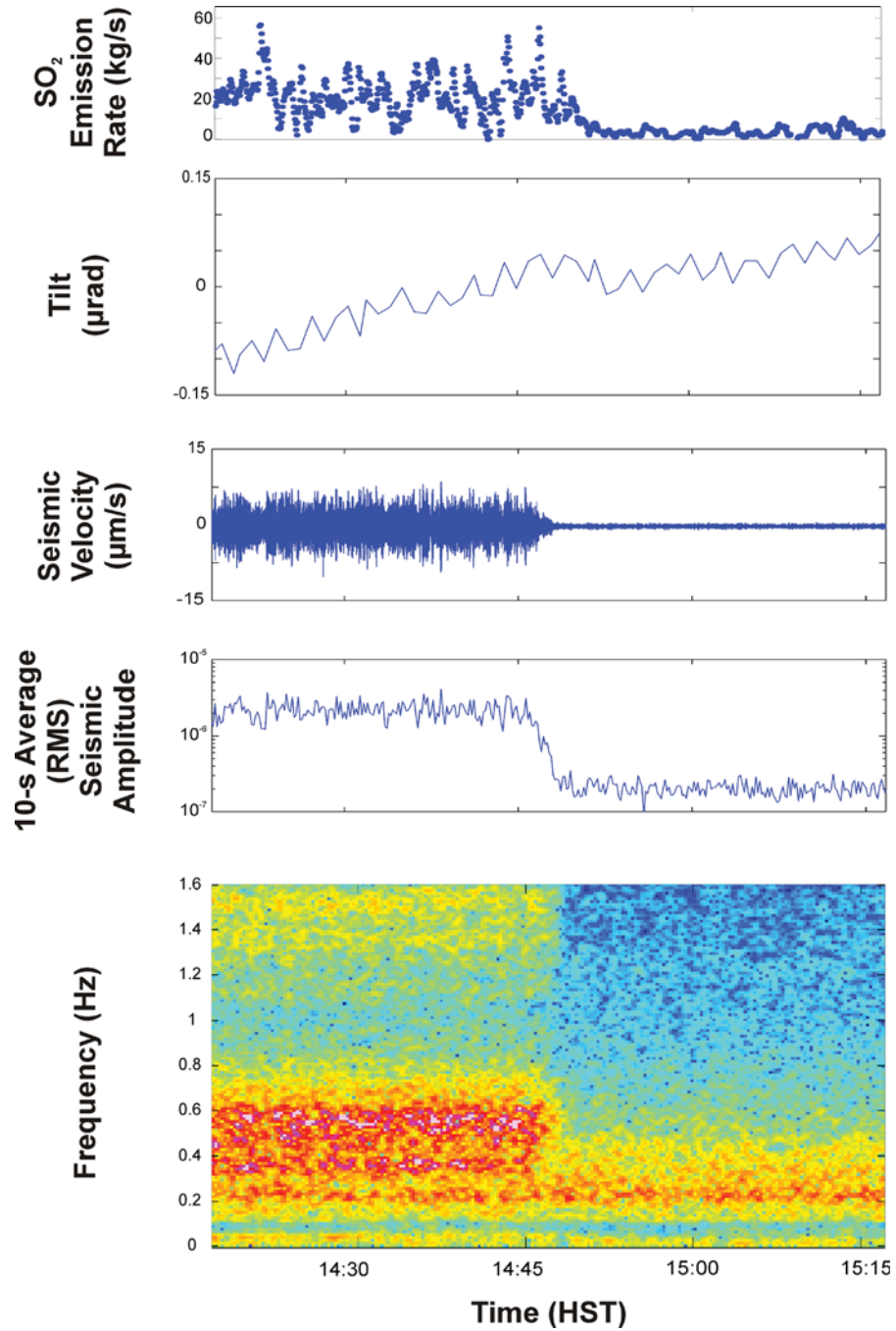


Figure 4.7: SO₂ emission rate, radial tilt, and seismicity for onset of second lava high stand, May 22, 2010. Bottom panel is a spectrogram of seismic data; cool and warm colors are weak and strong seismicity at the corresponding time and frequency, respectively.

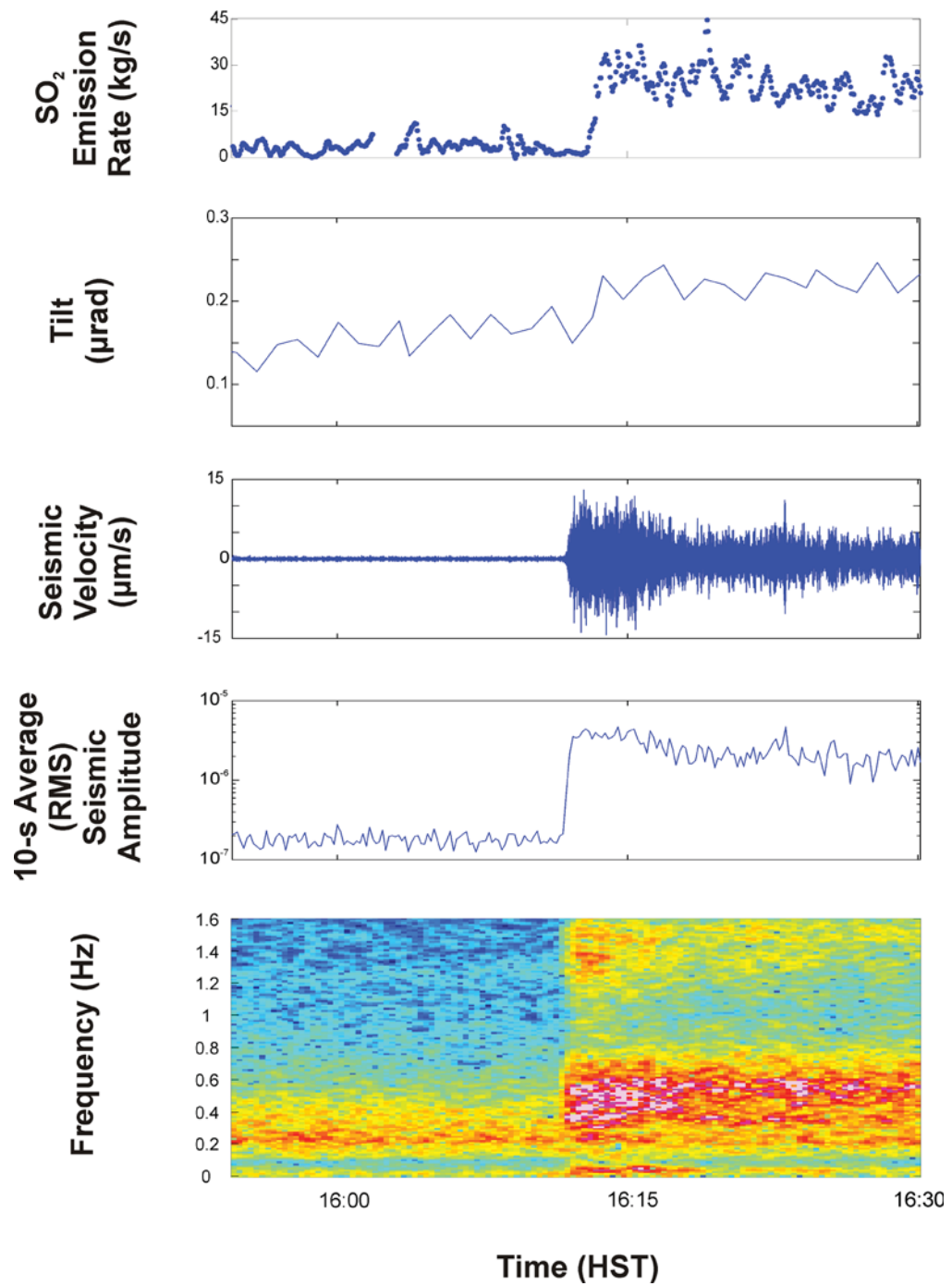


Figure 4.8: SO₂ emission rate, radial tilt, and seismicity for termination of second lava high stand, May 22, 2010

Chapter 4 – Kilauea Degassing and Summit Activity

Transform Infrared (FTIR) spectroscopy revealed H₂O-dominated gas (~80-90 mol% H₂O) during both passive background degassing and mild bubbling and spattering in the lava, consistent with open- or partially open-system degassing at shallow (<~200 m) depths. Lava lake rise within the column was marked by a decrease in SO₂, as seen in high stand events, and was attributed to the thinning of the magma above the slug as it flowed downwards around the rising slug. The limited and decreasing supply of shallowly degassed melt accounted for the measured decrease in SO₂ release. This explanation appears consistent with our observed decreased in SO₂ emission upon initiation of lava column rise. The large release of gas at the termination of gas piston activity was considerably more CO₂-rich (~70 mol% CO₂) than gas associated with passive degassing or spattering, with a markedly low SO₂/H₂S ratio. Both of these factors indicate gas that has equilibrated with magma at depths of over 600 m, suggesting a gas piston origin linked to the rise of deep gas.

Two significant factors lead to our eliminating slug rise as the underlying cause of high stand events in the summit vent in 2010. While FTIR data are not available for the high stands in May, subsequent events were measured via FTIR and neither gas compositions associated with high stand and nor draining degassing exhibit significant departures from background degassing compositions, and a spike in CO₂-rich gas as observed by *Edmonds and Gerlach* [2007] is absent [*Patrick et al.*, 2010; A.J. Sutton, pers. comm., 2010]. The H₂O-rich compositions reported to persist throughout the stages of high stand events indicates a shallow gas source inconsistent with the rise of a deep slug.

James et al. [2008] performed both laboratory experiments and numerical modeling to investigate slug expansion during ascent. For low-viscosity magmas, it was found that while the slug base velocity remained constant during ascent, decompression of slugs led to expansion of the gas that accelerated the slug nose upwards through the magma column. The greatest surface rise velocities are associated with the final stages of slug rise prior to bursting, in contrast to lava high stands, which display rapid onsets of lava rise followed by slowing rise and eventual stagnation for minutes or hours prior to the violent gas release [*Orr and Patrick*, 2009; *Patrick et al.*, 2010].

Chapter 4 – Kilauea Degassing and Summit Activity

Given the lack of CO₂ enrichment in gas expelled upon lava draining and lava surface rise rates inconsistent with those of slug rise and expansion, we can rule out slug rise as the mechanism behind the lava high stands of May 2010.

4.5.1.2 Gas accumulation

Swanson et al. [1979] ascribe the gas pistoning observed during the first phase of the 1969 – 1971 Mauna Ulu eruption of Kilauea to the trapping of gases beneath a relatively impermeable surface crust. They support their assertion with evidence of lava draining being both naturally and artificially triggered by penetration of the surface crust by various objects (e.g., rocks, jugs of water or gasoline), causing subsequent violent degassing. Some high stands occurring during the current summit eruption have also been noted to terminate upon the collapse of portions of the crater wall, which also serve to break the crust on the lava lake and induce the fall back to base lava level [Orr *et al.*, 2010; Patrick *et al.*, 2010].

To evaluate the plausibility of a physical barrier trapping bubbles as the mechanism for the high stands in May 2010, we examine the SO₂ time series measured by the UV camera. If gas is exsolving from the melt in the conduit at a constant rate, regardless of the presence or absence of a trapping crust, net emissions of SO₂ should also be constant over time if the assumption is made that there is no lateral gas loss via the conduit walls and that gas supply from depth is constant as well. Thus the departure of the gas emissions from baseline during a high stand should be compensated by the eventual release (and measurement by the UV camera) of the trapped gas beneath the surface crust. The mean SO₂ emission rate prior to the first lava high stands of May 22 is 13.67 kg/s. If we assume that to be the baseline of SO₂ emission rates at Kilauea's summit, the total emitted SO₂ over the duration of the first high stand (1:54:23; minimum duration, as high stand onset was during a pause for UV camera calibration) should be ~94 tonnes SO₂. With a mean emission rate of only ~3 kg/s SO₂, the high stand emitted only ~21 tonnes SO₂, leaving a deficit of over 70 tonnes of SO₂ for the first high stand. 57 tonnes of SO₂ are released in the emissions spike associated with the lava draining back to base level. That mass cannot account for the preceding high stand's deficit; accounting for the 31 tonnes expected to be emitted over the

Chapter 4 – Kilauea Degassing and Summit Activity

duration of the spike were emissions at baseline, the surplus is only 26 tonnes, which leaves the deficit owing to the first high stand at 47 tonnes. However, emission rates increase following the initial drop-off after the spike, with emissions higher than the pre-high stand baseline. If the full period of time following the first high stand and preceding the second high stand is taken into account, 123 tonnes of SO₂ should be emitted assuming the base level emission rate of 13.67 kg/s. Actual emissions over the inter-high stand period are 199 tonnes, accounting almost exactly for the 73 tonne deficit of the first high stand. The second high stand of the time series has a mean of 4.34 kg/s, and would account for 68 tonnes of SO₂ if the emission rate was at base level. Only 21 tonnes are emitted, leaving a deficit of 47 tonnes for the second high stand. The primary spike following the second stand involves the emission of another 53 tonnes of SO₂, a surplus of only 16 tonnes over the expected background emission of 37 tonnes. Another 31 tonnes are necessary to balance the SO₂ budget of the second high stand. SO₂ emission rate does begin to increase again after the spike; the UV camera dataset ends shortly after as a result of low light levels, meaning the total SO₂ emission between the second and third high stands cannot be precisely calculated. However, the mean emission rate following the second high stand's terminal spike in SO₂ is 16.17 kg/s, still elevated above base level degassing. If that rate of degassing persisted until the onset of the third high stand (based on seismicity and web camera imagery), 22 tonnes of SO₂ in excess of baseline degassing would be emitted prior to the third high stand, leaving a bulk deficit of only 9 tonnes of SO₂ for the second high stand. If SO₂ emission rate increased even minimally following the end of the UV camera time series (which would be the case if it mimicked the pattern of SO₂ emission following the first high stand), the 9 tonnes could easily be made up prior to the onset of the third high stand

While the two high stands measured on May 22, 2010 with the UV camera are a small subset of all high stand activity, based on our observations of these high stands, it appears that observations are not completely consistent with a gas accumulation model, though they do appear to fit such a model better than they do a slug model. Instead of all expected trapped gas being released, SO₂ deficits brought about by high stands are not immediately balanced by the release of gas upon lava draining. If high stands are simply a

result of all exsolved gas accumulating beneath a relatively impermeable crust, the full deficit of gas would be expected to be released upon disturbance of the crust and the return of the lava lake to its base level within the vent. While this is clearly not the case with post-high stand spikes in emission rate, the SO₂ budget is later balanced by continued surplus degassing until the onset of the subsequent high stand (Figure 4.9). It may be that the impermeable crust is causing suppression of gas exsolution such that the expected amount of gas is not accumulating as a free gas phase and only does so following removal of the capping viscous skin, or perhaps lava draining does not necessarily cause complete evacuation of the accumulated gas layer such that there is an extended release following the main spike in emissions.

4.5.1.3 Cyclic pressure variations

Witham et al. [2006] demonstrate periodic filling and draining of analogue lava lake models simply by the addition of gas fluxing upwards through the conduit into the lake. Decreased density in the conduit leads to a decreased hydrostatic head in the overlying lake, initiating lake rise. Eventually the increased lake depth increased pressure at the base of the lake such that the upward flux of the bubble-liquid mixture decreases. The system remains in precarious balance until a perturbation initiates net downward flow of lake liquid and the lake drains. Downward flow slows and the bubble-liquid mixture can begin to rise again, re-initiating lake filling. *Patrick et al.* [2010] point out the similarity of the pattern of lake heights in this model to that of the high stand, with faster rise at the onset of lake filling. However, they discount the model on the basis of expected gas emission patterns for such a mechanism. It is increased gas influx to the lake that results in lake rise, whereas high stands are associated with greatly diminished SO₂ emission rates. Likewise, where lake draining coincides with a spike in gas emissions at Kilauea, gas release is inhibited upon lake draining in the model.

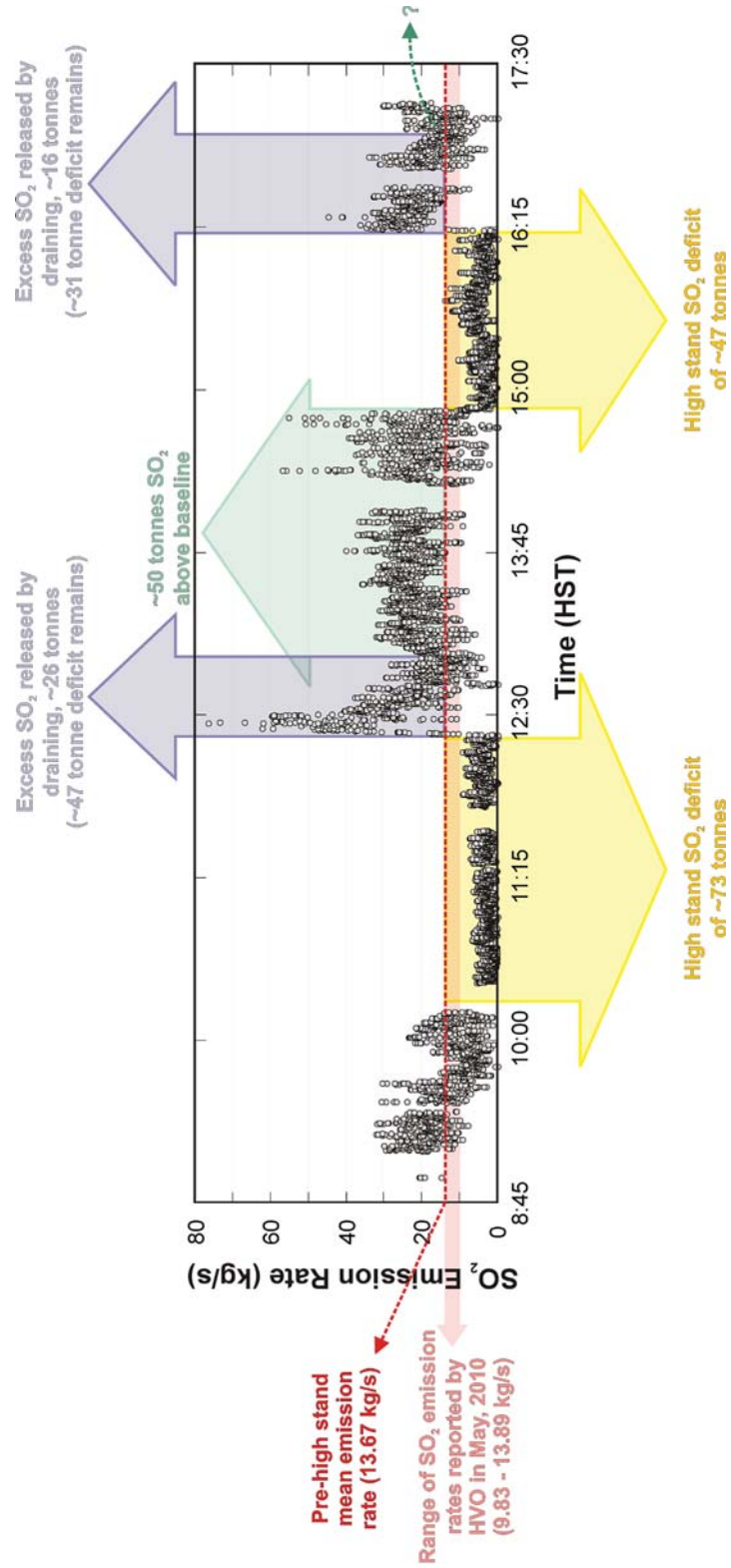


Figure 4.9: SO_2 budget for two lava high stands of May 22, 2010.

4.5.2 High stand mechanism

While deep slug rise is clearly the trigger for some cases of gas pistonning [e.g., *Edmonds and Gerlach*, 2007], such a model is not consistent with observations of lava rise rate and gas composition for high stands in the current summit vent of Halema`uma`u. At first glance, cyclic pressure variations do not appear to fit with the observed degassing scheme associated with high stand activity. However, the laboratory model of *Witham et al.* [2006] involved merely water and air. If a combined mechanism of cyclic pressure variations and a viscous, capping surface layer on a lava lake are envisioned, the increased gas fluxing through the lake would be masked due to accumulation beneath the lake surface. Upon draining, even if new degassing is suppressed, the previously trapped gas would be released, as seen in the high stand UV camera dataset. Thus periodic pressure fluctuations owing to gas fluxing into the lava lake may play a role, but would likely require the addition of a relatively impermeable lake surface layer to force accumulation of gas. Such a layer could also inhibit gas release and initiate lake level rise without the pressure variations at the base of the lake of the *Witham et al.* [2006] model.

In an effort to provide support for the plausibility of a gas accumulation model, we review examples of similar reported lava lake behaviors and associated interpretations. *Johnson et al.* [2005] provide evidence for the existence of viscous, capping layers on magma columns at Kilauea during ERZ eruptive activity. Thermal observations of gas piston sequences at Pu`u `O`o reveal decreased apparent temperatures of the magma column surface during rise within the vent, relative to background levels associated with quasi-continuous passive degassing. Temperature increased sharply upon release of the trapped gas and progressively returned to diminished levels upon the initiation of another rise event. The contrast in surface and underlying lava temperatures, in addition to sudden gas release led to the conclusion that gas was building up beneath a viscous cap, initiating lava level rise.

Further convincing evidence for gas accumulation as the cause of repeated variations in lava crust height is the work of *Patrick et al.* [2011a], also along the ERZ at Kilauea. In contrast to previous work on gas piston events in vents in the summit crater or Pu`u `O`o

cone, cycles of rise and fall of crusted lava in a perched lava channel on the active flow field were studied. Over the length of a 1.4 km long lava channel, lava level rose within the walls of the channel until it reached the height of the wall. Vigorous spattering along the margins of the channel ensued, followed by an abrupt drop in lava level. Given the shallow channel (~20 m) and distance from the source vent, deep slug rise was excluded as a source mechanism, leaving gas accumulation as the best explanation. Further cited evidence for a boundary layer trapping gas beneath it were instances of slabs of solidified lava crust foundering beneath other slabs, accompanied by bubbling and some gas release from the location of the downgoing slab. Similar behavior is noted in the summit vent of Kilauea, wherein increased spatter and bubbling is often noted on the side of the lake where cooled surface lava descends (HVO, <http://volcanoes.usgs.gov/hvo/activity/archive.php>).

Variability in the behavior of lava lake surface crust was also observed at Erta Ale volcano, Ethiopia [Harris *et al.*, 2005]. In this case, thermal features (e.g., spreading centers or cracks in on the lake surface) were tracked as they passed the temperature sensor's field of view over time during lake convection. Frequency analysis of the time series indicates variable periods of sluggish (cooler, fewer thermal anomalies and slower motion, 1 – 10 hr duration) and vigorous (warmer, rapid horizontal surface motion, 1 – 3 hr duration) convection. The variations in convective regime are interpreted to represent either surface manifestation of variable supply of gas-rich, buoyant magma at depth (which would trigger the onset of vigorous convection) or convective overturn triggered by the instability of an increasingly dense, cooled surface layer, under which gas could accumulate. Small lava fountains also occur at Erta Ale where lake crust is consumed upon foundering [Harris *et al.*, 2005], much like the bubbling along sinking slabs in the perched channel of Patrick *et al.* [2011a]. While Harris *et al.* [2005] do not mention short-term lake level fluctuations associated with the variations in lake surface velocity akin to those during high stands at Kilauea, Oppenheimer *et al.* [2004] report emission rates of only 0.7 kg/s of SO₂ from the lake. At just ~5% the baseline SO₂ emission rate for Kilauea on May 22, the supply of SO₂ at Erta Ale may not be sufficient to accumulate enough gas beneath the cooled crust of the sluggish regime to buoy the lake level upwards despite underlying gas accumulation.

Chapter 4 – Kilauea Degassing and Summit Activity

If, on the basis of our observations at Kilauea and supporting evidence from the above mentioned studies, we accept gas accumulation as the mechanism causing lava high stands (with the possibility of pressure fluctuations leading to the cyclic nature of some event sequences), we must next attempt to explain the trigger and termination mechanisms. Termination of high stands can be relatively straightforwardly explained. Release of the trapped gas could be brought about by: puncture of the capping layer by a portion of the crater wall (or other object) providing the initial impetus for disruption of the crust and release of the accumulated gas [e.g., *Orr and Patrick, 2009; Orr et al., 2010; Patrick et al., 2010; Swanson et al., 1979*]; the density of the cooled capping surface increasing to the point that the gas layer can no longer support it, inducing sudden convective overturn and release of accumulated gas [*Harris et al., 2005*]; or a pressure disturbance at the base of the lava lake [e.g., *Witham et al., 2006*] inducing lake drainage, with destruction of the surface crust occurring as a consequence of the draining. Still, questions remain with regard to the initial trigger mechanism for the event (or first in a series of events), the cause of the stagnation of the lake level following initial rise, and the fact that the SO₂ budget deficit is not accounted for in the immediate release of gas following lake draining, but is over the prolonged period leading up to the subsequent high stand.

As for a trigger mechanism, though *Orr et al. [2010]* confirm that high stand termination may be brought about by rockfalls impacting the high lava surface, they also state that lava lake rise can be spurred by debris impacting the lake. Experimental work by *Sumner et al. [2007]* demonstrates that vesiculation can be induced in samples of heated rhyolite simply by sudden impact with another object (e.g., airgun pellet, metal cylinder). They apply their results to volcanic bombs, asserting that some vesicles in bombs may be the result of the bomb's impact on the ground surface. It may be that forces associated with rockfall impacts on lava in the vent at Kilauea can, in certain circumstances induce a similar sudden vesiculation that leads to bubble accumulation and lake surface rise.

Conduit convection driven by density contrasts between upwelling gas-rich and descending degassed magma is an accepted explanation for maintenance of persistently

degassing volcanic systems [e.g., *Kazahaya et al.*, 1994; *Palma et al.*, 2011; *Shinohara*, 2008; *Stevenson and Blake*, 1998]. Constant lake surface motion in Kilauea's summit lava lake is a likely manifestation of this process operating in the shallow conduit. Slowing of lake surface velocity can be inferred as a slowing of convection, which occurs over times scales of a few tens of minutes at the onset of lava high stands. While partial collapse of the upper crater rim has been noted to cause rockfalls that trigger high stands, if portions of the submerged lake walls or viscous remnants of previous surface crust descend in the magma column and partially block the outlet for degassed magma at the base of the lava lake, net magma flux into the lake could temporarily increase, causing lake rise. Lack of outflow to counter the influx would then slow convection, leading to decreased lake surface velocity; increased residence time at the lake surface and therefore surface cooling and thickening; and gas accumulation beneath the lake crust.

4.5.3 Geophysical implications

First order examination of time series of SO₂ emission rate and seismicity indicate that there is an undeniable link between the two. Decreases in both gas emission and tremor are coincident with the onset of lava level rise within the summit vent. Examination of the spectral content of background, high stand, and lava draining seismicity indicates the essential disappearance of all predominant bands of seismicity, except for the 0.04 and 0.22 Hz bands. While the 0.04 Hz band weakens during high stands, the strength of the 0.22 Hz band does not change, as revealed by a water-level deconvolution [*Helmberger and Wiggins*, 1971] of representative spectra from background and high stand tremor. Given that amplitude of the 0.22 Hz band appears unaffected by high stands or other volcanic activity, we infer that this represents the oceanic microseism, or background seismic noise related to water waves on the ocean. Thus volcanic tremor at the summit of Kilauea is mostly stifled upon the rise of lava in the conduit.

Chouet et al. [2010] observe nearly the same dominant frequencies when evaluating seismic response to summit vent degassing bursts in the VLP band, and *Patrick et al.* [2011b] refer to the same degassing burst signals as well as peak episodic tremor at ~0.5 Hz. VLP

events are attributed to either the conduit response of a source at ~ 1 km depth to slug rise and burst [Chouet *et al.*, 2010], which we have already discounted for the high stand events considered here, or the coupling of degassing-induced vibrations at the top of the conduit to the same source at depth [Patrick *et al.*, 2011b]. In the case of Patrick *et al.* [2011b], it is of note that both small episodic tremor and larger VLPs resulting from degassing bursts have similar spectral characteristics and are both attributed to conduit response to varying degrees of gas release from the surface of the lava column. Given comparable dominant frequencies in all three stages of high stand seismicity (background, high stand, and draining), and the similarity (excluding duration) of high stand events to the gas pistoning driving episodic tremor, we may infer a continuum of gas release styles from the lava lake surface, which induces the same conduit response, but to varying degrees. Aside from the irrelevant oceanic microseism, the 0.04 Hz tremor is the only band noted in all activity considered (degassing bursts, episodic tremor, and the three stages of high stands). It is, however, significantly weakened during lava high stands, coincident with diminished SO_2 emission rates. If it is surficial degassing activity that is the source of the 0.04 Hz and other seismic spectral peaks, we must consider that higher frequency peaks at 0.36 and 0.55 Hz vanish during high stands. These peaks have been attributed to higher modes of resonance above the ‘breathing mode’ of the summit vent system at 0.04 Hz [Chouet *et al.*, 2010; Dawson *et al.*, 2010]. At the extremely low SO_2 emission rates associated with high stand activity, degassing may not be vigorous enough (as indicated by the weakened 0.04 Hz tremor) to excite the higher modes of resonance, which would explain their absence from the high stand spectrum. The sudden, violent gas release at the termination of high stands is associated with a resurgence of all dominant spectral peaks, supporting the concept of direct correlation of surface degassing and the VLP seismicity. Ideally, correlation between SO_2 emission rate and seismic amplitude in the 0.04 Hz band would verify this relationship. Unlike at other volcanoes where emission rate measurement in UV imagery may take place immediately adjacent to the vent (e.g., Fuego, Guatemala) and small variations in emission rate can be shown to correlate with low frequency seismicity [Nadeau *et al.*, 2011], at Kilauea, volcano topography may preclude such correlations. In order to account for as much of the plume cross-section as

Chapter 4 – Kilauea Degassing and Summit Activity

possible, plume profiles are ~ 1 km downwind of the vent, such that mixing and advection of ambient air may blur small signals correlating to minor increases in 0.04 Hz seismicity. Even if profiles could be sampled closer to the vent (as with a plume rising straight up), such mixing may still occur in the vent itself between the lake surface and appearance above the caldera rim in imagery.

Even lacking direct correlation on small scales between degassing and 0.04 Hz tremor, studies at other volcanoes have proposed that degassing at the surface of a lava lake or column can be the source of volcanic tremor [Metaxian *et al.*, 1997; Palma *et al.*, 2008; Ripepe *et al.*, 2001]. Similarities in tremor at Pu'u 'O'o to gas pistonning events lead to the assertion that they are different manifestations of the same degassing [Ferrazzini *et al.*, 1991]. At Erta Ale, seismic spectral content and tremor location vary during sluggish versus vigorous convective regimes [Jones *et al.*, 2006]. The slow convection scheme is characterized by the absence of high frequency seismicity, and tremor location and polarization analysis indicate a source ~ 150 m ENE of the lake, and 310 – 360 m below the surface of the lake. Vigorous convection is typified by broadband seismicity, with the same low frequency characteristics of the sluggish regime tremor but with the addition of higher frequency energy as well. Source locations for tremor during vigorous tremor cluster further south (E of the lake), with some scatter in the direction of the lower frequency tremor source. Jones *et al.* [2006] interpret this to be a manifestation of crustal cooling and viscosity increase at the surface of the lake during sluggish convection; gas buildup and coalescence under the crust generates low-frequency tremor, while cracking crust, gas escape, fountaining, and foundering of crust during vigorous convection generate higher frequencies. The higher frequency seismicity associated with the vigorous lake overturn may be analogous to the emergence of small peaks at ~ 1.3 and ~ 1.5 Hz during lake draining following high stands at Kilauea.

4.6 Conclusions

Transient events marked by the rise and fall of the surface of the lava lake, or lava high stands, in Kilauea's summit vent occurred sporadically in May, 2010. Upon initiation of lava rise, SO₂ emission rates (as measured via UV camera) drop precipitously relative to background levels. Seismic tremor amplitude in all characteristic bands decreases by an order of magnitude. Infrasound energy decreases as well, as does surface velocity of the lava lake. High stand onset is also accompanied by a small summit deflation. Once the lava has risen ~20 m in ~0.5 hours, lake level plateaus and can remain constant for ~2 or more hours. Lava lake drainage may then occur spontaneously or be triggered by the impact of rockfalls onto the lava surface. Bubbling and degassing at the surface lake increase and lava drains back to base level as seismicity and SO₂ emission rate spike well above background before stabilizing at levels near to those prior to the high stand.

Observations generally favor an explanation invoking the accumulation of exsolved gas beneath a viscous capping layer as the mechanism for triggering lake level rise. A budget of SO₂ emitted over the course of two high stand events indicate that the deficit created by the emission rate decrease below background degassing is not recovered by the initial spike in SO₂, as would be assumed by simple gas accumulation over time. However, mildly elevated emission rates that persist to the onset of the subsequent high stand do later reconcile the SO₂ budget and account for the remainder of the deficit. Accordingly, an addendum to the gas accumulation mechanism is that gas exsolution is either suppressed temporarily until following lake draining, or that initial lake draining is not efficiently evacuating the whole of the accumulated gas later in a single bulk gas emission.

With this study, we have drawn comparisons of high stands to similar activity at Kilauea and other volcanoes, with the benefit of measurements of gas emission rate. We can therefore assert that observed degassing styles in the summit eruption of Kilauea and associated seismicity are a continuum of the same process, with surface degassing exciting seismicity. At one end of the spectrum are lava high stands, wherein a viscous boundary layer prevents the bulk of exsolved bubbles from freely degassing at the lava surface.

Background degassing and tremor represent the next step in the progression, with moderate amounts of degassing occurring from the conduit lava. Episodic tremor [Patrick *et al.*, 2011b] and draining lava high stands appear to be similar events; seismic velocities associated with each are roughly equivalent. Large degassing bursts, like those described by Patrick *et al.* [2011b] and Chouet *et al.* [2010] are a more violent end-member, and are marked by even larger VLP amplitudes.

Further constraints on models of high stand and other behavior could be made with additional measurements of SO₂ emission rate. Limiting factors like weather restricted the sample size examined in this study to only two consecutive high stand events; a larger sample size would provide more information on the general behavior of gas emissions during varied types of high stand events. Nevertheless, the high temporal resolution of the UV camera data offers insight into the mechanisms at work during high stand events at Kilauea.

4.7 Acknowledgements

Funding for field work in Hawaii was provided by a Grant-In-Aid of Research from Sigma Xi, The Scientific Research Society; a graduate fellowship from the Michigan Space Grant Consortium; and a DeVlieg Fellowship from Michigan Technological University. Manuscript completion was also supported by NSF PIRE 0530109. We thank the National Park Service, Hawaii Volcanoes National Park, the United States Geological Survey, and the Hawaiian Volcano Observatory for accommodating and facilitating field work at Kilauea. E. Head and C. Sealing are thanked for assistance in the field, and D. Wilson, M. Poland, K. Wooten, M. Patrick, D. Fee, M. Garces, C. Kern, and W. Thelen are also thanked for data sharing and valuable discussions.

4.8 References

Barker, S. R., D. R. Sherrod, M. Lisowski, C. Heliker, and J. S. Nakata (2003), Correlation between lava-pond drainback, seismicity, and ground deformation at Pu`u`O`o, in The Pu`u`O`o-Kupaianaha Eruption of Kilauea Volcano, Hawaii: The First 20 Years, U.S. Geological Survey Professional Paper 1676, pp. 53-62.

Chapter 4 – Kilauea Degassing and Summit Activity

- Chouet, B., and H. R. Shaw (1991), Fractal properties of tremor and gas piston events observed at Kilauea Volcano, Hawaii, *Journal of Geophysical Research-Solid Earth and Planets*, 96(B6), 10177-10189.
- Chouet, B. A., P. B. Dawson, M. R. James, and S. J. Lane (2010), Seismic source mechanism of degassing bursts at Kilauea Volcano, Hawaii: Results from waveform inversion in the 10-50 s band, *Journal of Geophysical Research*, 115(B9), B09311.
- Dawson, P. B., M. C. Benítez, B. A. Chouet, D. Wilson, and P. G. Okubo (2010), Monitoring very-long-period seismicity at Kilauea Volcano, Hawaii, *Geophysical Research Letters*, 37(18), L18306.
- Ferrazzini, V., K. Aki, and B. Chouet (1991), Characteristics of seismic waves composing Hawaiian volcanic tremor and gas-piston events observed by a near-source array, *Journal of Geophysical Research*, 96(B4), 6199-6209.
- Harris, A. J. L., R. Carniel, and J. Jones (2005), Identification of variable convective regimes at Erta Ale Lava Lake, *Journal of Volcanology and Geothermal Research*, 142(3-4), 207-223.
- Helmberger, D., and R. A. Wiggins (1971), Upper Mantle Structure of Midwestern United States, *Journal of Geophysical Research*, 76(14), 3229-3245.
- James, M. R., S. J. Lane, and S. B. Corder (2008), Modelling the rapid near-surface expansion of gas slugs in low-viscosity magmas, *Geological Society, London, Special Publications*, 307(1), 147-167.
- Johnson, J. B., A. J. L. Harris, and R. P. Hoblitt (2005), Thermal observations of gas pistonning at Kilauea Volcano, *Journal of Geophysical Research-Solid Earth*, 110, B11201.
- Jones, J., R. Carniel, A. J. L. Harris, and S. Malone (2006), Seismic characteristics of variable convection at Erta 'Ale lava lake, Ethiopia, *Journal of Volcanology and Geothermal Research*, 153(1-2), 64-79.
- Kazahaya, K., H. Shinohara, and G. Saito (1994), Excessive degassing of Izu-Oshima Volcano - Magma convection in a conduit, *Bulletin of Volcanology*, 56(3), 207-216.
- Metaxian, J. P., P. Lesage, and J. Dorel (1997), Permanent tremor of Masaya Volcano, Nicaragua: Wave field analysis and source location, *Journal of Geophysical Research-Solid Earth*, 102(B10), 22529-22545.
- Nadeau, P. A., J. L. Palma, and G. P. Waite (2011), Linking volcanic tremor, degassing, and eruption dynamics via SO₂ imaging, *Geophysical Research Letters*, 38(1), L01304.
- Oppenheimer, C., A. J. S. McGonigle, P. Allard, M. J. Wooster, and V. Tsanev (2004), Sulfur, heat, and magma budget of Erta 'Ale lava lake, Ethiopia, *Geology*, 32(6), 509-512.

Chapter 4 – Kilauea Degassing and Summit Activity

- Orr, T., and M. Patrick (2009), What has driven degassing events during the 2008-2009 summit eruption of Kilauea Volcano, Hawai'i?, *Eos Transactions American Geophysical Union*, 90(52), Fall Meeting Supplement, Abstract V43G-2330
- Orr, T., M. Patrick, D. Wilson, A. J. Sutton, and T. Elias (2010), The impact of rockfalls on shallow degassing processes during the 2008-2010 summit eruption of Kilauea Volcano, Hawai'i, Abstract V21C-2340 presented at 2010 Fall Meeting, American Geophysical Union, San Francisco, Calif., 13-17 Dec.
- Palma, J. L., E. S. Calder, D. Basualto, S. Blake, and D. A. Rothery (2008), Correlations between SO₂ flux, seismicity, and outgassing activity at the open vent of Villarrica volcano, Chile, *Journal of Geophysical Research-Solid Earth*, 113(B10), B10201.
- Palma, J. L., S. Blake, and E. S. Calder (2011), Constraints on the rates of degassing and convection in basaltic open-vent volcanoes, *Geochemistry Geophysics Geosystems*, 12(11), Q11006.
- Patrick, M., T. Orr, D. Wilson, A. J. Sutton, T. Elias, D. Fee, and P. A. Nadeau (2010), Evidence for gas accumulation beneath the surface crust driving cyclic rise and fall of the lava surface at Halema'uma'u, Kilauea Volcano, Abstract V21C-2339 presented at 2010 Fall Meeting, American Geophysical Union, San Francisco, Calif., 13-17 Dec.
- Patrick, M., T. Orr, D. Wilson, D. Dow, and R. Freeman (2011a), Cyclic spattering, seismic tremor, and surface fluctuation within a perched lava channel, Kilauea Volcano, *Bulletin of Volcanology*, 73(6), 639-653.
- Patrick, M. R., D. Wilson, D. Fee, T. Orr, and D. Swanson (2011b), Shallow degassing events as a trigger for very-long-period seismicity at Kilauea Volcano, Hawai'i, *Bulletin of Volcanology*, 1-8.
- Perret, F. A. (1913), The floating islands of Halemaumau, *American Journal of Science*, 35(207), 273-282.
- Poland, M. P., A. Miklius, P. Lundgren, and A. J. Sutton (2011), Repeated deflation-inflation events at Kilauea Volcano, Hawaii: What's up (and down) with that?, V51G-01 presented at 2011 Fall Meeting, American Geophysical Union, San Francisco, Calif., 5-9 Dec.
- Ripepe, M., M. Coltelli, E. Privitera, S. Gresta, M. Moretti, and D. Piccinini (2001), Seismic and infrasonic evidences for an impulsive source of the shallow volcanic tremor at Mt. Etna, Italy, *Geophysical Research Letters*, 28(6), 1071-1074.
- Shinohara, H. (2008), Excess degassing from volcanoes and its role on eruptive and intrusive activity, *Reviews of Geophysics*, 46(4), RG4005.
- Stevenson, D. S., and S. Blake (1998), Modelling the dynamics and thermodynamics of volcanic degassing, *Bulletin of Volcanology*, 60(4), 307-317.

Chapter 4 – Kilauea Degassing and Summit Activity

- Sumner, J. M., D. A. Rothery, O. Spieler, and D. B. Dingwell (2007), Impact vesiculation - a new trigger for volcanic bubble growth and degassing, *eEarth*, 2(4), 151-167.
- Swanson, D. A., W. A. Duffield, D. B. Jackson, and D. W. Peterson (1979), Chronological narrative of the 1969-1971 Mauna Ulu eruption of Kilauea volcano, Hawaii, in, U.S. Geological Survey Professional Paper 1056, p. 55.
- Wilson, D., T. Elias, T. Orr, M. Patrick, J. Sutton, and D. Swanson (2008), Small Explosion From New Vent at Kilauea's Summit, *Eos Transactions American Geophysical Union*, 89(22), 203.
- Witham, F., A. Woods, and C. Gladstone (2006), An analogue experimental model of depth fluctuations in lava lakes, *Bulletin of Volcanology*, 69(1), 51-56.

Chapter 5: CONCLUSIONS

5.1 Summary of results

Work presented in this dissertation has demonstrated the usefulness of new UV camera technology in studying the role of gas in various styles of volcanic activity. One of the main shortcomings of previous means of measuring SO₂ emission rates was the disparity in temporal resolution between SO₂ and seismic or other geophysical data even though many models of volcanic activity depend, in part, on behavior of volatiles [Chouet, 1996; Ripepe and Gordeev, 1999]. Below are important highlights of this work as they pertain to application of UV camera-derived emission rates to better understanding volcanic processes.

- 1) Both emission rates of SO₂ and plume speed can be extracted semi-automatically from time series of UV camera images. A user-friendly, open source Matlab program facilitates image processing, and results agree with previously established methods for such measurements.
- 2) High-temporal SO₂ emission rates obtained via the UV camera and low-frequency tremor behaved in similar manners at Fuego volcano, Guatemala, in 2009, indicating linked source processes.
- 3) Long-term decreases in SO₂ emission rate prior to ashy explosions at Fuego in 2009 indicate rheological stiffening and impedance of gas escape within the upper conduit, leading to pressurization and subsequent explosion.
- 4) The synoptic spatial view of UV camera imagery can allow for the identification of multiple gas sources in singles images, which may in turn aid in interpretation of degassing and eruption processes.

- 5) A transient phenomenon of prolonged lava high stand in the summit vent of Kilauea is characterized by decreased emission rates of SO_2 and also diminished seismicity. Masses of SO_2 released following lava draining indicate gas accumulation beneath a viscous capping layer is the likely cause of such events.
- 6) The direct link between decreased tremor and an inhibition of surface degassing at Kilauea point towards shallow degassing at the surface of the magma column as the main source of seismicity in the summit eruption.
- 7) Very long-period seismic events at Fuego volcano in 2008 are immediately followed by increases in SO_2 emission rate that correlate roughly with the amplitude of the VLP. Pressurization at depth may be the source of the VLPs, as larger events result in an expedited arrival of SO_2 at the surface.

5.2 Limitations of the UV camera

Dalton et al. [2009] and *Kern et al.* [2010b] evaluate the accuracy of various means of processing UV imagery and errors associated with the method; summarized below are additional scientific and logistical issues encountered over the course of this dissertation. Solutions do not necessarily exist, but awareness of potential problems is important.

CCD sensors in the camera are two-dimensional; by utilizing both dimensions for spatial information rather than one for spatial and one for spectral, spectral information is limited to the integration of an external bandpass filter(s). Without information in multiple portions of the UV spectrum, any measured absorbance cannot be attributed to SO_2 alone. The addition of a second filter aids in isolation of SO_2 , but requires a second, synchronized camera, especially in cases of quickly evolving plumes. For very slow-moving plumes, a filter wheel with multiple filters on a single camera may be useful [e.g., *Prata*, 2011], but will still limit the user to a minimal number of filters, as plume evolution between images with greater numbers of filters would be prohibitive in terms of image alignment and plume age.

Chapter 5 – Conclusions

Sufficient power for camera and computer operation may be an issue, depending on volcano accessibility. The Apogee systems referred to throughout this dissertation require deep cooling of the CCD array and are thus a significant power drain. This is not a problem if buildings, such as volcano observatories, with power are nearby to simply plug in the system. More remote field sites, but with accommodations in the area, are slightly more problematic in that external power sources (e.g., car batteries) are required, but recharging or replacement can still easily occur between field sessions. Very isolated volcanoes pose the most significant problem, as arrangements must be made for sufficient power supplies to be transported to the field site.

Interference by ash in plumes is problematic at explosive volcanoes (e.g., Fuego; Chapter 3). Attenuation of UV skylight by the dark particulate matter is indistinguishable from attenuation of UV by absorption by SO_2 in UV imagery. Thus measurement of emission rates is limited to passive, inter-explosion degassing at volcanoes emitting ashy plumes and explosive degassing associated with ash emissions cannot be quantified with methods used here. Integration of DOAS-based spectrometers into UV camera systems may allow for an ash correction and thus quantification of explosive SO_2 in ashy plumes [Holland *et al.*, 2011; Kern *et al.*, 2010a; Kern *et al.*, 2010b]. Meteorological clouds pose a similar problem; clouds between the camera and the SO_2 plume may be thick enough to attenuate the incoming UV signal, thereby appearing to be increased SO_2 , or they may reflect excess UV toward the camera, appearing overly bright and negating any absorption signal of SO_2 in the plume behind them.

Apparent at Kilauea and Masaya were the limitations relating to plume propagation and volcano topography. While Fuego is a stratovolcano with a plume that lofted off the edifice, shield volcanoes with low-lying undulating topography can be problematic. Not only is the selection of a satisfactory viewing location for observation of the summit difficult, but with little relief over the surrounding topography, plumes are often grounded, which can lead to underestimation of SO_2 emission rates. Viewing location selection can also prove

difficult for volcanoes like Fuego, where accessibility is limited in certain sectors of the area. Observations at Fuego were limited to the north side of the edifice; had the plume had an orientation toward the south of the volcano, measurements would have been impossible.

Finally, weather is always a limiting factor in field work, but given the need for bright background sky and a clear line of sight to the plume, days yielding useable data may be limited over the course of a field campaign. High winds that cause camera shake are another factor that is detrimental to quality data collection, resulting in blurred imagery.

5.3 Future recommendations

Since the advent of the UV camera only a few years ago, it has already become possible to detect linkages between geophysical phenomena and degassing. Chapters 3 and 4 are two examples, but concurrent UV camera and seismic data at Asama volcano, Japan, also indicate a linkage between very-long-period seismic pulses and eruptive SO_2 emissions [Kazahaya *et al.*, 2011]. UV camera data have also made it possible to distinguish styles of degassing and their relationships to eruption mechanisms. At Pacaya volcano, Guatemala, a discrepancy between SO_2 emissions as calculated from infrasound records of Strombolian bubble bursts and those from the UV camera indicated that a significant portion of degassing was a result of a process other than bubble bursts [Dalton *et al.*, 2010]. Via viscosity modeling and analysis of patterns in UV camera data, Holland *et al.* [2011] showed that explosions at Santiaguito volcano, Guatemala, are a result of shear fracturing rather than vent pressurization. Tamburello *et al.* [2011] used a UV camera in tandem with a multi-gas sensor at the La Fossa fumarole field at Vulcano, Italy and were able to calculate distinct SO_2 emission rate time-series from four fumarolic areas. Multiplication of the SO_2 emission rates by gas molar ratios from the multi-gas sensor yielded emission rates of H_2O , H_2S , and CO_2 .

In terms of technical recommendations, power limitations could be mitigated by the incorporation of other, smaller cameras or CCD systems into the UV camera platform. Incorporation of a DOAS system into the UV camera package would reduce calibration

error in camera data by adding spectral information [Kern *et al.*, 2010b]. Finally, image processing algorithms could likely be refined, as with the incorporation of optical flow methodology to identify variability in plume speed.

Undoubtedly most important, UV cameras simply need to be used more often. With limited usage, results are already impressive; deployment to other volcanic systems will surely yield further insight into the processes at work in volcanic systems.

5.4 References

- Chouet, B. A. (1996), New methods and future trends in seismological volcano monitoring, in *Monitoring and Mitigation of Volcano Hazards*, edited by R. Scarpa and R. Tilling, pp. 23-98, Springer-Verlag, Berlin.
- Dalton, M. P., I. M. Watson, P. A. Nadeau, C. Werner, W. Morrow, and J. M. Shannon (2009), Assessment of the UV camera sulfur dioxide retrieval for point source plumes, *Journal of Volcanology and Geothermal Research*, 188(4), 358-366.
- Dalton, M. P., G. P. Waite, I. M. Watson, and P. A. Nadeau (2010), Multiparameter quantification of gas release during weak Strombolian eruptions at Pacaya Volcano, Guatemala, *Geophysical Research Letters*, 37(9), L09303.
- Holland, A. S. P., I. M. Watson, J. C. Phillips, L. Caricchi, and M. P. Dalton (2011), Degassing processes during lava dome growth: Insights from Santiaguito lava dome, Guatemala, *Journal of Volcanology and Geothermal Research*, 202(1-2), 153-166.
- Kazahaya, R., T. Mori, M. Takeo, T. Ohminato, T. Urabe, and Y. Maeda (2011), Relation between single very-long-period pulses and volcanic gas emissions at Mt. Asama, Japan, *Geophysical Research Letters*, 38(11), L11307.
- Kern, C., T. Deutschmann, L. Vogel, M. Wöhrbach, T. Wagner, and U. Platt (2010a), Radiative transfer corrections for accurate spectroscopic measurements of volcanic gas emissions, *Bulletin of Volcanology*, 72(2), 233-247.
- Kern, C., F. Kick, P. Lübcke, L. Vogel, M. Wöhrbach, and U. Platt (2010b), Theoretical description of functionality, applications, and limitations of SO₂ cameras for the remote sensing of volcanic plumes, *Atmospheric Measurement Techniques*, 3(3), 733-749.
- Prata, A. J. (2011), UV Ground-based imaging camera: EnviCam, presented at Open Vent Volcanoes PASI Workshop, San Jose, Costa Rica, 15 January 2011.
- Ripepe, M., and E. Gordeev (1999), Gas bubble dynamics model for shallow volcanic tremor at Stromboli, *Journal of Geophysical Research-Solid Earth*, 104(B5), 10639-10654.

Chapter 5 – Conclusions

Tamburello, G., E. P. Kantzas, A. J. S. McGonigle, A. Aiuppa, and G. Giudice (2011), UV camera measurements of fumarole field degassing (La Fossa crater, Vulcano Island), *Journal of Volcanology and Geothermal Research*, 199(1-2), 47-52.

COMPLETE REFERENCE LIST

- Almendros, J., B. Chouet, and P. Dawson (2001), Spatial extent of a hydrothermal system at Kilauea Volcano, Hawaii, determined from array analyses of shallow long-period seismicity - 1. Method, *Journal of Geophysical Research-Solid Earth*, 106(B7), 13565-13580.
- Andres, R. J., W. I. Rose, R. E. Stoiber, S. N. Williams, O. Matías, and R. Morales (1993), A summary of sulfur dioxide emission rate measurements from Guatemalan volcanoes, *Bull. Volcanol.*, 55(5), 379-388.
- Aster, R., S. Mah, P. Kyle, W. McIntosh, N. Dunbar, J. B. Johnson, M. Ruiz, and S. McNamara (2003), Very long period oscillations of Mount Erebus Volcano, *J. Geophys. Res.*, 108(B11), 2522.
- Barker, S. R., D. R. Sherrod, M. Lisowski, C. Heliker, and J. S. Nakata (2003), Correlation between lava-pond drainback, seismicity, and ground deformation at Pu`u`O`o, in The Pu`u`O`o-Kupaianaha Eruption of Kilauea Volcano, Hawaii: The First 20 Years, U.S. Geological Survey Professional Paper 1676, pp. 53-62.
- Battaglia, J., J.-L. Got, and P. Okubo (2003), Location of long-period events below Kilauea Volcano using seismic amplitudes and accurate relative relocation, *Journal of Geophysical Research*, 108(B12), 2553.
- Berlo, K., J. Stix, K. Roggensack, and B. Ghaleb (2011), A tale of two magmas, Fuego, Guatemala, *Bulletin of Volcanology*, 1-14.
- Bluth, G. J. S., J. M. Shannon, I. M. Watson, A. J. Prata, and V. J. Realmuto (2007), Development of an ultra-violet digital camera for volcanic SO₂ imaging, *Journal of Volcanology and Geothermal Research*, 161(1-2), 47-56.
- Bobrowski, N., G. Hönninger, F. Lohberger, and U. Platt (2006), IDOAS: A new monitoring technique to study the 2D distribution of volcanic gas emissions, *Journal of Volcanology and Geothermal Research*, 150(4), 329-338.
- Boichu, M., C. Oppenheimer, V. Tsanev, and P. R. Kyle (2010), High temporal resolution SO₂ flux measurements at Erebus volcano, Antarctica, *Journal of Volcanology and Geothermal Research*, 190(3-4), 325-336.

References

- Burton, M. R., C. Oppenheimer, L. A. Horrocks, and P. W. Francis (2000), Remote sensing of CO₂ and H₂O emission rates from Masaya volcano, Nicaragua, *Geology*, 28(10), 915-918.
- Canny, J. (1986), A Computational Approach to Edge Detection, *Pattern Analysis and Machine Intelligence, IEEE Transactions on, PAMI-8*(6), 679-698.
- Carn, S. A., A. J. Krueger, S. Arellano, N. A. Krotkov, and K. Yang (2008), Daily monitoring of Ecuadorian volcanic degassing from space, *Journal of Volcanology and Geothermal Research*, 176(1), 141-150.
- Carr, M. J., M. D. Feigenson, L. C. Patino, and J. A. Walker (2003), Volcanism and geochemistry in Central America: Progress and problems, in *Inside the Subduction Factory*, edited by J. Eiler, pp. 153-174, AGU, Washington, D.C.
- Chesner, C. A., and W. I. Rose (1984), Geochemistry and evolution of the fuego volcanic complex, Guatemala, *Journal of Volcanology and Geothermal Research*, 21(1-2), 25-44.
- Chouet, B., and H. R. Shaw (1991), Fractal properties of tremor and gas piston events observed at Kilauea Volcano, Hawaii, *Journal of Geophysical Research-Solid Earth and Planets*, 96(B6), 10177-10189.
- Chouet, B. A. (1992), A seismic model for the source of long-period events and harmonic tremor, in *Volcanic Seismology*, edited by P. Gasparini, R. Scarpa and K. Aki, pp. 133-156, Springer, New York.
- Chouet, B. A. (1996), New methods and future trends in seismological volcano monitoring, in *Monitoring and Mitigation of Volcano Hazards*, edited by R. Scarpa and R. Tilling, pp. 23-98, Springer-Verlag, Berlin.
- Chouet, B. A., P. Dawson, and A. Arciniega-Ceballos (2005), Source mechanism of Vulcanian degassing at Popocatepetl Volcano, Mexico, determined from waveform inversions of very long period signals, *Journal of Geophysical Research*, 110(B7), B07301.
- Chouet, B. A., P. Dawson, and M. Martini (2008), Shallow-conduit dynamics at Stromboli Volcano, Italy, imaged from waveform inversions, *Geological Society, London, Special Publications*, 307(1), 57-84.
- Chouet, B. A., P. B. Dawson, M. R. James, and S. J. Lane (2010), Seismic source mechanism of degassing bursts at Kilauea Volcano, Hawaii: Results from waveform inversion in the 10-50 s band, *Journal of Geophysical Research*, 115(B9), B09311.
- Clague, D. A., and G. B. Dalrymple (1987), The Hawaiian-Emperor Volcanic Chain - Part I: Geologic Evolution, in *Volcanism in Hawaii*, U.S. Geological Survey Professional Paper 1350, pp. 5-54.

References

- Crafford, T. (1975), SO₂ emission of the 1974 eruption of Volcán Fuego, Guatemala, *Bulletin of Volcanology*, 39(4), 536-556.
- Dalton, M. P., I. M. Watson, P. A. Nadeau, C. Werner, W. Morrow, and J. M. Shannon (2009), Assessment of the UV camera sulfur dioxide retrieval for point source plumes, *Journal of Volcanology and Geothermal Research*, 188(4), 358-366.
- Dalton, M. P., G. P. Waite, I. M. Watson, and P. A. Nadeau (2010), Multiparameter quantification of gas release during weak Strombolian eruptions at Pacaya Volcano, Guatemala, *Geophysical Research Letters*, 37(9), L09303.
- Dawson, P. B., M. C. Benítez, B. A. Chouet, D. Wilson, and P. G. Okubo (2010), Monitoring very-long-period seismicity at Kilauea Volcano, Hawaii, *Geophysical Research Letters*, 37(18), L18306.
- Edmonds, M., R. A. Herd, B. Galle, and C. M. Oppenheimer (2003), Automated, high time-resolution measurements of SO₂ flux at Soufrière Hills Volcano, Montserrat, *Bulletin of Volcanology*, 65(8), 578-586.
- Edmonds, M., and T. M. Gerlach (2007), Vapor segregation and loss in basaltic melts, *Geology*, 35(8), 751-754.
- Edmonds, M., T. M. Gerlach, and R. A. Herd (2009), Halogen degassing during ascent and eruption of water-poor basaltic magma, *Chemical Geology*, 263(1-4), 122-130.
- Elias, T., A. J. Sutton, C. Oppenheimer, K. A. Horton, H. Garbeil, V. Tsanev, A. J. S. McGonigle, and G. Williams-Jones (2006), Comparison of COSPEC and two miniature ultraviolet spectrometer systems for SO₂ measurements using scattered sunlight, *Bulletin of Volcanology*, 68(4), 313-322.
- Endo, E. T., and T. Murray (1991), Real-Time Seismic Amplitude Measurement (RSAM) - a volcano monitoring and prediction tool, *Bulletin of Volcanology*, 53(7), 533-545.
- Fee, D., and M. Garcés (2007), Infrasonic tremor in the diffraction zone, *Geophys. Res. Lett.*, 34(16), L16826.
- Fee, D., M. Garcés, M. Patrick, B. Chouet, P. Dawson, and D. Swanson (2010), Infrasonic harmonic tremor and degassing bursts from Halema'uma'u Crater, Kilauea Volcano, Hawaii, *J. Geophys. Res.*, 115(B11), B11316.
- Ferrazzini, V., K. Aki, and B. Chouet (1991), Characteristics of seismic waves composing Hawaiian volcanic tremor and gas-piston events observed by a near-source array, *Journal of Geophysical Research*, 96(B4), 6199-6209.

References

- Firstov, P. P., and N. M. Kravchenko (1996), Estimation of the amount of explosive gas release in volcanic eruptions using airwaves, *Volcanology & Seismology*, 17(4-5), 547-560.
- Fischer, T. P., M. M. Morrissey, M. L. Calvache, D. Gomez, R. Torres, J. Stix, and S. N. Williams (1994), Correlations between SO₂ flux and long-period seismicity at Galeras Volcano, *Nature*, 368(6467), 135-137.
- Fischer, T. P., K. Roggensack, and P. R. Kyle (2002), Open and almost shut case for explosive eruptions: Vent processes determined by SO₂ emission rates at Karymsky volcano, Kamchatka, *Geology*, 30(12), 1059-1062.
- Galle, B., C. Oppenheimer, A. Geyer, A. J. S. McGonigle, M. Edmonds, and L. Horrocks (2003), A miniaturised ultraviolet spectrometer for remote sensing of SO₂ fluxes: a new tool for volcano surveillance, *Journal of Volcanology and Geothermal Research*, 119(1-4), 241-254.
- Garcés, M., A. Harris, C. Hetzer, J. B. Johnson, S. Rowland, E. Marchetti, and P. Okubo (2003), Infrasonic tremor observed at Kilauea Volcano, Hawai'i, *Geophysical Research Letters*, 30(20), 2023.
- Garcia, M. O., A. J. Pietruszka, and J. M. Rhodes (2003), A Petrologic Perspective of Kilauea Volcano's Summit Magma Reservoir, *Journal of Petrology*, 44(12), 2313-2339.
- Gerlach, T. M., and E. J. Graeber (1985), Volatile budget of Kilauea volcano, *Nature*, 313(6000), 273-277.
- Giggenbach, W. F. (1987), Redox processes governing the chemistry of fumarolic gas discharges from White Island, New Zealand, *Applied Geochemistry*, 2(2), 143-161.
- Goldstein, P., and B. Chouet (1994), Array Measurements and Modeling of Sources of Shallow Volcanic Tremor at Kilauea Volcano, Hawaii, *Journal of Geophysical Research-Solid Earth*, 99(B2), 2637-2652.
- Halsor, S. P., and W. I. Rose (1988), Common Characteristics of Paired Volcanoes in Northern Central America, *Journal of Geophysical Research*, 93(B5), 4467-4476.
- Harris, A. J. L., R. Carniel, and J. Jones (2005), Identification of variable convective regimes at Erta Ale Lava Lake, *Journal of Volcanology and Geothermal Research*, 142(3-4), 207-223.
- Helmberger, D., and R. A. Wiggins (1971), Upper Mantle Structure of Midwestern United States, *Journal of Geophysical Research*, 76(14), 3229-3245.
- Holcomb, R. T. (1987), Eruptive History and Long-Term Behavior of Kilauea Volcano, in *Volcanism in Hawaii*, U.S. Geological Survey Professional Paper 1350, pp. 261-350.

References

- Holland, A. S. P., I. M. Watson, J. C. Phillips, L. Caricchi, and M. P. Dalton (2011), Degassing processes during lava dome growth: Insights from Santiaguito lava dome, Guatemala, *Journal of Volcanology and Geothermal Research*, 202(1-2), 153-166.
- Horton, K. A., G. Williams-Jones, H. Garbeil, T. Elias, A. J. Sutton, P. Mouginis-Mark, J. N. Porter, and S. Clegg (2006), Real-time measurement of volcanic SO₂ emissions: validation of a new UV correlation spectrometer (FLYSPEC), *Bulletin of Volcanology*, 68(4), 323-327.
- Houghton, B. F., D. A. Swanson, and R. J. Carey (2009), Products of short-lived pyroclastic events during the 2008-2009 Halema`uma`u eruption, Kilauea: Implications for eruption process and hazards, *Geological Society of America Abstracts with Programs*, 41(7), 231.
- James, M. R., S. J. Lane, and B. A. Chouet (2006), Gas slug ascent through changes in conduit diameter: Laboratory insights into a volcano-seismic source process in low-viscosity magmas, *Journal of Geophysical Research*, 111(B5), B05201.
- James, M. R., S. J. Lane, and S. B. Corder (2008), Modelling the rapid near-surface expansion of gas slugs in low-viscosity magmas, *Geological Society, London, Special Publications*, 307(1), 147-167.
- Jaupart, C., and S. Vergnolle (1988), Laboratory models of Hawaiian and Strombolian eruptions, *Nature*, 331(6151), 58-60.
- Johnson, J. B., R. C. Aster, and P. R. Kyle (2004), Volcanic eruptions observed with infrasound, *Geophysical Research Letters*, 31(14), L14604.
- Johnson, J. B., A. J. L. Harris, and R. P. Hoblitt (2005), Thermal observations of gas pistonning at Kilauea Volcano, *Journal of Geophysical Research-Solid Earth*, 110, B11201.
- Jones, J., R. Carniel, A. J. L. Harris, and S. Malone (2006), Seismic characteristics of variable convection at Erta 'Ale lava lake, Ethiopia, *Journal of Volcanology and Geothermal Research*, 153(1-2), 64-79.
- Julian, B. R. (1994), Volcanic tremor - Nonlinear excitation by fluid-flow, *Journal of Geophysical Research-Solid Earth*, 99(B6), 11859-11877.
- Julian, B. R. (2000), Period doubling and other nonlinear phenomena in volcanic earthquakes and tremor, *Journal of Volcanology and Geothermal Research*, 101(1-2), 19-26.
- Kantzas, E. P., A. J. S. McGonigle, G. Tamburello, A. Aiuppa, and R. G. Bryant (2010), Protocols for UV camera volcanic SO₂ measurements, *Journal of Volcanology and Geothermal Research*, 194(1-3), 55-60.

References

- Kazahaya, K., H. Shinohara, and G. Saito (1994), Excessive degassing of Izu-Oshima Volcano - Magma convection in a conduit, *Bulletin of Volcanology*, 56(3), 207-216.
- Kazahaya, R., T. Mori, M. Takeo, T. Ohminato, T. Urabe, and Y. Maeda (2011), Relation between single very-long-period pulses and volcanic gas emissions at Mt. Asama, Japan, *Geophysical Research Letters*, 38(11), L11307.
- Kern, C., T. Deutschmann, L. Vogel, M. Wöhrbach, T. Wagner, and U. Platt (2010a), Radiative transfer corrections for accurate spectroscopic measurements of volcanic gas emissions, *Bulletin of Volcanology*, 72(2), 233-247.
- Kern, C., F. Kick, P. Lübcke, L. Vogel, M. Wöhrbach, and U. Platt (2010b), Theoretical description of functionality, applications, and limitations of SO₂ cameras for the remote sensing of volcanic plumes, *Atmospheric Measurement Techniques*, 3(3), 733-749.
- Khokhar, M. F., C. Frankenberg, M. Van Roozendaal, S. Beirle, S. Köhl, A. Richter, U. Platt, and T. Wagner (2005), Satellite observations of atmospheric SO₂ from volcanic eruptions during the time-period of 1996–2002, *Advances in Space Research*, 36(5), 879-887.
- Klauber, G. M. (1973), Ultraviolet photography of sulfur dioxide plumes, *Environmental Science & Technology*, 7(10), 953-954.
- Krueger, A. J. (1983), Sighting of El Chichón sulfur dioxide clouds with the Nimbus 7 Total Ozone Mapping Spectrometer, *Science*, 220(4604), 1377-1379.
- Kumagai, H., and B. A. Chouet (2000), Acoustic properties of a crack containing magmatic or hydrothermal fluids, *Journal of Geophysical Research-Solid Earth*, 105(B11), 25493-25512.
- Kumagai, H., B. A. Chouet, and P. B. Dawson (2005), Source process of a long-period event at Kilauea volcano, Hawaii, *Geophysical Journal International*, 161(1), 243-254.
- Lyons, J. J., G. P. Waite, W. I. Rose, and G. Chigna (2010), Patterns in open vent, strombolian behavior at Fuego volcano, Guatemala, 2005-2007, *Bulletin of Volcanology*, 72(1), 1-15.
- Lyons, J. J., and G. P. Waite (2011), Dynamics of explosive volcanism at Fuego volcano imaged with very long period seismicity, *Journal of Geophysical Research*, 116(B9), B09303.
- Manga, M. (1996), Waves of bubbles in basaltic magmas and lavas, *Journal of Geophysical Research-Solid Earth*, 101(B8), 17457-17465.

References

- Marchetti, E., and M. Ripepe (2005), Stability of the seismic source during effusive and explosive activity at Stromboli Volcano, *Geophysical Research Letters*, 32(3), -.
- Marchetti, E., M. Ripepe, A. J. L. Harris, and D. Delle Donne (2009), Tracing the differences between Vulcanian and Strombolian explosions using infrasonic and thermal radiation energy, *Earth and Planetary Science Letters*, 279(3-4), 273-281.
- Martin, D. P., and W. I. Rose (1981), Behavioral patterns of Fuego volcano, Guatemala, *Journal of Volcanology and Geothermal Research*, 10(1-3), 67-81.
- Martin, R. S., G. M. Sawyer, L. Spampinato, G. G. Salerno, C. Ramirez, E. Ilyinskaya, M. L. I. Witt, T. A. Mather, I. M. Watson, J. C. Phillips, and C. Oppenheimer (2010), A total volatile inventory for Masaya Volcano, Nicaragua, *Journal of Geophysical Research*, 115(B9), B09215.
- McGee, K. A., and T. M. Gerlach (1998), Airborne volcanic plume measurements using a FTIR spectrometer, Kilauea Volcano, Hawaii, *Geophysical Research Letters*, 25(5), 615-618.
- McGee, K. A., T. Elias, A. J. Sutton, M. P. Doukas, P. G. Zemek, and T. M. Gerlach (2005), Reconnaissance gas measurements on the East Rift Zone of Kilauea volcano, Hawai'i by Fourier transform infrared spectroscopy, U.S. Geological Survey Open File Report 2005-1062.
- McGonigle, A. J. S., A. Aiuppa, M. Ripepe, E. P. Kantzas, and G. Tamburello (2009), Spectroscopic capture of 1 Hz volcanic SO₂ fluxes and integration with volcano geophysical data, *Geophysical Research Letters*, 36, L21309.
- McNutt, S., and D. Harlow (1983), Seismicity at Fuego, Pacaya, Izalco, and San Cristobal Volcanoes, Central America, 1973–1974, *Bulletin of Volcanology*, 46(3), 283-297.
- Metaxian, J. P., P. Lesage, and J. Dorel (1997), Permanent tremor of Masaya Volcano, Nicaragua: Wave field analysis and source location, *Journal of Geophysical Research-Solid Earth*, 102(B10), 22529-22545.
- Moffat, A. J., and M. M. Millan (1971), The applications of optical correlation techniques to the remote sensing of SO₂ plumes using sky light, *Atmospheric Environment*, 5(8), 677-690.
- Molina, I., H. Kumagai, A. García-Aristizábal, M. Nakano, and P. Mothes (2008), Source process of very-long-period events accompanying long-period signals at Cotopaxi Volcano, Ecuador, *Journal of Volcanology and Geothermal Research*, 176(1), 119-133.

References

- Mori, T., and M. Burton (2006), The SO₂ camera: A simple, fast and cheap method for ground-based imaging of SO₂ in volcanic plumes, *Geophysical Research Letters*, 33(24), L24804.
- Nadeau, P. A., and G. Williams-Jones (2008), Beyond COSPEC - Recent advances in SO₂ monitoring technology, in *The COSPEC Cookbook: Making SO₂ Measurements at Active Volcanoes*, edited by G. Williams-Jones, J. Stix and C. Hickson, pp. 219-233, IAVCEI.
- Nadeau, P. A., and G. Williams-Jones (2009), Apparent downwind depletion of volcanic SO₂ flux-lessons from Masaya Volcano, Nicaragua, *Bulletin of Volcanology*, 71(4), 389-400.
- Nadeau, P. A., J. L. Palma, and G. P. Waite (2011), Linking volcanic tremor, degassing, and eruption dynamics via SO₂ imaging, *Geophysical Research Letters*, 38(1), L01304.
- Namiki, A., and M. Manga (2005), Response of a bubble bearing viscoelastic fluid to rapid decompression: Implications for explosive volcanic eruptions, *Earth and Planetary Science Letters*, 236(1-2), 269-284.
- Oppenheimer, C., A. J. S. McGonigle, P. Allard, M. J. Wooster, and V. Tsanev (2004), Sulfur, heat, and magma budget of Erta 'Ale lava lake, Ethiopia, *Geology*, 32(6), 509-512.
- Oppenheimer, C., and P. R. Kyle (2008), Probing the magma plumbing of Erebus volcano, Antarctica, by open-path FTIR spectroscopy of gas emissions, *Journal of Volcanology and Geothermal Research*, 177(3), 743-754.
- Orr, T., and M. Patrick (2009), What has driven degassing events during the 2008-2009 summit eruption of Kilauea Volcano, Hawai'i?, *Eos Transactions American Geophysical Union*, 90(52), Fall Meeting Supplement, Abstract V43G-2330
- Orr, T., M. Patrick, D. Wilson, A. J. Sutton, and T. Elias (2010), The impact of rockfalls on shallow degassing processes during the 2008-2010 summit eruption of Kilauea Volcano, Hawai'i, Abstract V21C-2340 presented at 2010 Fall Meeting, American Geophysical Union, San Francisco, Calif., 13-17 Dec.
- Palma, J. L., E. S. Calder, D. Basualto, S. Blake, and D. A. Rothery (2008), Correlations between SO₂ flux, seismicity, and outgassing activity at the open vent of Villarrica volcano, Chile, *Journal of Geophysical Research-Solid Earth*, 113(B10), B10201.
- Palma, J. L., S. Blake, and E. S. Calder (2011), Constraints on the rates of degassing and convection in basaltic open-vent volcanoes, *Geochemistry Geophysics Geosystems*, 12(11), Q11006.

References

- Parfitt, E. A., and L. Wilson (1995), Explosive volcanic eruptions-IX. The transition between Hawaiian-style lava fountaining and Strombolian explosive activity, *Geophysical Journal International*, 121(1), 226-232.
- Patrick, M., T. Orr, D. Wilson, A. J. Sutton, T. Elias, D. Fee, and P. A. Nadeau (2010), Evidence for gas accumulation beneath the surface crust driving cyclic rise and fall of the lava surface at Halema`uma`u, Kilauea Volcano, Abstract V21C-2339 presented at 2010 Fall Meeting, American Geophysical Union, San Francisco, Calif., 13-17 Dec.
- Patrick, M., T. Orr, D. Wilson, D. Dow, and R. Freeman (2011a), Cyclic spattering, seismic tremor, and surface fluctuation within a perched lava channel, Kilauea Volcano, *Bulletin of Volcanology*, 73(6), 639-653.
- Patrick, M. R., A. J. L. Harris, M. Ripepe, J. Dehn, D. A. Rothery, and S. Calvari (2007), Strombolian explosive styles and source conditions: insights from thermal (FLIR) video, *Bulletin of Volcanology*, 69(7), 769-784.
- Patrick, M. R., D. Wilson, D. Fee, T. Orr, and D. Swanson (2011b), Shallow degassing events as a trigger for very-long-period seismicity at Kilauea Volcano, Hawai'i, *Bulletin of Volcanology*, 1-8.
- Pence, W. D., L. Chiappetti, C. G. Page, R. A. Shaw, and E. Stobie (2010), Definition of the Flexible Image Transport System (FITS), version 3.0, *Astronomy & Astrophysics*, 524, A42.
- Perret, F. A. (1913), The floating islands of Halemaumau, *American Journal of Science*, 35(207), 273-282.
- Peterson, D. W., and R. B. Moore (1987), Geologic history and evolution of geologic concepts, Island of Hawaii, in *Volcanism in Hawaii*, U.S. Geological Survey Professional Paper 1350, pp. 149-189.
- Poland, M. P., A. Miklius, P. Lundgren, and A. J. Sutton (2011), Repeated deflation-inflation events at Kilauea Volcano, Hawaii: What's up (and down) with that?, V51G-01 presented at 2011 Fall Meeting, American Geophysical Union, San Francisco, Calif., 5-9 Dec.
- Prata, A. J., and J. Kerkmann (2007), Simultaneous retrieval of volcanic ash and SO₂ using MSG-SEVIRI measurements, *Geophysical Research Letters*, 34(5), L05813.
- Prata, A. J. (2011), UV Ground-based imaging camera: EnviCam, presented at Open Vent Volcanoes PASI Workshop, San Jose, Costa Rica, 15 January 2011.

References

- Press, W. H., B. P. Flannery, S. A. Teukolsky, and W. T. Vetterling (1992), Spectral Analysis of Unevenly Sampled Data, in *Numerical recipes in FORTRAN: The art of scientific computing*, edited, pp. 569-577, Cambridge University Press, Cambridge.
- Ripepe, M., and E. Gordeev (1999), Gas bubble dynamics model for shallow volcanic tremor at Stromboli, *Journal of Geophysical Research-Solid Earth*, 104(B5), 10639-10654.
- Ripepe, M., M. Coltelli, E. Privitera, S. Gresta, M. Moretti, and D. Piccinini (2001), Seismic and infrasonic evidences for an impulsive source of the shallow volcanic tremor at Mt. Etna, Italy, *Geophysical Research Letters*, 28(6), 1071-1074.
- Ripepe, M., A. J. L. Harris, and R. Carniel (2002), Thermal, seismic and infrasonic evidences of variable degassing rates at Stromboli volcano, *Journal of Volcanology and Geothermal Research*, 118(3-4), 285-297.
- Rodriguez, L. A., I. M. Watson, W. I. Rose, Y. K. Branan, G. J. S. Bluth, G. Chigna, O. Matias, D. Escobar, S. A. Carn, and T. P. Fischer (2004), SO₂ emissions to the atmosphere from active volcanoes in Guatemala and El Salvador, 1999-2002, *Journal of Volcanology and Geothermal Research*, 138(3-4), 325-344.
- Roggensack, K. (2001), Unraveling the 1974 eruption of Fuego volcano (Guatemala) with small crystals and their young melt inclusions, *Geology*, 29(10), 911-a-914.
- Rose, W. I., A. T. Anderson, L. G. Woodruff, and S. B. Bonis (1978), October 1974 basaltic tephra from Fuego Volcano - Description and history of the magma body, *Journal of Volcanology and Geothermal Research*, 4(1-2), 3-53.
- Rose, W. I., S. Self, P. J. Murrow, C. Bonadonna, A. J. Durant, and G. G. J. Ernst (2008), Nature and significance of small volume fall deposits at composite volcanoes: Insights from the October 14, 1974 Fuego eruption, Guatemala, *Bulletin of Volcanology*, 70(9), 1043-1067.
- Shannon, J. M. (2006), Development and application of new techniques for sulfur dioxide monitoring at active volcanoes, Michigan Technological University, Houghton, Michigan.
- Shinohara, H. (2005), A new technique to estimate volcanic gas composition: plume measurements with a portable multi-sensor system, *Journal of Volcanology and Geothermal Research*, 143(4), 319-333.
- Shinohara, H. (2008), Excess degassing from volcanoes and its role on eruptive and intrusive activity, *Reviews of Geophysics*, 46(4), RG4005.
- Stevenson, D. S., and S. Blake (1998), Modelling the dynamics and thermodynamics of volcanic degassing, *Bulletin of Volcanology*, 60(4), 307-317.

References

- Stix, J. (2007), Stability and instability of quiescently active volcanoes: The case of Masaya, Nicaragua, *Geology*, 35(6), 535-538.
- Stoiber, R. E., and A. Jepsen (1973), Sulfur dioxide contributions to the atmosphere by volcanoes, *Science*, 182(4112), 577-578.
- Stoiber, R. E., L. L. Malinconico, and S. N. Williams (1983), Use of the correlation spectrometer at volcanoes, in *Forecasting volcanic events*, edited by H. Tazieff and J. C. Sabroux, pp. 424-444, Elsevier, New York.
- Sumner, J. M., D. A. Rothery, O. Spieler, and D. B. Dingwell (2007), Impact vesiculation - a new trigger for volcanic bubble growth and degassing, *eEarth*, 2(4), 151-167.
- Sutton, A. J., T. Elias, T. M. Gerlach, and J. B. Stokes (2001), Implications for eruptive processes as indicated by sulfur dioxide emissions from Kilauea Volcano, Hawaii, 1979-1997, *Journal of Volcanology and Geothermal Research*, 108(1-4), 283-302.
- Swanson, D. A., W. A. Duffield, D. B. Jackson, and D. W. Peterson (1979), Chronological narrative of the 1969-1971 Mauna Ulu eruption of Kilauea volcano, Hawaii, in, U.S. Geological Survey Professional Paper 1056, p. 55.
- Sweeney, D., P. R. Kyle, and C. Oppenheimer (2008), Sulfur dioxide emissions and degassing behavior of Erebus volcano, Antarctica, *Journal of Volcanology and Geothermal Research*, 177(3), 725-733.
- Taddeucci, J., M. Pompilio, and P. Scarlato (2004), Conduit processes during the July-August 2001 explosive activity of Mt. Etna (Italy): inferences from glass chemistry and crystal size distribution of ash particles, *Journal of Volcanology and Geothermal Research*, 137(1-3), 33-54.
- Tamburello, G., E. P. Kantzas, A. J. S. McGonigle, A. Aiuppa, and G. Giudice (2011), UV camera measurements of fumarole field degassing (La Fossa crater, Vulcano Island), *Journal of Volcanology and Geothermal Research*, 199(1-2), 47-52.
- Thomas, H., and I. Watson (2010), Observations of volcanic emissions from space: current and future perspectives, *Natural Hazards*, 54(2), 323-354.
- Vandaele, A. C., C. Hermans, and S. Fally (2009), Fourier transform measurements of SO₂ absorption cross sections: II.: Temperature dependence in the 29000–44000 cm⁻¹ (227–345 nm) region, *Journal of Quantitative Spectroscopy and Radiative Transfer*, 110(18), 2115-2126.

References

- Watson, I. M., C. Oppenheimer, B. Voight, P. W. Francis, A. Clarke, J. Stix, A. Miller, D. M. Pyle, M. R. Burton, S. R. Young, G. Norton, S. Loughlin, and B. Darroux (2000), The relationship between degassing and ground deformation at Soufriere Hills Volcano, Montserrat, *Journal of Volcanology and Geothermal Research*, 98(1-4), 117-126.
- Watson, I. M., V. J. Realmuto, W. I. Rose, A. J. Prata, G. J. S. Bluth, Y. Gu, C. E. Bader, and T. Yu (2004), Thermal infrared remote sensing of volcanic emissions using the moderate resolution imaging spectroradiometer, *Journal of Volcanology and Geothermal Research*, 135(1-2), 75-89.
- Whittington, A., P. Richet, and F. Holtz (2000), Water and the viscosity of depolymerized aluminosilicate melts, *Geochimica Et Cosmochimica Acta*, 64(21), 3725-3736.
- Williams-Jones, G., J. Stix, M. Heiligmann, J. Barquero, E. Fernandez, and E. D. Gonzalez (2001), A model of degassing and seismicity at Arenal Volcano, Costa Rica, *Journal of Volcanology and Geothermal Research*, 108(1-4), 121-139.
- Williams-Jones, G., K. A. Horton, T. Elias, H. Garbeil, P. J. Mouginiis-Mark, A. J. Sutton, and A. J. L. Harris (2006), Accurately measuring volcanic plume velocity with multiple UV spectrometers, *Bulletin of Volcanology*, 68(4), 328-332.
- Wilson, D., T. Elias, T. Orr, M. Patrick, J. Sutton, and D. Swanson (2008), Small Explosion From New Vent at Kilauea's Summit, *Eos Transactions American Geophysical Union*, 89(22), 203.
- Witham, F., A. Woods, and C. Gladstone (2006), An analogue experimental model of depth fluctuations in lava lakes, *Bulletin of Volcanology*, 69(1), 51-56.
- Yuan, A. T. E., S. R. McNutt, and D. H. Harlow (1984), Seismicity and eruptive activity at Fuego Volcano, Guatemala: February 1975 –January 1977, *Journal of Volcanology and Geothermal Research*, 21(3-4), 277-296.

Appendix A: SO₂ EMISSIONS AT FUEGO VOLCANO, 2008

A.1 Introduction

Initial field testing of the UV camera, as it pertains to this dissertation, was carried out in Guatemala in January of 2008. While a more devoted data collection campaign was carried out at Fuego volcano specifically in January of 2009, the small, preliminary dataset that resulted from initial testing itself has yielded exciting results in conjunction with coincident seismic data.

A.2 UV camera measurements

Measurements with the UV camera in 2008 were carried out in a similar fashion to that described in Chapter 3. The camera system included an Apogee Alta U6 camera outfitted with a CoastalOpt 105 mm UV lens. A filter wheel was placed on in front of the lens and included two full width half max bandpass filters from Andover Optics, with center wavelengths at 307 and 326 nm. The filter wheel was controlled via a USB wire separate from that of the camera body itself. The entire package was placed on a tripod approximately 1 km, and ~200 m below, Fuego’s active summit, on the slope of the Meseta edifice. No lava flows were present during the measurements; the only visible activity aside from a passively degassing plume were small, ash-rich explosions occurring approximately once per hour.

Data acquisition protocol followed *Bluth et al.* [2007] and *Dalton et al.* [2009], with modifications for the use of two filters. While a dual-filter method is preferable to a single-filter approach for the purpose of isolating the absorbance of SO₂, it became clear following data acquisition that successive images were not similar enough to allow overlay and image

processing as a pair. Accordingly, only imagery acquired with the 307 filter was ultimately useful, and had a temporal resolution half that of the overall image acquisition.

Raw UV camera images were processed with Matlab using the routines described in Chapter 2 in order to derive time-series of integrated column amount, plume speed, and, ultimately, emission rate of SO₂.

A.3 Seismic measurements

A small antenna of 5 broadband seismometers (30 second Güralp CMG-40Ts with Reftek 130 digitizers) was installed on the northeast flank of Fuego, on the western side of the Meseta edifice between the vent and the UV camera. The seismic array had stations spaced 30 m apart and a total aperture of ~140 m. Data presented in this study are from the station at the corner of the array, nearest the UV camera and also the station in operation most consistently over the course of the field campaign.

A.4 Results and preliminary discussion

UV camera image acquisition resulted in 875 images obtained over ~80 minutes on the morning of 15 January 2008. Imagery was processed using the programs described in Chapter 2. Calculated emission rates of SO₂ were comparable to those measured the following year [Nadeau *et al.*, 2011] and ranged from a minimum of 0.55 kg/s to a maximum of 2.98 kg/s and had a mean of 1.44 kg/s. Results are displayed in Figure A.1. No explosions occurred during the acquisition of the 2008 data; all emissions are inter-explosion passive degassing and all imagery acquired with the 307 nm filter was therefore useable.

Initial inspection of the time-series reveals a pseudo-cyclic appearance, with well-defined peaks and troughs in the dataset. A quasi-10-minute periodicity noted in both SO₂ emission rate (DOAS) [Sweeney *et al.*, 2008] and gas composition (FTIR) [Oppenheimer and Kyle, 2008] data allowed for recognition of open-system degassing and convection as possible

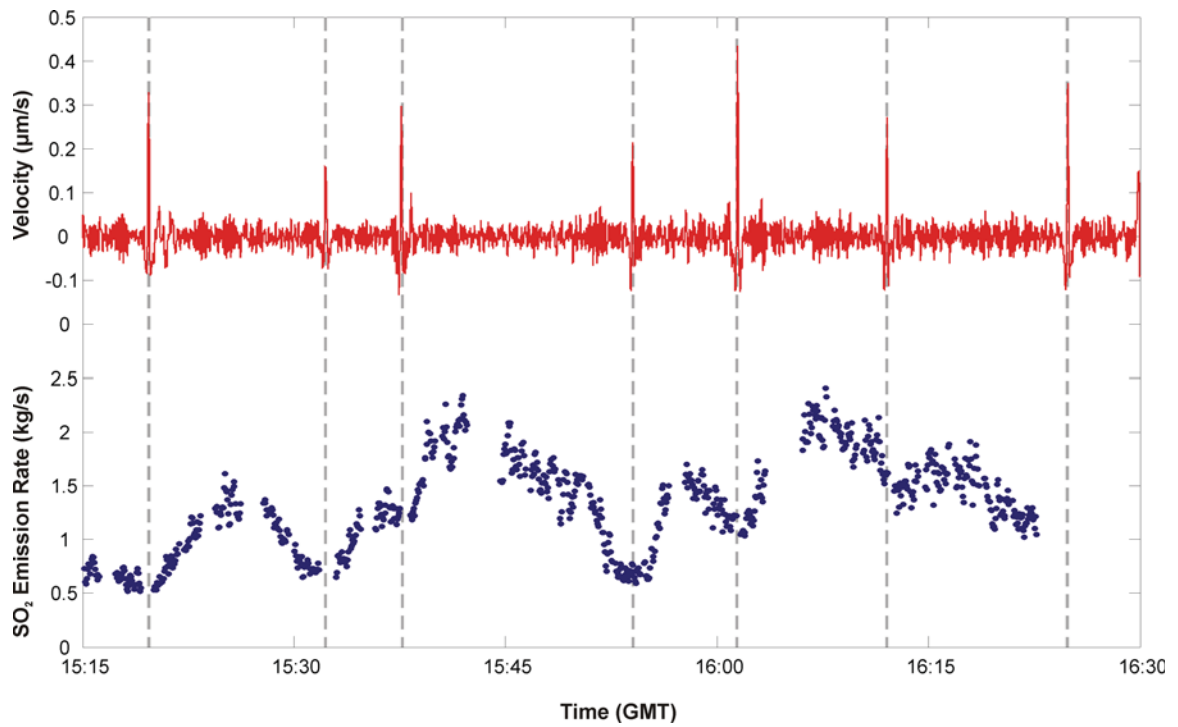


Figure A.1: VLP (12 – 60 s) seismic velocity and SO_2 emission rate at Fuego volcano, January 15, 2008. Dashed gray lines are coincident with maximum VLP velocity and extend into the SO_2 portion of the plot to indicate VLP occurrences relative to the SO_2 peaks that follow.

Appendix A – Fuego VLPs, 2008

sources of short-term variability in SO₂ emission rate at Erebus [Sweeney *et al.*, 2008]. Recognition of similar periodicity within the fluctuations of the SO₂ emission rate at Fuego could be valuable when dominant frequencies are compared to the occurrences of various seismic or acoustic events thought to be driven by degassing processes (i.e., long-period events, explosions). The Lomb-Scargle periodogram is able to identify both the presence and strength of periodic signals in a dataset, even when data are unevenly distributed in the temporal domain [Press *et al.*, 1992]. The analysis, however, revealed no consistent results in the 2008 Fuego SO₂ data that could be related to the seismic data, indicating no time-dependent pattern of SO₂ emissions.

Seismicity was dominated by constant tremor at ~2 Hz and small, repetitive low-frequency events that had no acoustic expression. Further filtering of the seismic data to very long periods (VLP; 12 – 60 s) revealed the occurrence of six VLP seismic events with contemporaneous UV camera data (Figure A.1).

VLPs are typically attributed to large-scale fluid flow and volumetric sources, as time scales associated with such long periods are much longer than those of LP events or tremor, and with the advent of broadband seismometer use at volcanoes, observations of VLP events have become prevalent at many types of volcanoes. The VLPs vary from volcano to volcano and are associated with a range of activities at volcanoes with compositions ranging from basalt, such as at Kilauea and Stromboli to more viscous systems like Popocatepetl. Accompanying the range of VLP phenomena is a range of interpretations of their sources. VLP events occurring with LP events at Cotopaxi volcano, Ecuador, have been interpreted to be the manifestation of a crack opening repeatedly to expel pressurized gas at depth [Molina *et al.*, 2008], while VLPs at Stromboli are inferred to be the result of bubbles in the magma column coalescing into a larger slug [Marchetti and Ripepe, 2005] or the movement of a large slug around discontinuities in the conduit [Chouet *et al.*, 2008], and those at Erebus the result of the ascent of a previously coalesced gas slug [Aster *et al.*, 2003]. Laboratory model

Appendix A – Fuego VLPs, 2008

experiments by *James et al.* [2006], indicate that slug flow through conduit geometry changes could be the source of volcanic VLP events.

Lyons and Waite [2011] examined VLP events recorded at Fuego during the 2009 field campaign conducted in conjunction with Chapter 3. Waveform inversion of VLPs associated with the largest explosions indicated a VLP source represented best by two intersecting cracks ~ 300 m below and to the west the summit vent. That result, along with inflation prior to explosions and patterns of SO_2 decrease leading up to explosions [*Nadeau et al.*, 2011], led to the interpretation that, with more viscous and crystallized basalt than volcanoes like Stromboli and Kilauea, Fuego generated VLP signals via cycles of pressurization and depressurization resulting from degassing-induced crystallization of magma in one of the source cracks [*Lyons and Waite*, 2011].

In 2008, as opposed to only the largest explosions, VLPs occurred during inter-explosion periods. Qualitative assessment of the seismic and gas datasets indicates VLPs occur in minima in the SO_2 time-series and that larger amplitude VLP events are followed by larger pulses of SO_2 emissions. SO_2 masses associated with the six events are 769 kg, 339 kg, 1410 kg, 527 kg, 1075 kg, and 908 kg of SO_2 , respectively. A caveat of these SO_2 masses is that, as the puffs from each VLP overlap in time, some SO_2 from the preceding VLP puff may be erroneously attributed to the next VLP, skewing the masses to lower values for the first of a closely spaced puff pair and higher for the second. Also of note is that larger amplitude seismic and degassing events occur following shorter preceding inter-event times. This seems counterintuitive to the model of *Lyons and Waite* [2011], which requires crystallization, pressurization, and brittle failure of the cooled upper portion of the magma column to generate a VLP event. In such a case, it would be expected that longer repose periods between events would generate larger subsequent event. This point, coupled with the ash-free gas pulses associated with the 2008 VLP events, hint at the presence of a different trigger for the VLPs in 2008. In contrast, although exact determination of the onset of SO_2 increase following a VLP is complicated by gaps in the gas dataset and smaller

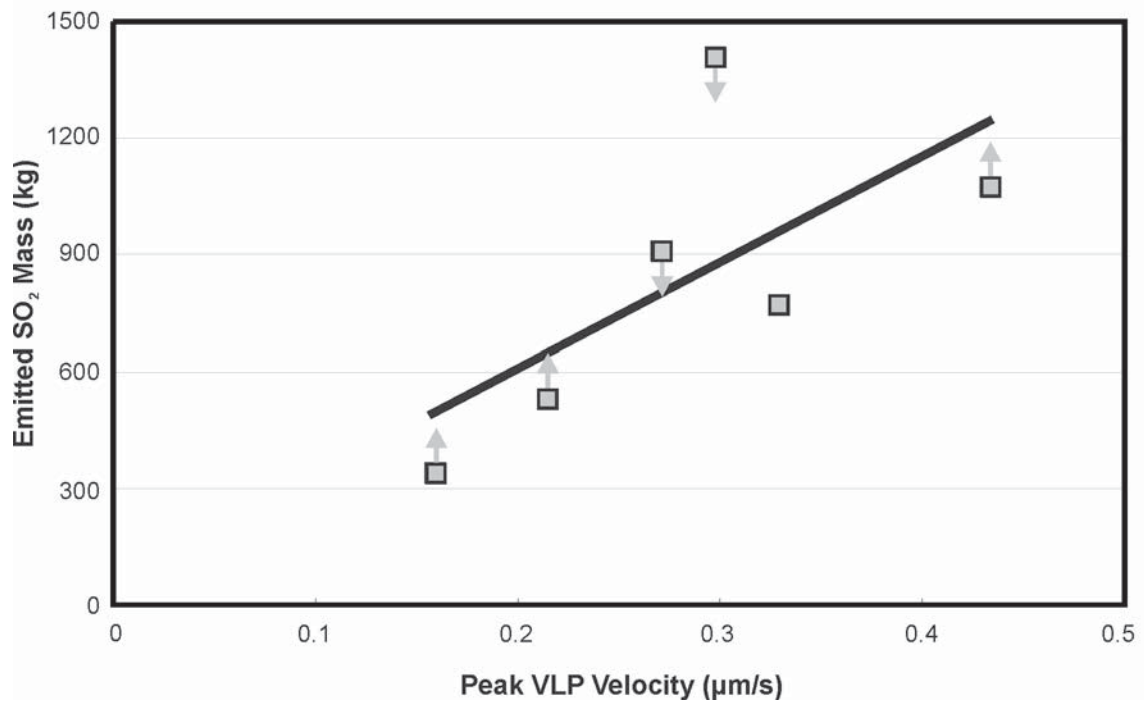


Figure A.2: Peak VLP velocity versus emitted SO_2 mass for six VLP events at Fuego volcano in 2008. Calculated masses are likely over- or under-estimates of true masses for each VLP, as associated puffs overlap, leading to misallocation of some SO_2 ; gray arrows indicate the direction in which the true mass would plot. Arrows indicate direction only and do not indicate the degree of over- or under-estimation. The correlation coefficient for trend line is 0.67.

variations overprinting the longer-term trends, lag times from peak VLP amplitude to the start of the uptick in SO₂ emissions, ranging from ~35 to ~85 s, appear to be longer for smaller amplitude VLPs. Of the six VLPs occurring during the SO₂ time series, the largest three are associated with the three fastest appearances of increased SO₂ at the surface, as well as the three largest SO₂ pulses. These facts may support the same VLP trigger mechanism described by *Lyons and Waite* [2011], with increased overpressurization at depth causing a larger seismic event in tandem and the release of a larger volume of gas that reaches the surface faster, owing to the increased pressure at depth.

Future work on the Fuego 2008 UV camera data includes modeling of total gas volumes derived from both gas and seismic data, as well as derivation of the seismic moment of the VLP events via waveform inversion. Similar work on Asama volcano, Japan, yielded results that indicated VLP seismic moment and associated gas pulse volumes were positively correlated and that degassing via other means dominated over VLP-related degassing by a factor of four [*Kazahaya et al.*, 2011]. A short manuscript, using the UV camera and VLP data, will be prepared, with Dr. Waite as first author on the paper.

A.5 References

- Aster, R., S. Mah, P. Kyle, W. McIntosh, N. Dunbar, J. B. Johnson, M. Ruiz, and S. McNamara (2003), Very long period oscillations of Mount Erebus Volcano, *J. Geophys. Res.*, 108(B11), 2522.
- Bluth, G. J. S., J. M. Shannon, I. M. Watson, A. J. Prata, and V. J. Realmuto (2007), Development of an ultra-violet digital camera for volcanic SO₂ imaging, *Journal of Volcanology and Geothermal Research*, 161(1-2), 47-56.
- Chouet, B. A., P. Dawson, and M. Martini (2008), Shallow-conduit dynamics at Stromboli Volcano, Italy, imaged from waveform inversions, *Geological Society, London, Special Publications*, 307(1), 57-84.
- Dalton, M. P., I. M. Watson, P. A. Nadeau, C. Werner, W. Morrow, and J. M. Shannon (2009), Assessment of the UV camera sulfur dioxide retrieval for point source plumes, *Journal of Volcanology and Geothermal Research*, 188(4), 358-366.

Appendix A – Fuego VLPs, 2008

- James, M. R., S. J. Lane, and B. A. Chouet (2006), Gas slug ascent through changes in conduit diameter: Laboratory insights into a volcano-seismic source process in low-viscosity magmas, *Journal of Geophysical Research*, 111(B5), B05201.
- Kazahaya, R., T. Mori, M. Takeo, T. Ohminato, T. Urabe, and Y. Maeda (2011), Relation between single very-long-period pulses and volcanic gas emissions at Mt. Asama, Japan, *Geophysical Research Letters*, 38(11), L11307.
- Lyons, J. J., and G. P. Waite (2011), Dynamics of explosive volcanism at Fuego volcano imaged with very long period seismicity, *Journal of Geophysical Research*, 116(B9), B09303.
- Marchetti, E., and M. Ripepe (2005), Stability of the seismic source during effusive and explosive activity at Stromboli Volcano, *Geophysical Research Letters*, 32(3), -.
- Molina, I., H. Kumagai, A. García-Aristizábal, M. Nakano, and P. Mothes (2008), Source process of very-long-period events accompanying long-period signals at Cotopaxi Volcano, Ecuador, *Journal of Volcanology and Geothermal Research*, 176(1), 119-133.
- Nadeau, P. A., J. L. Palma, and G. P. Waite (2011), Linking volcanic tremor, degassing, and eruption dynamics via SO₂ imaging, *Geophysical Research Letters*, 38(1), L01304.
- Oppenheimer, C., and P. R. Kyle (2008), Probing the magma plumbing of Erebus volcano, Antarctica, by open-path FTIR spectroscopy of gas emissions, *Journal of Volcanology and Geothermal Research*, 177(3), 743-754.
- Press, W. H., B. P. Flannery, S. A. Teukolsky, and W. T. Vetterling (1992), Spectral Analysis of Unevenly Sampled Data, in *Numerical recipes in FORTRAN: The art of scientific computing*, edited, pp. 569-577, Cambridge University Press, Cambridge.
- Sweeney, D., P. R. Kyle, and C. Oppenheimer (2008), Sulfur dioxide emissions and degassing behavior of Erebus volcano, Antarctica, *Journal of Volcanology and Geothermal Research*, 177(3), 725-733.

Appendix B: SUPPLEMENT TO CHAPTER 2 – UVCAMSO2: IMAGE PROCESSING PROGRAM FOR EXTRACTION OF SO₂ EMISSION RATES FROM UV IMAGERY (USER MANUAL AND TUTORIAL)*

B.1 Introduction

The UVCamSO2 suite of programs, created using Matlab R2008b, provides a means by which to view and process UV camera images in order to extract high temporal resolution datasets of emission rates of volcanic SO₂. Various graphical user interfaces (GUIs) allow even user unfamiliar with Matlab to display imagery, create AVI files from image sequences, and derive emission rates and plume speeds. More advanced users may take advantage of Matlab's programming capabilities to further modify the codes to suit their own needs.

UVCamSO2 comprises seven modules linked by one main GUI interfaces, and several accessory routines. To ensure that the program will run properly, check that you have each of the required m-files:

- Main GUI interface:
UVCamSO2.fig
UVCamSO2.m
- Modules:
uvdisplay.m (static display of single or multiple images)
uvcam_moviemake.m (AVI movie file creation)
multi_image_processing_code.m (calculation of integrated column amount of SO₂)
plumespeed.m (derivation of plume speed)
backcalc.m (correction of image times from measurement time to emission time)
ERcalc.m (emission rate calculations)
readSO2.m (display of previously processed datasets)

* This appendix, along with Chapter 2 and Appendices C and D, is in review as:

Nadeau, P. A. and Palma, J.L., A Matlab Program for Deriving Emission Rates of Volcanic SO₂ from UV imagery. *Computers & Geosciences*.

Appendix B – UVCamSO2 Tutorial

- Accessory routines:
 - bresenham.m (profile line delineation)
 - imSelectROI.m (region-of-interest selection)
 - hanningsmooth_JL (vector smoothing algorithm)

To use the program, create a new folder to host the files and set the folder as the working directory in Matlab. A separate data folder is also required, which may contain your own data or the 204 sample files included with the codes. This tutorial guides first time users through the use of each of the modules of the program. While this document is designed as a step-by-step tutorial for using the sample data, it also serves as a user manual, as the same data processing procedures can be used on any similar set of UV camera data.

During the tutorial, the user will be exposed to some raw UV camera images, as well as imagery at various stages of processing, in order to familiarize the user with the data and the program. Image display is followed by processing of sample data from May of 2010 at Kilauea volcano, Hawaii, for experience with deriving SO₂ emission rates from UV camera images.

With your Matlab working directory set to the folder that houses the program codes (Figure B.1), type '**UVCamSO2**' (without quotes) into the command window and press 'Enter' (Figure B.2). The main GUI menu for the program will open and present you with seven options (Figure B.3).

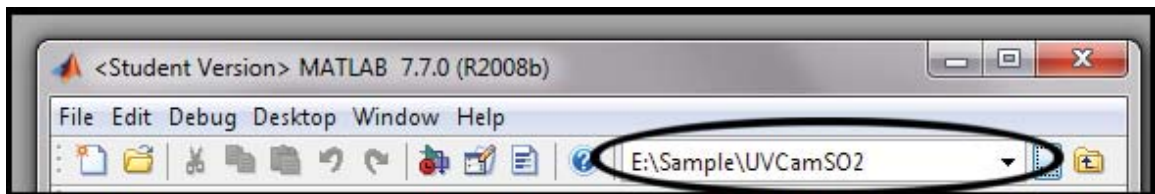


Figure B.1: Sample of correctly set Matlab working directory file path

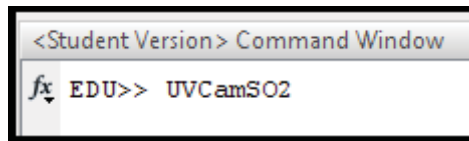


Figure B.2: Entry of program name in Matlab command window

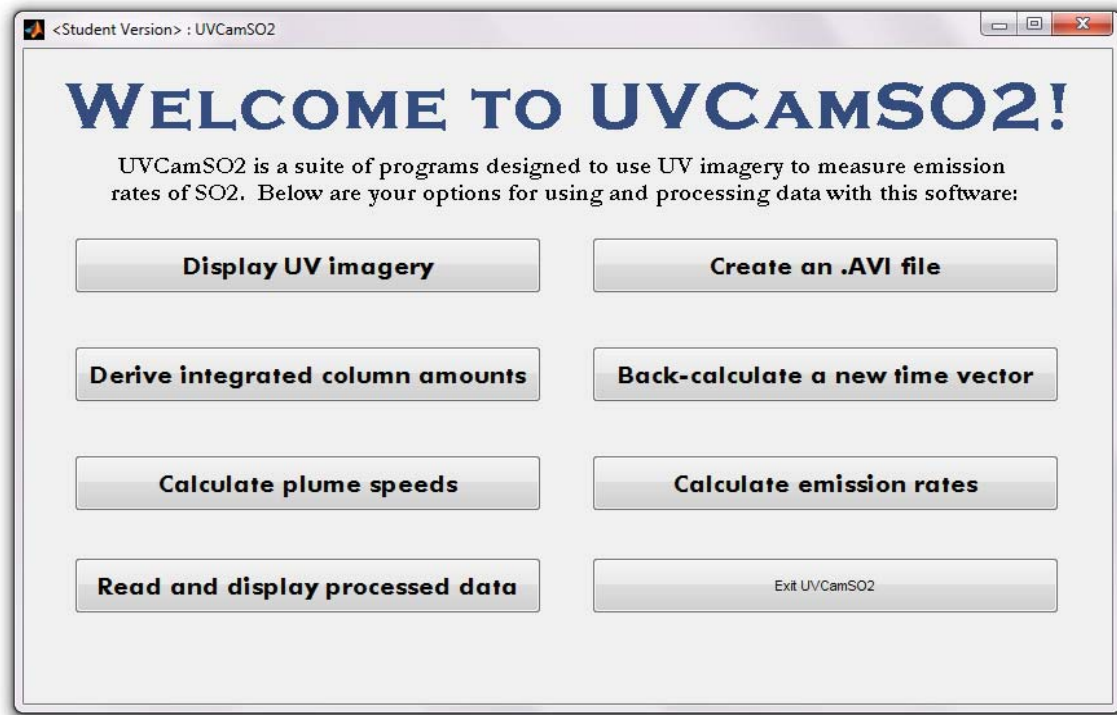


Figure B.3: Main GUI interface for UVCamSO2 program

B.2 Display of individual images

- 1) Especially if you are a first-time user of the program, you should first familiarize yourself with UV camera image files. To do so, by displaying individual images for viewing, click on the button labeled 'Display UV imagery.'

Appendix B – UVCamSO2 Tutorial

- 2) First let's just look at a raw image taken straight from the UV camera. A menu will pop up asking which type of display you would like to create (Figure B.4). Select the '**Single filter raw**' option and click '**OK**'. Now a window will pop up asking which file(s) you would like to display (Figure B.5). Select the image called '**Image307-001.fit**' and click '**Open**'.

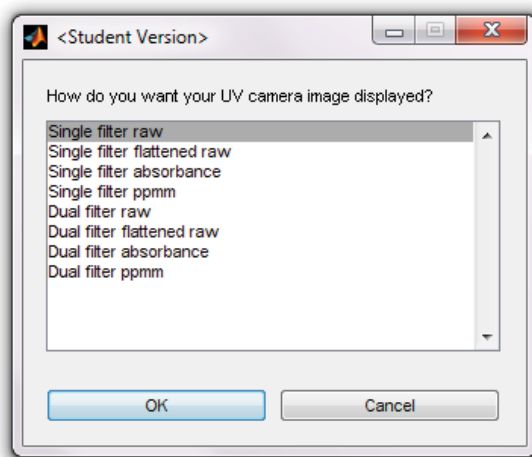


Figure B.4: Display type menu in image display module

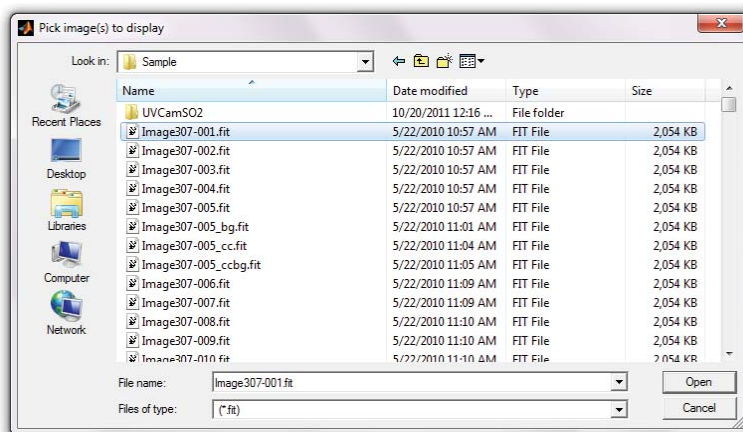


Figure B.5: File selection menu for image display module

Appendix B – UVCamSO₂ Tutorial

Now what you are seeing is a UV image of Kilauea volcano's summit plume. Because the image has not been processed yet, units are not in concentration path-length units, but are just pixel brightnesses. You can see that the SO₂ in the plume appears darker than the sky as a result of the absorption of incoming UV radiation. (There are also a few meteorological clouds as wisps in the background.) However, do you also see that the corners of the image are darker than the middle?

The darkening of the corners of the images is caused by interaction of the incoming light with the lens and lens aperture. Light coming in at the edges of the image are shielded by the lens itself, and leads to darkening at the edges of the images. This effect is larger for larger aperture openings in the lens.

- 3) In the raw imagery, where we are measuring only brightness and not SO₂, a dark corner is no different than a dark plume. To correct for this effect, we use an image taken on clear background sky. To see what one of these looks like, click on the button labeled **'Display UV imagery'** again, select **'Single filter raw'** again, and now select the file called **'Image307-005_bg.fit'** and click **'Open.'**

Now you are seeing an image of uniform clear sky, but you can see the darkening at the edges of the image again. But this darkening pattern is nearly identical in this image and the plume image we already looked at. So by combining the two, we can isolate the plume in our first image. To do this, we just divide the plume image by the background image.

- 4) To see what one of these corrected images looks like, again click **'Display UV imagery'** and select **'Single filter flattened raw.'** Then click **'OK.'** In the first window that pops up, select the same image we looked at already, **'Image307-001.fit.'** In the second pop-up window, select **'Image307-005_bg.fit'** again. This is the background image we need, so select it and click **'Open.'**

Appendix B – UVCamSO2 Tutorial

Now you can see that the darkening at the edges is mostly gone. Compare it to the first image you displayed.

- 5) The imagery still includes no information pertaining to SO_2 . For that you will need to relate the plume image to an image of something with known SO_2 concentration path-length. To do this, there is set of calibration cells that have been photographed in separate images. For an example, click '**Display UV imagery**' again, select '**Single filter flattened raw,**' and click '**OK.**' Now instead of choosing a plume image to display, we will choose the image of calibration cells. In the window that pops up, select '**Image307-005_cc.fit,**' and next select the same background image you used before, '**Image307-005_bg.fit,**' and click '**OK.**'

The image you now see is of seven calibration cells with SO_2 in known concentration path-lengths, which are in units of $\text{ppm}\cdot\text{m}$ (Figure B.6).

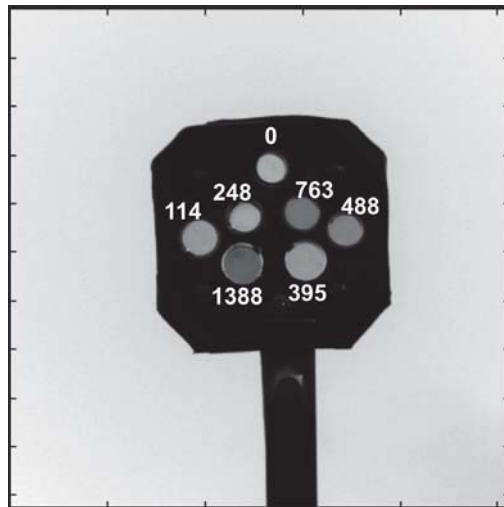


Figure B.6: Sample calibration cell image, with corresponding concentration path-length values labeled in white (units of $\text{ppm}\cdot\text{m}$)

- 6) You can use calibration images to display plume images as maps of SO₂ concentration path-length. To do this, again select **‘Display UV imagery’** and then choose **‘Single filter ppmm’** and click **‘OK.’** In the first pop-up, we will select the plume image we want to convert. Choose **‘Image307-001.fit’** again. In the second pop-up, we will select the same background image as before, **‘Image307-005_bg.fit’**. In the third pop-up, select the calibration image again, **‘Image307-005_cc.fit.’**

Now another box will ask you to enter the concentration path-lengths of the cells, in increasing order. So type **[0 114 248 395 488 763 1388]**. *Make sure to include the square brackets and to leave a space between each value* (Figure B.7). Then click **‘OK.’**

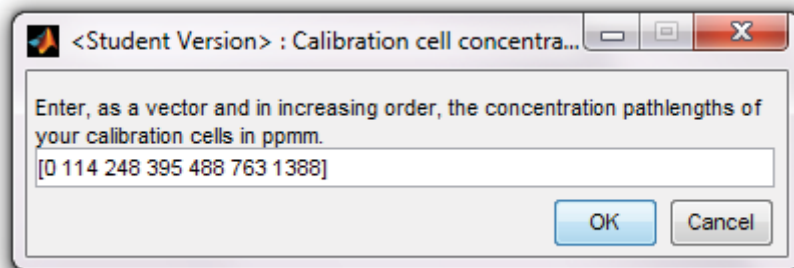


Figure B.7: Sample entry of calibration cell concentrations, including necessary square brackets

Now a box will prompt you to select the region of the 0 ppm•m cell. Click **‘OK.’** In the next window, you will draw a box within the 0 ppm•m cell, which we know is the top cell of the 7 cells (Figure B.6). **Click once to mark the upper left corner of the box, and then move your cursor to where you want the lower right corner of the box and click again.** *Make sure not to include any part of the holder or the cell edge in the box.* If you make a mistake, simply click the **‘Start Over’** button at the lower left and begin a new box. You can also use the zoom-

Appendix B – UVCamSO2 Tutorial

in drop-down menu if necessary. Once you are satisfied with the box drawn on the 0 ppm•m cell, click the box marked **‘Done’** at the lower right (Figure B.8).

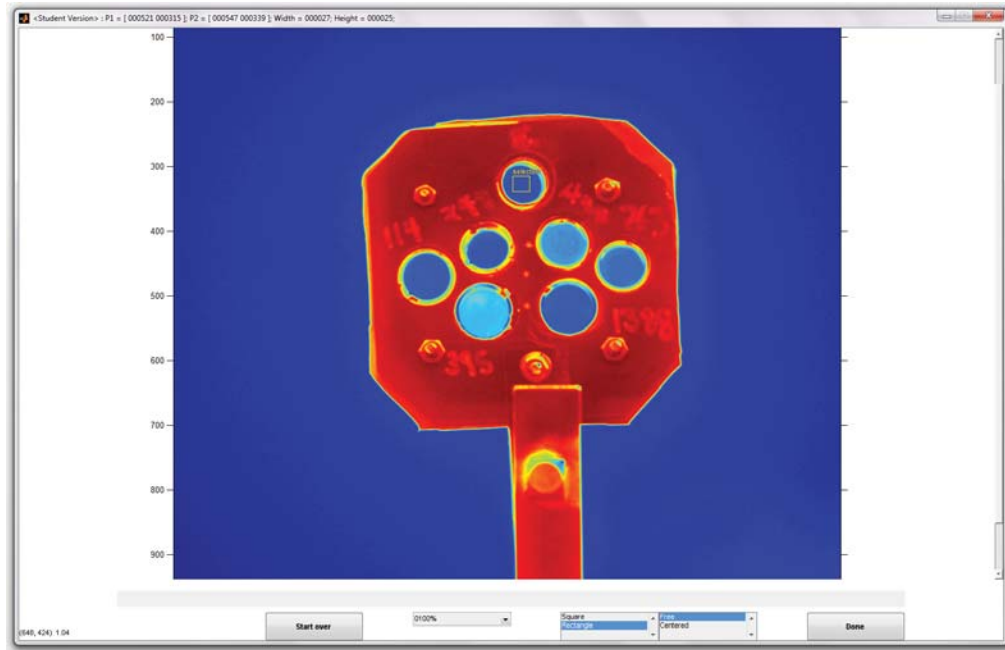


Figure B.8: Example of proper selection of the 0 ppm•m calibration cell

Now the code will prompt you to do the same box selection in the other six calibration cells, in order of increasing concentration path-length. Select the boxes for these cells just as you did previously for the 0 ppm•m cell.

The display now shows the map of SO₂ concentration path-length of the plume. However, you can see that the volcanic edifice, because it reflects very little UV and looks dark in the raw imagery, is now registering as very high SO₂ values, so we don't see much definition within the plume. We need to change the scale of our colorbar. At the top of the image window, click on **‘Edit’** and select **‘Colormap...’** (Figure B.9). In the window that opens, change the color data min and max to what you think best displays the image, then click **‘OK’**.

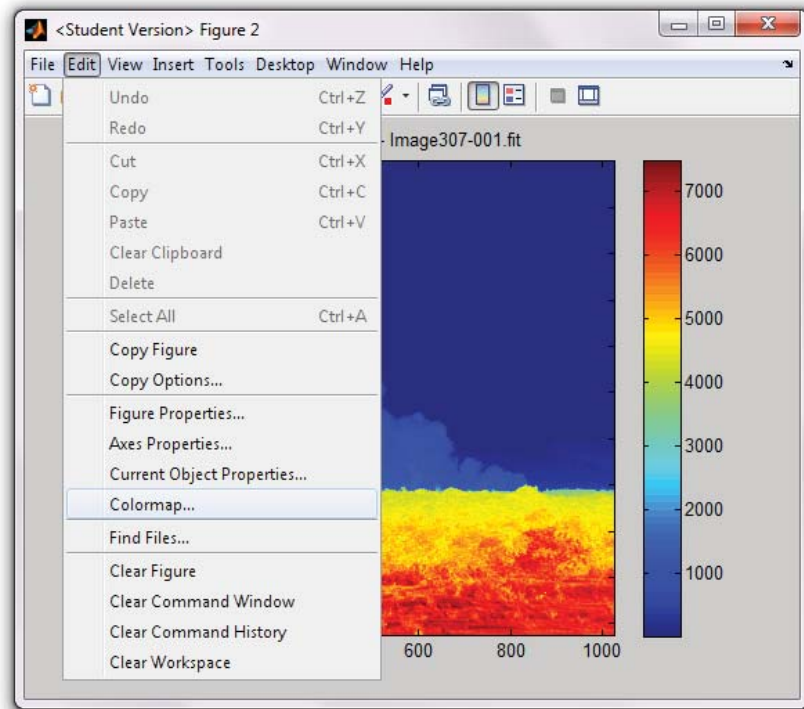


Figure B.9: Menu for navigating to colormap editing

Now the plume is displayed over a broader color range and you can see variations much better.

B.3 Creating movies with multiple images

- 3) The benefit of the UV camera is that we can get a time series of SO₂ emission rates with a high temporal resolution. So now we will look at all of the images we are about to analyze. On the main GUI window, click 'Create an .AVI file.'

A pop-up will appear asking if you whether you would like to use images from just the 307 nm filter, or both the 307 and 326 nm filters. The use of two filters is important when extracting SO₂ emission rates from images of plumes

comprising more than mostly just SO₂. Using two filters is not crucial for simply viewing the images in a movie, so click '**307 only**.' In the next drop down list, you should navigate to the folder called where you have stored the sample imagery, make sure it is selected, and click then '**OK**.'

- 4) When the next window pops-up (Figure B.10), you will need to fill in the blanks with the appropriate information about the imagery and the movie file you are creating. For the sample imagery included with this tutorial, the file prefix is '**Image307-**' and there are 100 images to be processed, with the first one being numbered '**1**.' Whether or not you only include every other image in your movie and what frame rate you use is user preference. When the information has all been entered, click '**OK**.'

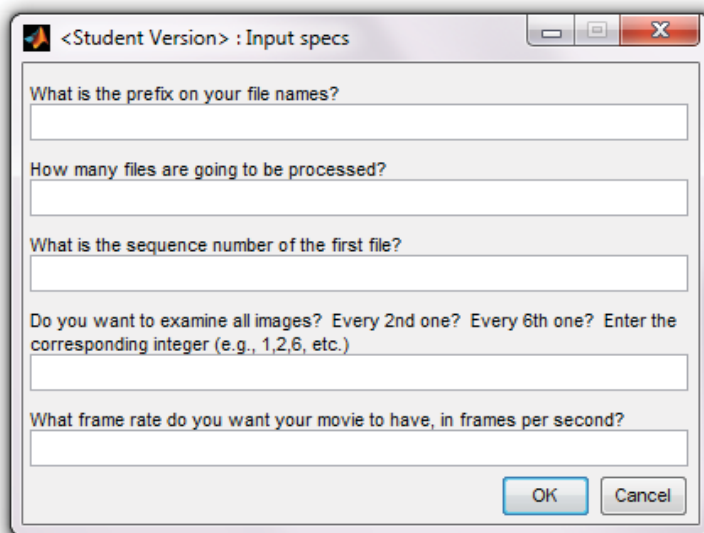


Figure B.10: Input box for movie creation module

- 5) The next window asks if you want to 'flatten' the images. This is what we have just done using the background with the darkened corners, is user preference. If you opt to flatten the images, click '**Yes**', and in the next window enter **[5]**,

Appendix B – UVCamSO2 Tutorial

including the square brackets (Figure B.11). Image 5 is the location in the image acquisition sequence that the background image was acquired.

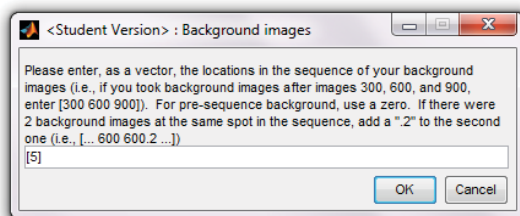


Figure B.11: Entry of background image locations, including square brackets

If you opt to flatten the images, another box will pop up asking you if you would like to convert the images to maps of concentration path-length ($\text{ppm}\cdot\text{m}$). Again, this is user preference for the individual movie you are creating. If you select 'Yes,' you will then enter both the image number of the calibration image ([5], as with the background image) and the concentration path-lengths of the cells, in increasing order. So type [0 114 248 395 488 763 1388]. *Make sure to include the square brackets and to leave a space between each value* (Figure B.12). Then click 'OK' and identify your boxes within the calibration cells as you did previously for single images.

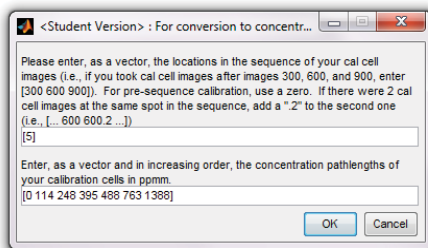


Figure B.12: Entry of background image location and calibration cell values, including square brackets

Appendix B – UVCamSO2 Tutorial

- 6) You will now be asked if you would like to compress the movie file you are creating; this is user preference. A question about the imagery's time stamp will also pop up (Figure B.13). FITS file headers include a time stamp from the time of imagery acquisition, but depending on the settings of the computer acquiring the images, the time stamp may not be in the time zone you prefer. In the case of these Kilauea images, the pop up box indicates that the first image's time stamp is 14:57:39, which is time time stamp of the image in Eastern Daylight Time (where the computer was set). To stamp the frames in the movie with either GMT or local time, an offset is required. Click '**Offset by hour(s)**' and enter '-6' for the offset from Eastern Daylight Time to Hawaiian Standard Time.

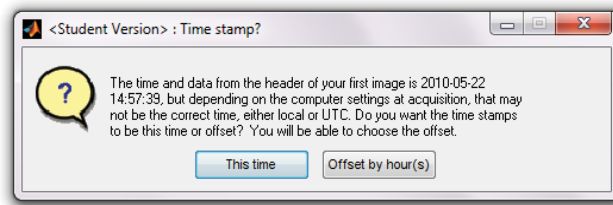


Figure B.13: Prompt for optional time stamp offset

- 7) Now you will be seeing the individual images that will be movie frames show up on your screen. If you would like to see the images again, you can open the folder where all of the files are in Windows and open the .avi file you just made in Windows Media Player or another media program.

Notice the different structures and puffs you can see in the plume; we will measure these variations in emission rates below.

B.4 Deriving integrated column amounts of SO₂

The goal of acquiring these UV camera images is to derive emission rates of SO₂, and we want to get time-series of emission rates, not just a single rate from an individual image. The equation for this is below:

$$\text{Emission Rate of SO}_2 = [\text{SO}_2]_{\text{pl}} * \cos\theta * d_{\text{seg}} * v_{\text{pl}} * C_{\text{F}}$$

where $[\text{SO}_2]_{\text{pl}}$ is the average path-length concentration of SO₂ (ppm·m) in a given slice through the plume, θ (°) is the deviation from perpendicularity of the slice of plume with respect to the gas plume's direction of propagation and d_{seg} is the width (m) of the plume over that slice. The term v_{pl} is the average plume speed (m s⁻¹) and C_{F} is a conversion factor changing ppm·m³ s⁻¹ into metric tones per day (t d⁻¹).

For now you will concentrate on the $[\text{SO}_2]$, the average concentration and d_{seg} , the width of the plume, which can be combined into one value: the Integrated Column Amount (ICA), with units of ppm·m². And we will account for $\cos\theta$ by drawing our slice, or profile, of the plume perpendicular to the direction the plume is moving.

- 1) To get a time series of ICA, go back to the main GUI and click on **'Derive integrated column amounts.'**
- 2) First the code will ask if you want to process one filter wavelength or two. Two filter wavelengths is better for isolating SO₂ from other interfering species, which can be a problem in Kilauea's plume, so we will use images from both the 307 nm and the 326 nm filters. Click **'307 and 326.'**
- 3) In the next drop down list, you should navigate to the folder where your images are stored and click **'OK'**.
- 4) The next pop-up window requires input information about the images to be processed (Figure B.14). For the sample Kilauea data, enter the following input

Appendix B – UVCamSO2 Tutorial

variables about the data, and *make sure to include the square brackets in the bottom four blanks*:

307 prefix: **Image307-**

326 prefix: **Image326-**

Number of files for each filter: **100**

Number at the end of the first file: **1**

Examine all images: **1**

Distance from the camera to the plume (in meters): **7000**

Background image locations: **[5]**

Calibration image locations: **[5]**

Profile image locations: **[1 6]**

Calibration cell concentration path-lengths: **[0 114 248 395 488 763 1388]**

<Student Version> : Initial input for UV camera data processing:

What is the prefix on your 307 file names?
Image307-

What is the prefix on your 326 file names?
Image326-

How many files (for each filter) are going to be processed?
100

What is the number at the end of the first file? (If includes zeros, as will 006 or 035, DO NOT include the zeros)
1

Do you want to examine all images? Every 2nd one? Every 6th one? Enter the corresponding integer (e.g., 1,2,6, etc.)
1

How far was the camera from the plume in meters?
7000

Please enter, as a vector, the locations in the sequence of your background images (i.e., if you took background images after images 300, 600, and 900, enter [300 600 900]). For pre-sequence background, use a zero. If there were 2 background images at the same spot in the sequence, add a ".2" to the second one (i.e., [... 600 600.2 ...]).
[5]

Please enter, as a vector, the locations in the sequence of your cal cell images (i.e., if you took cal cell images after images 300, 600, and 900, enter [300 600 900]). For pre-sequence (assuming your sequence starts at 1) cal cells, use a zero. If there were 2 cal cell images at the same spot in the sequence, add a ".2" to the second one (i.e., [... 600 600.2 ...]).
[5]

Now enter, as a vector, the image numbers that you want to use for clicking profile endpoints. These should essentially be the first image you took after having moved the camera, whether there is a usable background or cal cell image there or not. So for this vector, you do not need to deal with the .2 stuff from the other vectors.
[1 6]

Enter, as a vector and in increasing order, the concentration pathlengths of your calibration cells in ppm.
[0 114 248 395 488 763 1388]

OK Cancel

Figure B.14: Main input window for ICA processing code

Appendix B – UVCamSO₂ Tutorial

The profile image locations variable is a vector of images at which you will draw distinct profiles for integration of the plume. A new profile must be used each time the camera has a new field of view (such as the first image in the sequence, or following moving of the camera for a calibration image) or if the plume has changed location or direction relative to the profile. Such changes can be determined by inspection of the movie file previously made.

- 5) The Kilauea sample data includes a cell with no SO₂ in it, but if you were processing a dataset without a 0 ppm•m calibration cell, you would now be prompted to decide whether to use clear sky in place of a 0 ppm•m cell or simply construct a calibration curve using calibration cells with SO₂. Generally, the cell material itself does absorb UV to some degree, though it depends on the specific cells. Using clear sky instead of an absorbing empty cell can skew the calibration curve, so it's suggested that you don't substitute clear sky, although in some cases you may choose to.
- 6) The next window asks whether you would like to correct for scattering between the plume and the camera. This is important for avoiding underestimates of SO₂ emission rate, especially at distances as great as the 7 km for the Kilauea sample data. If you are processing other data, this is optional depending on user preference, but for the Kilauea data, click **'Yes.'**

If you do choose to do this distance correction, the next prompt will ask if you would like to input or estimate the beta, or volume scattering coefficient, value for the atmosphere at the volcano in the imagery. If you have external knowledge of a beta value, it can be entered, otherwise it will be estimated as close to the value for pure air. For this Kilauea sample dataset, we have no knowledge of the beta value, so click **'Estimate.'**

- 7) Another input box will ask you about the camera and lens specifications, for later calculating the pixel size in meters. For the camera system used to acquire the

Appendix B – UVCamSO2 Tutorial

sample Kilauea data, the size of the CCD array is 1024 pixels and the angular field of view of the lens is 13.3578° . If you are processing imagery from another camera, you may have to enter different values.

- 8) Next, because we are using the two-filter method, you will need to register the images from each of the cameras to each other. Despite the two cameras being mounted on the same tripod in order to have approximately the same field of view, there is generally still a shift of a few pixels that must be accounted for. This registration may be done manually by identifying the same feature on simultaneous images from each camera, or by selecting the feature in one image and having the code cross-correlate the feature with the other image. If the cross-correlation method fails for any reason, you have the option to go back and align the images manually, so we will start with the cross-correlation method. Click **‘Cross-corr.’**

You can zoom in on a feature (generally something on the landscape or edifice); just make sure the feature stands out and has contrast with whatever is behind it (Figure B.15), then click on it.

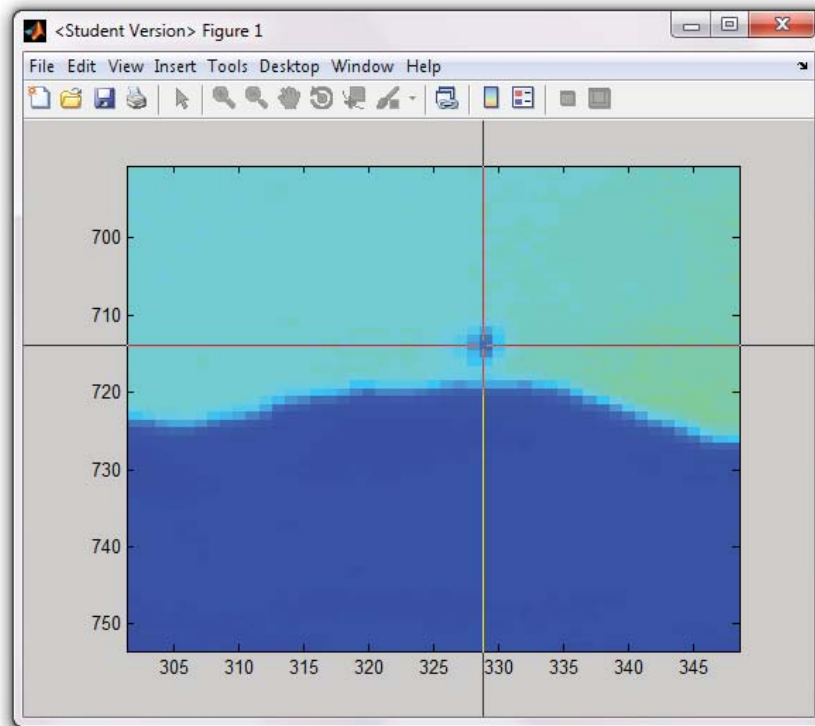


Figure B.15: Example of zooming in and selecting a distinct feature on the landscape for image alignment

Once the sample images are aligned, you are asked to verify that the alignment worked properly. If it did, click '**Keep**,' otherwise you can go back and manually click the same feature on the two images.

- 9) Next you need to draw the profile of the plume that you want to measure. Click '**OK**' on the prompt. Now you need to click the endpoints of a line across the plume that is perpendicular to the plume's propagation. You should have an idea of where the plume is going based on the image itself as well as the movie created earlier. In this image, the plume is hugging the ground, so one end of the profile will have to be at the ground surface (Figure B.16). (The fact that the plume is grounded may lead to underestimation of emission rates, but this is

Appendix B – UVCamSO2 Tutorial

unavoidable with some volcanoes given their topography.) You will repeat this profile selection (and alignment from step 10 above) process for each of the profile images you entered in the main input window; for the sample data, you will do it twice, once each for images 1 and 6.

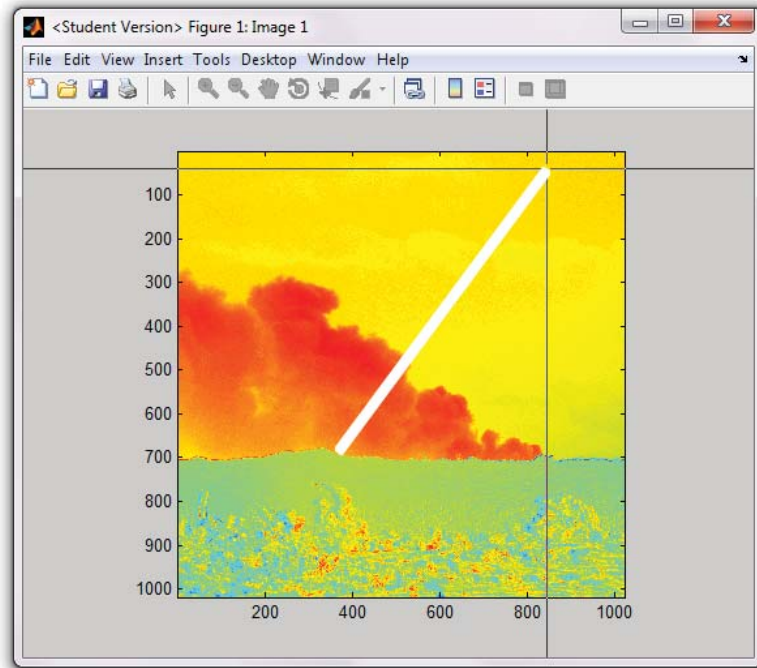


Figure B.16: Selection of a profile perpendicular to the plume, for a grounded plume

- 10) If you elected to correct for scattering, which you did for the sample data, a new prompt instructs you to select an area of representative background. For this, you should select a region of clear sky near to the plume (Figure B.17), and not far in the corner or at the edge of the image, etc. Next you will select a small area that represents the darkest part of the plume (Figure B.18). This process will repeat for each profile image, as with the alignment and profile selection.

Appendix B – UVCamSO2 Tutorial

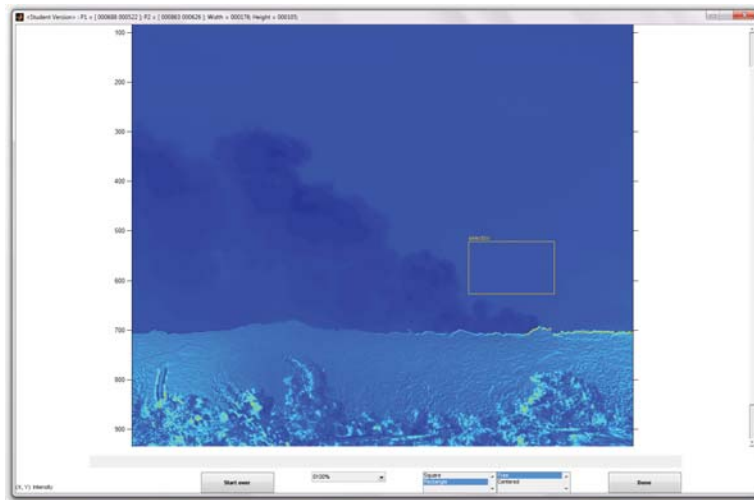


Figure B.17: Selection of background sky for distance correction

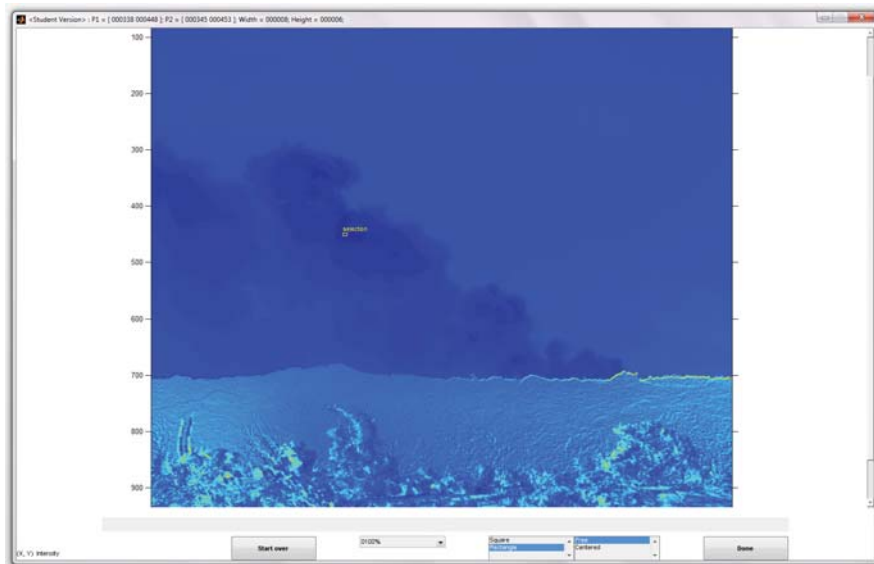


Figure B.18: Selection of a small section of the darkest portion of the plume for distance correction

- 11) Now, as you did when displaying a concentration path-length map when viewing single images, you will select boxes within calibration cell images. The code will

Appendix B – UVCamSO₂ Tutorial

prompt you to select the cells in order of increasing concentration path-length. With the two-filter mode, it is important to pay attention to prompts, as *you will need to select a box twice for each concentration path-length – once for each filter.*

- 12) Once the calibration cell boxes have all been selected, you will see a box pop-up with a red bar that ticks to the right progressively (Figure B.19). At this point, the code is processing the images. Processing time will depend on the number of images and the processing power of the computer on which the program is running.

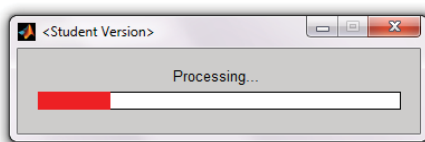


Figure B.19: Wait bar that is displayed during processing of images

- 13) What you will see now is a stack of all the image ‘slices’ along the first profile line you chose. The x-axis is time, and the y-axis is distance along the plume profile. You can see the variations on SO₂ along the line through space and time. The plume should stand out clearly against the background at either the edge of the stack (for a grounded plume) or in the middle of the image (for a lofting plume).

At the same time, the code asks about cropping zeros; this only applies for datasets with more than one profile line drawn. Because different profiles are bound to be different lengths, the program pads the bottom of the shorter profiles with zeros in order to be able to compile all the profiles into one matrix. There are two profiles for the sample data, so for one of the two profile lengths, you will have to click ‘Yes.’ If you see the box of uniform zero values across the bottom (Figure B.20), you should select the ‘Yes’ option.

Appendix B – UVCamSO2 Tutorial

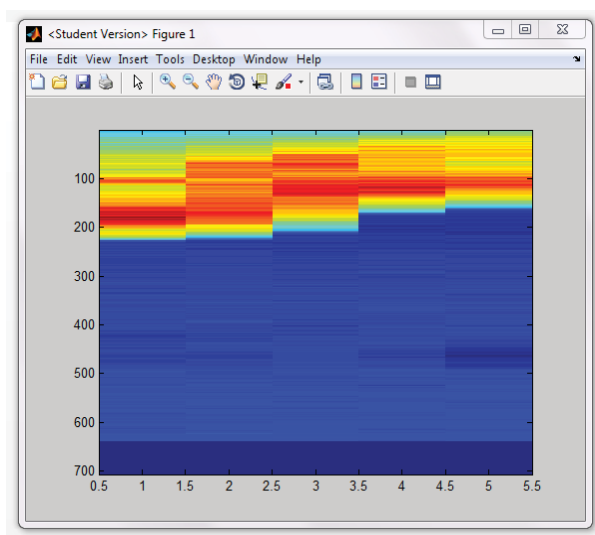


Figure B.20: Sample stack of image profiles, with time increasing to right. Note uniform dark blue section at bottom representing zero values padded on to shorter profiles.

If you do need to crop the zeros, simply click at the top of the zero area (Figure B.21).

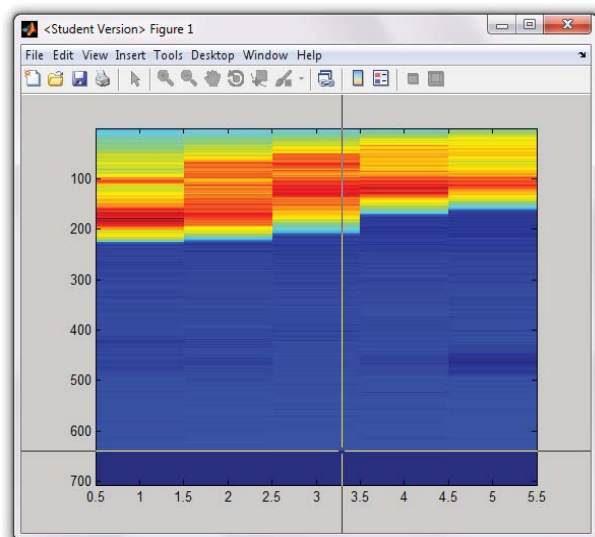


Figure B.21: Clicking the limit between image information and padded zeros

Appendix B – UVCamSO2 Tutorial

- 14) The code then asks for a background correction. If calibration images were not taken near enough in time to the plume image, skylight conditions may have changed, meaning the plume image was converted to slightly incorrect SO_2 concentration path-length values. We know the sky has no SO_2 , so here we set all the background sky for each image to zero. For this lab, click ‘**One**’ for a one-sided background correction, as we can only see background sky on one side of the grounded plume. A two-sided correction can be done on a lofting plume where the stack image has clear background sky on both sides of a central plume, while an area correction can be done if there is no clear sky area that extends laterally in the plot across all profiles.

This correction also accounts for long periods of time without calibration and any subsequent background drift that results from varying background sky conditions. We do not see this effect in the short data set from Kilauea, but an example from Fuego volcano in Guatemala is shown in Figure B.22.

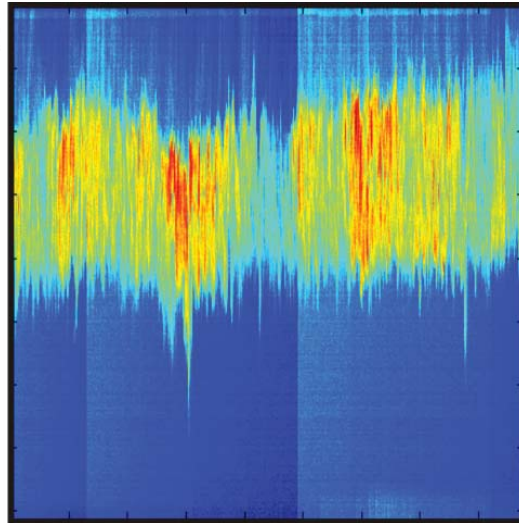


Figure B.22: Sample image stack from Fuego volcano dataset displaying variable background as a result of changing sky conditions and image exposure time

Appendix B – UVCamSO₂ Tutorial

- 15) The dark blue at the bottom of the image is the clear sky that we need to make sure is equal to zero. So right now, **click a location close to the plume, but one with no SO₂ below it in the y-direction** (Figure B.23).

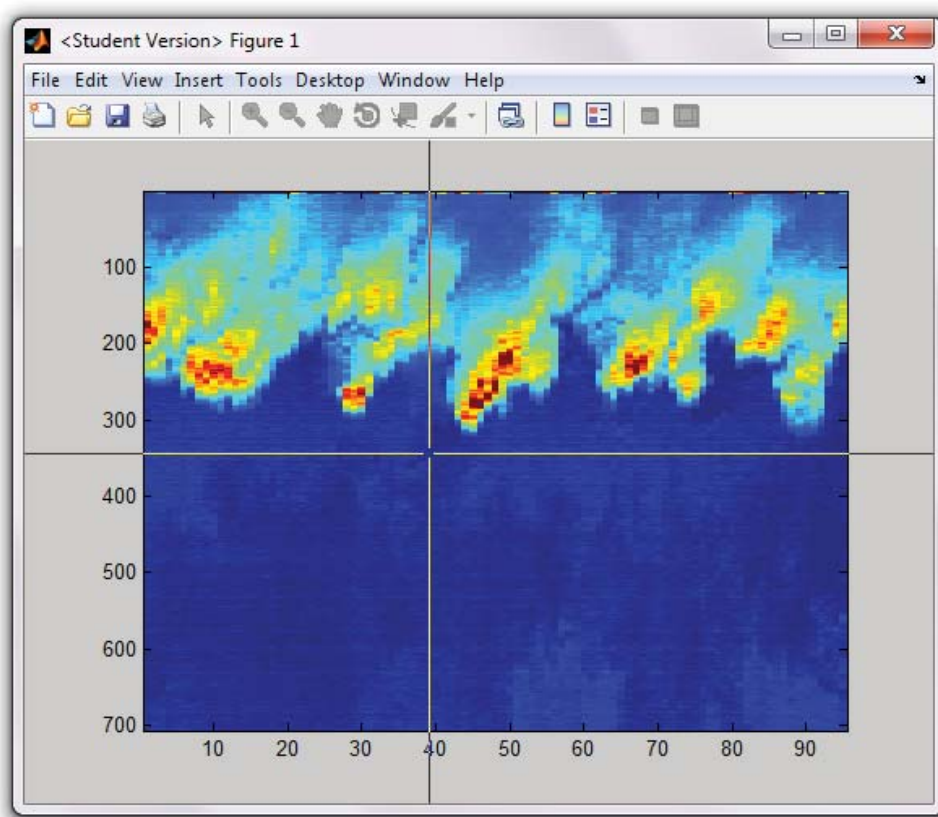


Figure B.23: Selecting limit between SO₂ and background sky

Click '**OK**' in the next prompt box, and now you will see a black line on the profile stack where you just clicked. Now **click another spot below that line so that you have a range of background sky included** (Figure B.24).

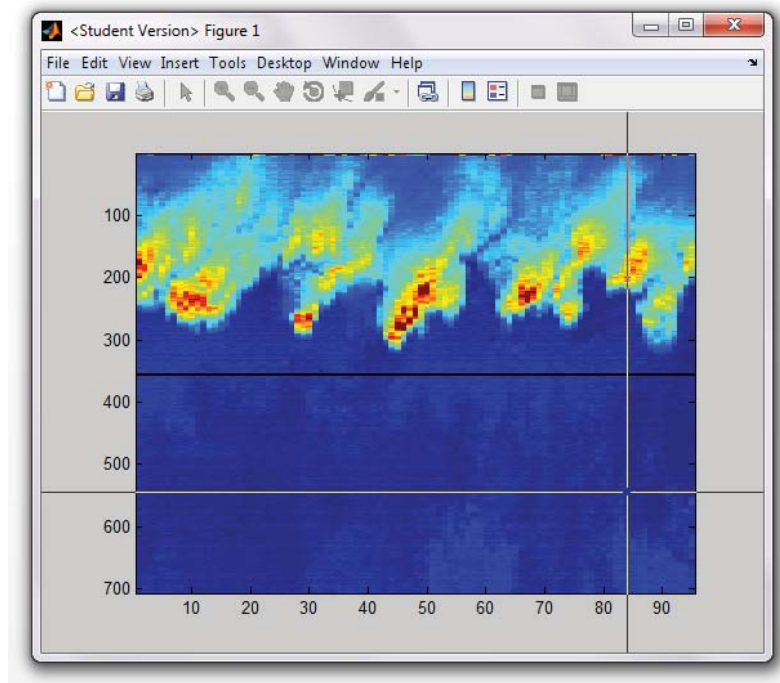


Figure B.24: Selecting bottom of background sky range following delineation of upper limit

- 16) With the background corrected, you will now see a prompt giving you the option of sub-setting the profiles so you are only measuring the plume itself and not any noise in the background. This is optional, but suggested. Click **'Yes'**. Again, because the plume is grounded here, we will ignore background on only one side of the plume, so on the next prompt, click **'One.'**

After the next prompt, click as close to the plume as you can so as to exclude the most background.

- 17) Following the background corrections and cropping for each of the profiles, a final plot of SO₂ integrated column amount is plotted for display. The ICA information is also written to a text file in the folder containing the imagery, with

a unique time identifier in the file name for distinguishing multiple processing runs on the same imagery.

B.5 Calculating plume speed

- 1) To convert the ICAs calculated above to SO₂ emissions rates, a time series of plume speeds is still required. To derive plume speeds, a similar code to the ICA module is used. Back on the main GUI window, click on ‘**Calculate plume speeds.**’
- 2) Now navigate to the same folder we did before and click ‘**OK.**’
- 3) In the next window, enter **the following for data variables**. Some are similar to last time, but not exactly, so copy carefully, and *make sure to include the square brackets* on the ones that require them:

Prefix: Image307-
Number of files: **100**
Number at the end of the first file: **1**
Examine all images: **1**
Uninterrupted sequence: **[6 100]**
Smoothing of profile: **9**
Distance from the camera to the plume (in meters): **7000**
Background image locations: **[5]**
Calibration image locations: **[5]**
Profile image locations: **[1 6]**
Calibration cell concentration path-lengths: **[0 114 248 395 488 763 1388]**

The sequence of uninterrupted imaged if necessary to determine the temporal resolution of the imagery, and the profile smoothing is the number of points used to smooth the profile of the plume in order to ensure the best cross-correlation of successive profiles.

- 4) As for the ICA module, click ‘**Yes**’ and ‘**Estimate**’ for the distance correction. Also make sure the camera specifications are entered correctly.

Appendix B – UVCamSO2 Tutorial

- 5) Now the prompt is telling you to click the endpoints of the plume's velocity vector, so click '**OK**'. As opposed to the ICA module, when the profile was chosen perpendicular to the plume's propagation, you now need to select a profile that is the same orientation as the plume's propagation vector. **Click a line similar to the one below** (Figure B.25). *Make sure you don't click on the edifice.* Repeat for each of the profile numbers entered as input.

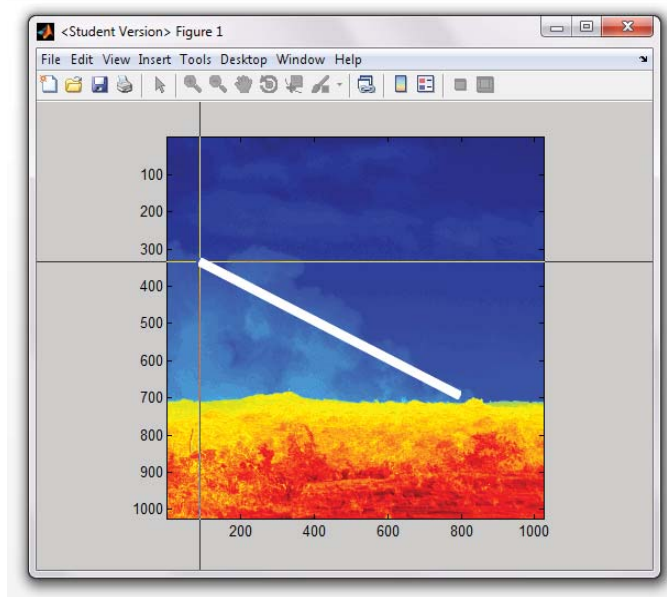


Figure B.25: Sample plume speed profile selection

- 6) Next, select boxes for the distance correction as you did for ICAs. Then select the calibration cells the same way you did before as well. Note that the plume speed code only uses one filter, so you need only select a box for each cell once.
- 7) Now you will see the code as it is working to derive plume speed (Figure B.26). In the upper left, you will see the sequence of images the code is importing along with the profile line you chose. Here you can double-check to make sure the line you chose is appropriate for the images that are being analyzed. Across the

Appendix B – UVCamSO2 Tutorial

bottom of the plot, you see two different colored lines. These are the profiles from sequential images. What the code does is perform cross-correlation to find the best fit between the two profiles. By doing this, the code identifies how far certain features, or puffs, in the plume have moved between images. Since you know how long there was in time between images, the code combines this time and distance into a plume speed. The top right plot is a running plot of the plume speed the code is calculating.

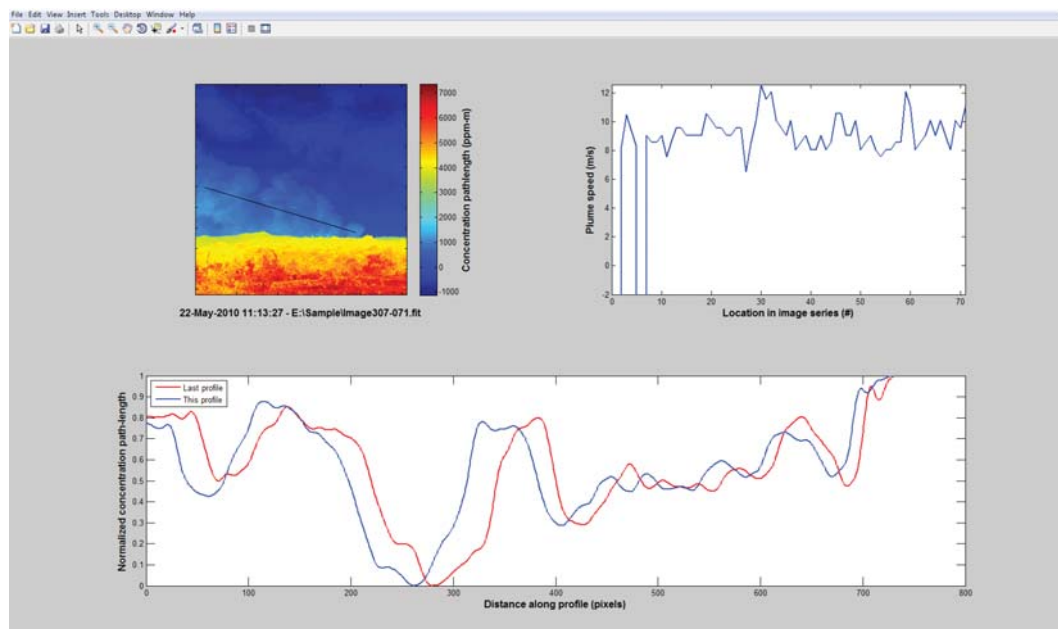


Figure B.26: Screenshot of plume speed code running

- 8) When the plume speeds are all calculated, the final plot that pops up is the time-series of plume speeds. There may be some spikes in the data, which could be a result of a bad profile line, or just the code's inability to find a good correlation, which can happen if the plume doesn't have distinct puffs/structure. Because of this, the program prompts you to smooth the time series, which should be more realistic than the spiky time series. Your smoothing window must be an even

number here, and if you choose not to smooth the dataset, simply enter '0.' The final smoothed plume speed is also then displayed on the plot with the unsmoothed time series.

- 9) Like the ICA output, the plume speed time series is written to a text file in the same folder as the original imagery.

B.6 Back-calculation of time vector

Because the ICA profiles you drew were not right at the volcanic vent, a certain amount of time will have passed between the emission of a given parcel of SO₂ at the vent and its subsequent measurement at the ICA profile line. Therefore, the image time stamp associated with the profile integration is not representative of the time of emission, which is crucial if one aims to relate SO₂ emission rate time series to volcanic phenomena at the vent, including various geophysical measurements.

To correct for the time discrepancy, you can use the plume speed you just calculated in conjunction with the distance from the vent to the profile to determine what the time would have been when a given parcel of SO₂ was emitted at the vent.

- 1) To do this back-calculation to the vent, click the button on the main GUI labeled **'Back-calculate a new time vector.'**
- 2) In the first pop-up window, you will need to select the ICA file created when you ran the code. The file name will vary depending on what images were used and what time the code was run, but there should be a file with the name format **'####-####int_notrendttttt.tttt.'** The #s are the image numbers of the first and last images in the sequence that you processed (1 and 100, for the Kilauea sample data), and the tttt portion is the Matlab time that you ran the code, so if you process multiple times, the larger number at the end of the file name is the most recent file. In the second pop-up window, choose a corresponding plume

Appendix B – UVCamSO₂ Tutorial

speed file, which will have a file name format of '####-####plspttttt.tttt.' Next you will have to select the metadata file that was created for the ICA file you just chose, with the format '####-####metadatattttt.ttt.txt.'

- 3) Because the only way to calculate the time a given parcel of SO₂ was at the vent is to know where the vent is, you now have to define the location of the vent in the imagery. If the vent would be out of the field of view of the imagery, you can define, in the coordinate system of the image, where the vent would be if the image was larger. To do so, you'll first select the folder containing the imagery and then select either '**In imagery**' or '**Off-screen**.' For this Kilauea data, the vent is just below the ground surface where the plume begins, so click '**In imagery**.'
- 4) Next, click where the vent is in the image. For Kilauea, see the Figure B.27 below. Repeat the process for each image in which you originally drew distinct profile lines. (These image numbers are read from the previously created metadata file you selected.)

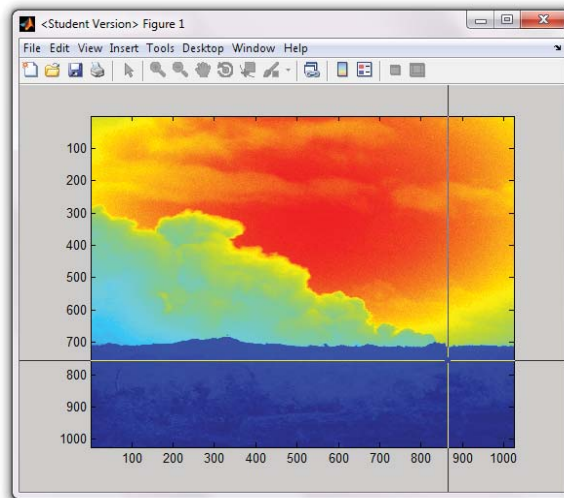


Figure B.27: Vent location selection for Kilauea volcano imagery

- 5) As with both the ICA and plume speed code, the new time vector file is output to the same folder as your images.

B.7 Emission rate calculation

- 1) At this stage, you can use the ICA and plume speed files to calculate the emission rate of SO₂ by multiplying them together with a conversion factor. Click **‘Calculate emission rates’** on the main GUI window.
- 2) In the two subsequent pop-up windows, select the desired ICA and plume speed files.
- 3) Next, the code prompts you to select the units for your emission rates. This is user preference, so select either tonnes per day (**‘t/d’**) or kilograms per second (**‘kg/s’**).
- 4) What you now see displayed on the screen is a time series plot of SO₂ emission rates from Kilauea volcano. It represents a small amount of time, but when images are collected all day, with thousands of images, you get time series that can then be usefully incorporated into multi-disciplinary datasets with geophysical data to try and understand processes at active volcanoes.

B.8 Data display

- 1) The UVCamSO2 program also includes the capability to read and display previously processed data, including ICA, plume speed, emission rate, and back-calculated time vectors. To select a display, click on **‘Read and display processed data’** in the main GUI window.
- 2) The first option presented is a choice between displaying plume speed or SO₂ data. If you chose plume speed, you will first select the file to be plotted, and then be required to select either the smoothed or unsmoothed plume speed

vector. If you select SO₂, you will be prompted to select either emission rate or ICA, and then the file you wish to plot.

- 3) Once the variable and file have been chosen, you will need to choose the vector you would like on the x-axis: consecutive data points only, image number, image time stamp, or a back calculated time vector (Figure B.28).

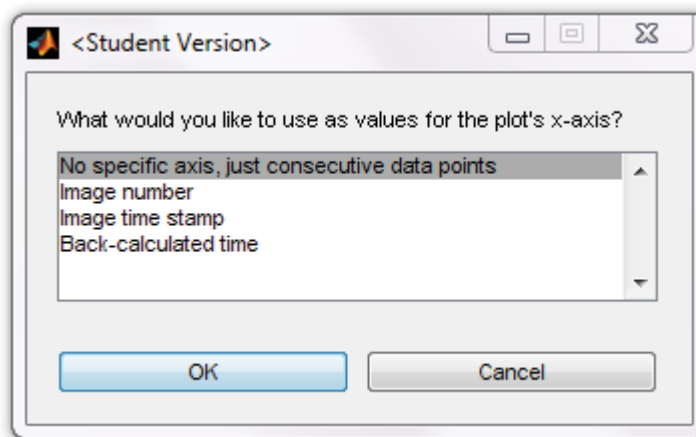


Figure B.28: X-axis selection options in data display module

If you select '**Image time stamp**,' and are displaying plume speed data, a pop-up window will require you to select the ICA file associated with your original data set. If you chose to plot against a back-calculated time vector, a pop-up will prompt you to choose the back-calculated data file.

- 4) If you plotted just data points or against image number, your final plot will appear. If you elected to plot against image time or back-calculated time, a preliminary plot of your data will appear and prompt you to inspect the x-axis. You now have the option of leaving the times as-is or offsetting them to the correct time (in the case of mismatched acquisition and computer time) or a

Appendix B – UVCamSO2 Tutorial

different time zone (in the case of converting from local time to GMT). You may then enter the offset you require, including the negative sign, if necessary.

- 5) The data is then plotted (Figure B.29), with axis labels, and the two vectors used for the axes are imported into Matlab for further manipulation, if desired.

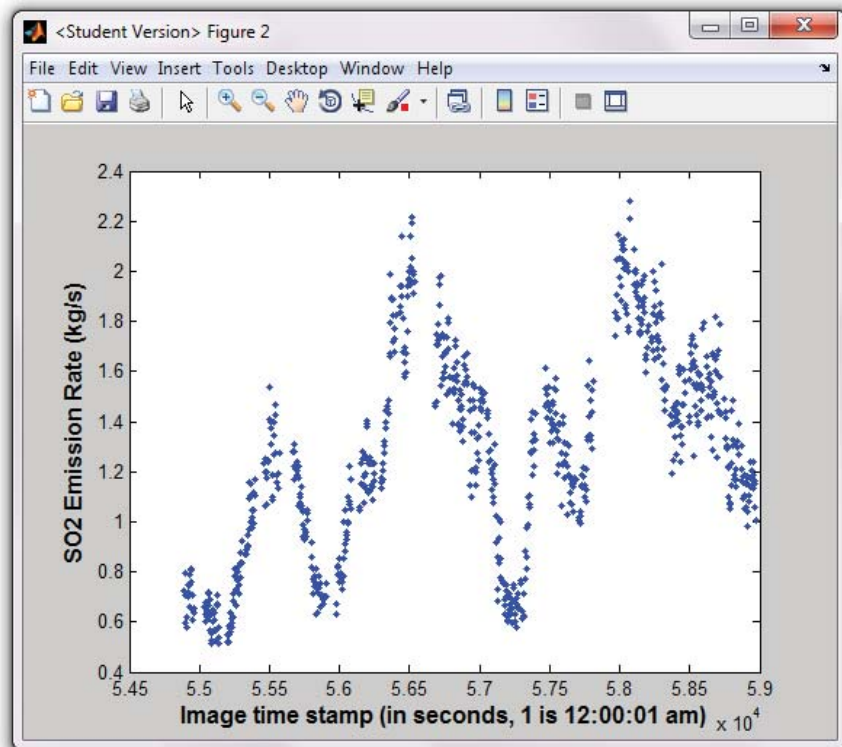


Figure B.29: Sample final plot from data display module

Appendix C: SUPPLEMENT TO CHAPTER 2 – PROGRAM CODES AND SAMPLE DATA^{*}

Matlab codes associated with the UVCamSO2 program described in Chapter 2, and used for processing data in Chapters 3, 4, and Appendix A, as well as sample data are available from the online database, Vhub.org at <http://vhub.org/resources/1069>. Included Matlab codes are:

backcalc.m
bresenham.m
ERcalc.m
hanning_smoothJL.m
imSelectROI.m
multi_image_processing_code.m
plumespeed.m
readSO2.m
uvcam_moviemake.m
UVCamSO2.fig
UVCamSO2.m
uvdisplay.m

^{*} This appendix, along with Chapter 2 and Appendices B and D, is in review as:
Nadeau, P. A. and Palma, J.L., A Matlab Program for Deriving Emission Rates of Volcanic SO₂ from UV imagery. *Computers & Geosciences*.

Appendix D: SUPPLEMENT TO CHAPTER 2 – SAMPLE OUTPUT FILES*

The following pages include sample output data and metadata files from the ICA, plume speed, back-calculation, and emission rate calculation modules of UVCamSO2. Column headings are included here in examples, but do not exist in actual data files. Data files are also clipped for display, thereby comprising only a subset of the full number of data rows.

D.1 Integrated column amount (multi_image_processing_code.m)

Table D.1: Data file (single filter), 1-100int_notrend734794.5002.txt

Image Number	Image Time Stamp (in seconds of day; from header file)	Integrated Column Amount (ppm·m ²)
1	53859	1.90E+06
2	53862	1.73E+06
3	53866	1.60E+06
4	53869	1.50E+06
5	53872	1.48E+06
6	54589	1.62E+06
7	54592	1.57E+06
8	54596	1.44E+06
9	54599	1.43E+06
10	54603	1.54E+06
11	54606	1.54E+06
12	54609	1.66E+06
13	54612	1.74E+06
14	54616	1.78E+06
15	54619	1.83E+06

*This appendix, along with Chapter 2 and Appendices B and C, is in review as:
Nadeau, P. A. and Palma, J.L., A Matlab Program for Deriving Emission Rates of Volcanic SO₂ from UV imagery. *Computers & Geosciences*.

Appendix D – Sample Output Files

Table D.2: Metadata file, single filter: 1-100metadata734794.5002.txt

18-Oct-2011 12:00:18

Initial Input Variables

Folder: E:\Sample\
Filename prefix: Image307-
Original number of files: 100
Actual number of files: 100
First file: 1
Skip: 1
Distance to plume (m): 7000
Background images: 5
Cal cell images: 5
Input images for profiles: 1 6
Actual images for profiles: 1 6
Input cal cell concentration-path lengths (ppmm): 0 114
248 395 488 763 1388
Actual (used) cal cell concentration-path lengths (ppmm):
0 114 248 395 488 763 1388
CCD resolution of camera (pixels): 1024
Angular field of view (degrees): 1.335780e+001
(Calculated Pixel size (m): 1.600972e+000)

Distance Correction Specs

Input beta: none

Image Used: 1

Beta used: 1.150000e-001

	MinX	MaxX	MinY	MaxY	Avg. Luminance
Lb	722	999	446	611	7.188498e-001
Lp	90	99	699	704	4.089892e-001

Equation: Actual Luminance = 2.2367(Measured Luminance) -
0.889

Appendix D – Sample Output Files

Image Used: 6

Beta used: 1.080000e-001

	MinX	MaxX	MinY	MaxY	Avg. Luminance
Lb	833	1002	382	659	7.595220e-001
Lp	577	585	736	742	4.166965e-001

Equation: Actual Luminance = 2.1297(Measured Luminance) - 0.85806

Calibration Cell Area Coordinates

Image 5:

Cell (ppmm) MinX MaxX MinY MaxY Avg. Value (absorbance)

0	524	550	322	339	1.575600e-001
114	377	392	464	482	2.014970e-001
248	477	491	422	440	1.737667e-001
395	594	617	508	536	2.018263e-001
488	678	701	447	465	2.553958e-001
763	589	609	412	435	2.951165e-001
1388	465	490	522	546	3.418310e-001

Profile Line Coordinates

Image 1:

X1	X2	Y1	Y2
366	895	695	82

Image 6:

X1	X2	Y1	Y2
360	793	728	22

Appendix D – Sample Output Files

End Input Variables

Images 1-plus:

Zero crop? Yes

Y value of crop level: 607

Background correction type: ONE

Background limit (top): 235

Background limit (bottom): 3.858947e+002

Subset to avoid messy background? Yes

Ignoring where? ONE

Background location: Below limit

Multiple plumes? No

Images 6-plus:

Zero crop? No

Background correction type: ONE

Background limit (top): 305

Background limit (bottom): 6.754576e+002

Subset to avoid messy background? Yes

Ignoring where? ONE

Background location: Below limit

Multiple plumes? No

Final series of profiles output to:

E:\Sample\1-100ppmm_line_profiles734794.5002.txt

Final time series of ICAs output to:

E:\Sample\1-100int_notrend734794.5002.txt

If you delineated multiple plumes at all, those files were written to the same folder as the above two files, with

Appendix D – Sample Output Files

'multiICA' in each of their file names. The time will be the same as the above files as well.

*All .txt files are tab-delimited

Table D.3: Data file, dual filter: 1-100int_notrend_2filt_734794.5347.txt

Image Number	Image Time Stamp (in seconds of day; from header file)	Integrated Column Amount (ppm·m ²)
1	53859	9.17E+05
2	53862	8.94E+05
3	53866	8.38E+05
4	53869	8.62E+05
5	53872	1.10E+06
6	54589	1.46E+06
7	54592	1.48E+06
8	54596	1.39E+06
9	54599	1.25E+06
10	54603	1.34E+06
11	54606	1.53E+06
12	54609	1.51E+06
13	54612	1.69E+06
14	54616	1.93E+06
15	54619	1.92E+06

Table D.4: Metadata file, dual filter: 1-100metadata_2filt_734794.5347.txt

18-Oct-2011 12:50:00

Initial Input Variables

Folder: E:\Sample\
Two filters:
Filename prefix for 307: Image307-
Filename prefix for 326: Image326-
Original number of files: 100
Actual number of files: 100
First file: 1
Skip: 1
Distance to plume (m): 7000

Appendix D – Sample Output Files

Background images: 5
Cal cell images: 5
Input images for profiles: 1 6
Actual images for profiles: 1 6
Input cal cell concentration-path lengths (ppmm): 0 114
248 395 488 763 1388
Actual (used) cal cell concentration-path lengths (ppmm):
0 114 248 395 488 763 1388
CCD resolution of camera (pixels): 1024
Angular field of view (degrees): 1.335780e+001
(Caluclated Pixel size (m): 1.600972e+000)

2-filter alignment shifts (motion of 326 with respect to
307)
(Negative is 326 moving left or up, positive is 326 moving
right or down)

Image 1: X shift (columns) Y shift (rows)
Cross-corr -1 6

Image 6: X shift (columns) Y shift (rows)
Cross-corr -2 6

Distance Correction Specs

Input beta: none

Image Used: 1

Beta used: 1.180000e-001

	MinX	MaxX	MinY	MaxY	Avg. Luminance
Lb	708	994	359	609	9.679006e-001
Lp	334	337	445	448	5.603717e-001

Equation: Actual Luminance = 2.2842(Measured Luminance) -
1.2429

Image Used: 6

Appendix D – Sample Output Files

Beta used: 1.180000e-001

	MinX	MaxX	MinY	MaxY	Avg. Luminance
Lb	749	991	386	604	9.887390e-001
Lp	402	404	512	516	5.725034e-001

Equation: Actual Luminance = 2.2842(Measured Luminance) - 1.2697

307 Calibration Cell Area Coordinates

Image 5:

Cell (ppmm) MinX MaxX MinY MaxY Avg. Value (flattened)

0	523	536	328	343	-7.019354e-001
114	376	394	467	486	-6.281360e-001
248	469	491	423	440	-6.693673e-001
395	592	624	510	539	-6.279789e-001
488	675	704	445	472	-5.549087e-001
763	586	616	410	436	-5.066745e-001
1388	459	495	527	547	-4.555862e-001

326 Calibration Cell Area Coordinates

Image 5:

Cell (ppmm) MinX MaxX MinY MaxY Avg. Value (flattened)

0	473	486	403	418	-6.805137e-001
114	339	354	538	554	-6.865150e-001
248	419	443	491	512	-7.739447e-001
395	536	566	572	597	-6.891203e-001
488	610	635	506	534	-7.006369e-001
763	527	551	481	502	-6.559102e-001
1388	411	449	587	606	-6.618811e-001

Appendix D – Sample Output Files

Profile Line Coordinates

(These are coordinates on the new overlain/cropped image, with 326 already having been shifted to align with 307.)

Image 1:

X1 X2 Y1 Y2
359 929 687 92

Image 6:

X1 X2 Y1 Y2
366 712 725 18

End Input Variables

Images 1-plus:

Zero crop? Yes
Y value of crop level: 594

Background correction type: ONE

Background limit (top): 219
Background limit (bottom): 3.856462e+002
Subset to avoid messy background? Yes

Ignoring where? ONE
Background location: Below limit

Multiple plumes? No

Images 6-plus:

Zero crop? No
Background correction type: ONE

Background limit (top): 368
Background limit (bottom): 6.784825e+002

Appendix D – Sample Output Files

Subset to avoid messy background? Yes

Ignoring where? BOTH

Upper plume limit (on image --> smaller y-value): 9

Lower plume limit (on image --> bigger y-value): 326

Multiple plumes? No

Final series of profiles output to:

E:\Sample\1-100ppmm_line_profiles_2filt_734794.5347.txt

Final time series of ICAs output to:

E:\Sample\1-100int_notrend_2filt_734794.5347.txt

If you delineated multiple plumes at all, those files were written to the same folder at the above two files, with 'multiICA' in each of their file names. The time will be the same as the above files as well.

*All .txt files are tab-delimited

D.2 Plume speed (plumespeed.m)

Table D.5: Data file: 1-100plsp734794.5537.txt

Image Number	Plume Speed (m/s)	Smoothed Plume Speed (m/s)
1	6.4076	7.3161
2	6.4076	7.4959
3	7.4755	7.6794
4	6.9416	7.8662
5	7.4755	8.0508
6	8.3413	8.2272
7	9.207	8.3942
8	9.207	8.5529
9	9.7185	8.7019
10	9.7185	8.8364
11	8.184	8.95
12	9.207	9.0409
13	9.207	9.1153

Appendix D – Sample Output Files

14	7.6725	9.1793
15	8.6955	9.2403

Table D.6: Metadata file: 1-100plsp_metadata734794.5537.txt

18-Oct-2011 13:17:23

Initial Input Variables

```

Folder: E:\Sample\
Filename prefix: Image307-
Original number of files: 100
Actual number of files: 100
First file: 1
Skip: 1
Images used for calculating temporal resolution: 6 100
Smoothing window on profile for cross-correlation: 9
Distance to plume (m): 7000
Background images: 5
Cal cell images: 5
Input images for profiles: 1 6
Actual images for profiles: 1 6
Input cal cell concentration-path lengths (ppmm): 0 114
248 395 488 763 1388
Actual (used) cal cell concentration-path lengths (ppmm):
0 114 248 395 488 763 1388
CCD resolution of camera (pixels): 1024
Angular field of view (degrees): 1.335780e+001
(Calculated Pixel size (m): 1.600972e+000 )

```

Distance Correction Specs

Input beta: none

Image Used: 1

Beta used: 1.140000e-001

MinX MaxX MinY MaxY Avg. Luminance

Appendix D – Sample Output Files

Lb 698 998 458 622 7.123183e-001
Lp 130 138 697 702 4.038539e-001

Equation: Actual Luminance = 2.2211(Measured Luminance) -
0.86981

Image Used: 6

Beta used: 1.080000e-001

	MinX	MaxX	MinY	MaxY	Avg. Luminance
Lb	797	990	365	665	7.600292e-001
Lp	581	586	736	744	4.167587e-001

Equation: Actual Luminance = 2.1297(Measured Luminance) -
0.85864

Calibration Cell Area Coordinates

Image 5:

Cell (ppmm) MinX MaxX MinY MaxY Avg. absorbance

0	523	547	323	343	1.565085e-001
114	373	393	463	487	2.018661e-001
248	472	489	421	442	1.746268e-001
395	589	616	505	535	2.024288e-001
488	681	700	448	474	2.558636e-001
763	585	612	410	433	2.954317e-001
1388	458	488	522	545	3.419943e-001

Profile Line Coordinates

Image 1:

X1	X2	Y1	Y2
783	167	688	394

Appendix D – Sample Output Files

Image 6:

```
X1 X2 Y1 Y2
780 38 727 463
```

Size of Hanning window used to smooth final plume speed
time series: 20

Final time series of plume speeds output to:
E:\Sample\1-100plsp734794.5537.txt

*All .txt files are tab-delimited

D.3 Back-calculation to vent (backcalc.m)

Table D.7: Data file: 1-100backcalc734794.7405.txt

Image Number	Image Time Stamp (in seconds of day; from header file)	Time at vent (back- calculated, in seconds of day)
1	53859	53769
2	53862	53772
3	53866	53777
4	53869	53780
5	53872	53783
6	54589	54488
7	54592	54491
8	54596	54496
9	54599	54499
10	54603	54504
11	54606	54508
12	54609	54511
13	54612	54515
14	54616	54520
15	54619	54524

Table D.8: Metadata file: 1-100backcalc_metadata734794.7405.txt

18-Oct-2011 17:46:23

Appendix D – Sample Output Files

Initial Input Files for Back-Calculation

ICA file: E:\Sample\1-100int_notrend_2filt_734794.5347.txt

PS file: E:\Sample\1-100plsp734794.5537.txt

Metadata file: E:\Sample\1-100metadata_2filt_734794.5347.txt

Final time series of back-calculated times output to:
E:\Sample\1-100backcalc734794.7405.txt

*All .txt files are tab-delimited

D.4 Emission rate (ERcalc.m)

Table D.9: Data file: 1-100EmRate-kgs734794.7568.txt

Image Number	Image Time Stamp (in seconds of day; from header file)	SO ₂ Emission Rate (kg/s)
1	53859	17.862
2	53862	17.839
3	53866	17.141
4	53869	18.056
5	53872	23.624
6	54589	32.084
7	54592	33.106
8	54596	31.755
9	54599	29.024
10	54603	31.464
11	54606	36.525
12	54609	36.417
13	54612	40.936
14	54616	47.195
15	54619	47.201

Table D.10: Metadata file: 1-100EmRate-kgsmetadata734794.7568.txt

18-Oct-2011 18:09:50

Appendix D – Sample Output Files

Initial Input Files for Emission Rate

ICA file: E:\Sample\1-100int_notrend_2filt_734794.5347.txt

PS file: E:\Sample\1-100plsp734794.5537.txt

Final time series of emission rates output to:

E:\Sample\1-100EmRate-kgs734794.7568.txt

*All .txt files are tab-delimited

Appendix E: SUPPLEMENT TO CHAPTER 3 – METHODOLOGY TO DERIVE EMISSION RATES OF SULFUR DIOXIDE FROM UV IMAGERY*

The UV camera used for this study consists of an Apogee Alta U6 camera with a Kodak KAF-1001E-2 1024×1024 pixel CCD. The camera was outfitted with a 105 mm CoastalOpt UV lens and a 10 nm FWHM (full width, half-max; such that the full bandwidth encompassing peak transmission wavelength to half the maximum intensity of transmission on each side of the peak is 10 nm) bandpass filter centered at 307 nm from Andover Optics. For calibration of plume imagery, periodic images were taken of five quartz cells containing known concentration path-lengths (units of ppm.m) of SO₂. Readers are referred to *Bluth et al.* [2007] and *Dalton et al.* [2009] for more detailed descriptions and discussions on the use of the UV camera. A brief description of the methodology used for processing the raw UV imagery follows below.

Conversion of the raw imagery to emission rates of SO₂ is performed by a semi-automatic processing routine specific to the derivation of volcanic SO₂ emission rates from UV camera imagery. The algorithms have been programmed in MATLAB. Via user interaction, sequences of images and associated metadata are imported in to the program. User-defined variables include the distance of the camera from the volcano's summit and the concentration path-lengths of the calibration cells that were employed, of which there may be any number. The program includes an option of applying a distance correction [*Bluth et al.*, 2007; *Shannon*, 2006] to account for scattering between the plume and the camera. The

* This appendix, along with Chapter 3, was previously published as:

Nadeau, P. A., J. L. Palma, and G. P. Waite (2011), Linking volcanic tremor, degassing, and eruption dynamics via SO₂ imaging, *Geophysical Research Letters*, 38(1), L01304.

Copyright 2011 by the American Geophysical Union. See Appendix F for a copy of the copyright transfer agreement.

Appendix E – Methodology for Chapter 3

user then selects profile lines (ideally) perpendicular to the direction of plume propagation and as close as possible to the degassing vent (Figure E.1), as well as representative sections of all calibration cells. Raw calibration images are converted into maps of absorbance via Beer's Law. Mean absorbance values from the user-selected areas in each cell in the calibration images are used with the known concentration path-length values of the cell to derive a linear calibration curve relating absorbance to concentration path-length. For each image in the sequence, the calibration curve is used to convert the image to a map of concentration path-length of SO_2 . Each converted SO_2 image is then sampled along the input profile line such that each image yields a profile of SO_2 concentration path-length. Upon completion of the processing for all individual images, the series of profile lines is plotted in an image as a stack of profiles. At this stage, background drift (a result of diurnal variation in sun illumination) and non-zero backgrounds may be corrected for via user designation of SO_2 -free areas of the profile stack. Lastly, each corrected profile is integrated using a trapezoidal approximation to yield an integrated column amount (ICA) of SO_2 (units of $\text{ppm}\cdot\text{m}^2$) for each image in the sequence. For time periods when more than one distinct plume (i.e., plumes from different vents) was distinguishable, a modified code was used to determine the ICA from each vent. Single profile lines were chosen, as above, with multiple plumes being encompassed by the single line. Profiles were again stacked and adjusted for background drift. While the main processing code integrates over the full profile line, the multi-vent code displayed the stack of profiles for the user. Based on profile appearance the user then clicked the pixel determined to be the division between the two plumes. Because the plume migrated laterally through time with minor wind shifts, each image's profile was clicked separately. Following the division of the two plumes for each profile, each of the two portions of all the profiles was integrated, yielding an ICA for each of the two plumes for each image.

To derive plume speed, a parallel program uses nearly identical initial input. In place of a profile perpendicular to the plume, a longitudinal profile of the plume is selected and

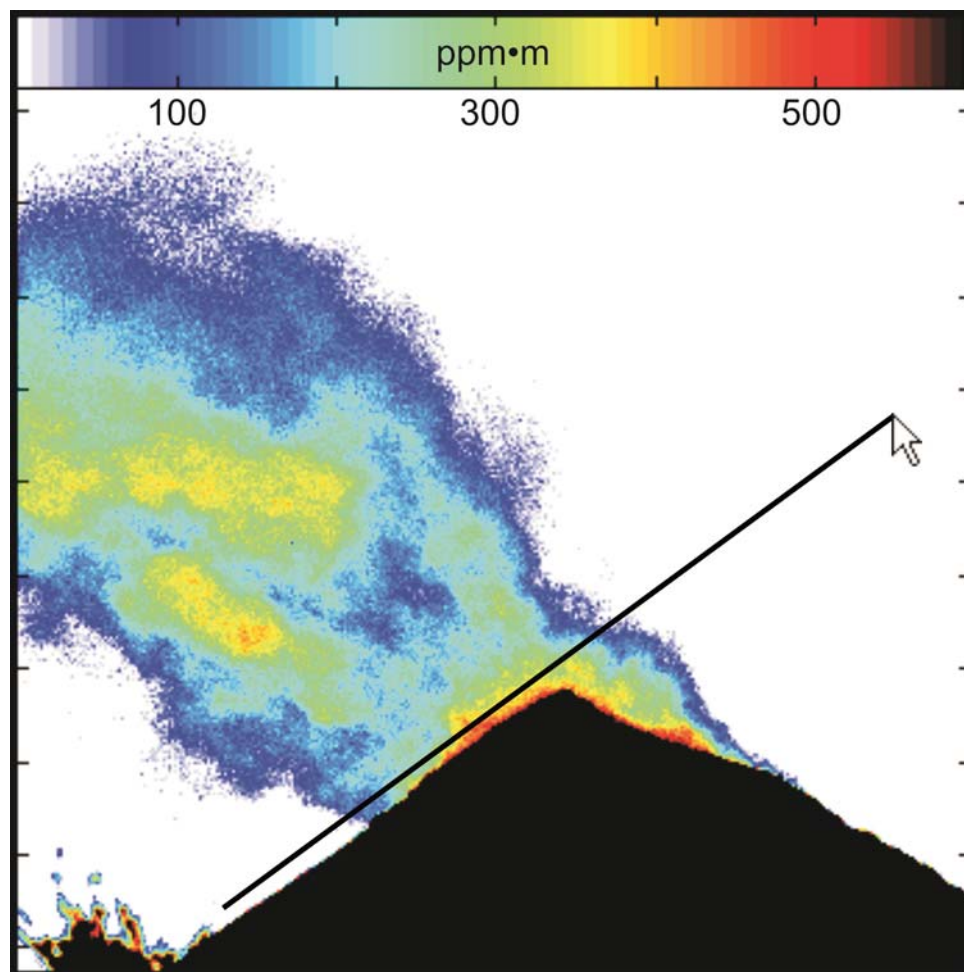


Figure E.1: Sample UV image converted to map of concentration path-length of SO₂, with sample profile line.

applied to the maps of SO₂ concentration path-length. In a modification of the method of plume speed derivation of *Williams-Jones et al.* [2006], profiles from successive images are iteratively fit to maximize the coefficient of determination (r^2). The spatial lag at which this maximum occurs is used with the temporal resolution of the imagery to derive a plume speed for each pair of images. The plume speed time-series is smoothed using an 8-point Hann window. The smoothed time-series of plume speeds is then multiplied by the timeseries of ICAs to yield a time-series of SO₂ emission rates. Times associated with the SO₂ emission rates are initially the time of the image wherein the measured SO₂ has already traveled a distance from the vent. Plume speeds, in combination with the known location of the original ICA profile line, are then used in order to back-calculate the time series to the vent by determining the amount of time the measured parcel of SO₂ took to reach the measurement profile. Times are adjusted to yield a time series of SO₂ as it was emitted at the vent.

E.1 References

- Bluth, G. J. S., J. M. Shannon, I. M. Watson, A. J. Prata, and V. J. Realmuto (2007), Development of an ultra-violet digital camera for volcanic SO₂ imaging, *Journal of Volcanology and Geothermal Research*, 161(1-2), 47-56.
- Dalton, M. P., I. M. Watson, P. A. Nadeau, C. Werner, W. Morrow, and J. M. Shannon (2009), Assessment of the UV camera sulfur dioxide retrieval for point source plumes, *Journal of Volcanology and Geothermal Research*, 188(4), 358-366.
- Shannon, J. M. (2006), Development and application of new techniques for sulfur dioxide monitoring at active volcanoes, Michigan Technological University, Houghton, Michigan.
- Williams-Jones, G., K. A. Horton, T. Elias, H. Garbeil, P. J. Mougini-Mark, A. J. Sutton, and A. J. L. Harris (2006), Accurately measuring volcanic plume velocity with multiple UV spectrometers, *Bulletin of Volcanology*, 68(4), 328-332.

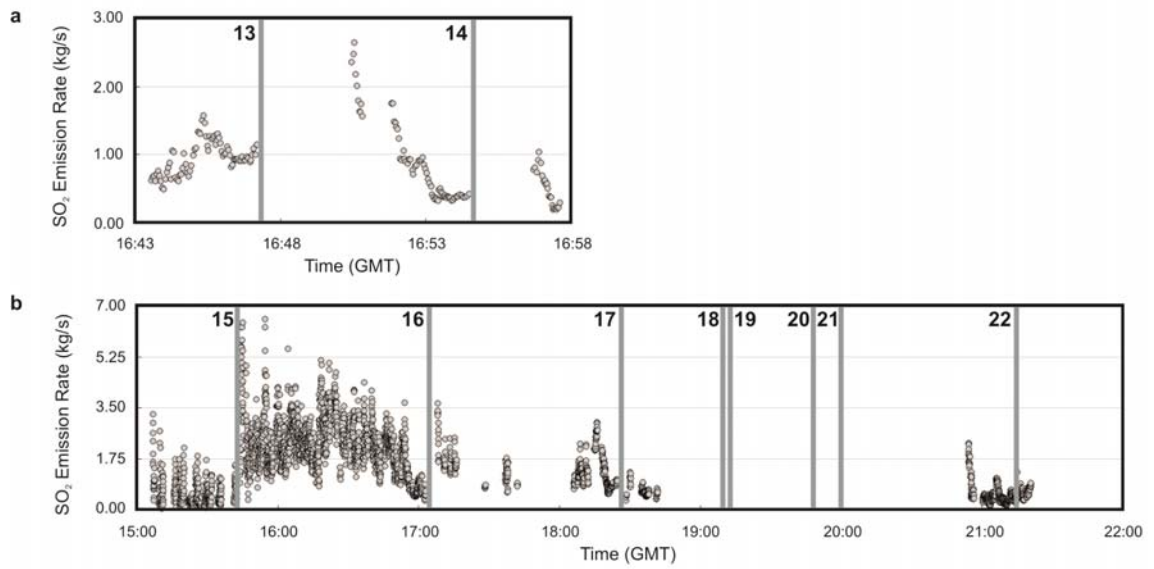


Figure E.2: Emission rates of SO₂ (circles) plotted alongside explosion occurrences (vertical gray lines) for (a) 12 January 2009 and (b) 14 January 2009.

Appendix F: COPYRIGHT PERMISSIONS

AMERICAN GEOPHYSICAL UNION

2000 Florida Avenue, NW, Washington, DC 20009

Tel: 202-462-6900
Author Information: 202-777-7354

FAX: 202-777-7395

PAPER NUMBER: 2010GL045820

JOURNAL TITLE: Geophysical Research Letters

PAPER TITLE: Linking volcanic tremor, degassing, and eruption dynamics via SO₂ imaging

AUTHOR(S): Nadeau, P. A., J. L. Palma, and G. P. Waite

This form is to be signed by at least one author. If more than one author chooses to sign, please type or print the name beside each signature. If the article was commissioned by another person or organization or was written as part of the duties of an employee, an authorized representative of the commissioning organization or employer should sign. (See below for explanation of conditions.)

COPYRIGHT AGREEMENT

I have the consent of each author to transfer copyright of the article referenced above. I hereby assign and transfer to the American Geophysical Union copyright and all rights under it. I further confirm that this article has not been published previously elsewhere, nor is it under consideration by any other publisher.

Signature

Patricia A. Nadeau

Name, Printed or Typed

Title (if not Author)

12/1/10
Date

Michigan Technological University

Institution Name

1400 Townsend Dr.

Street Address

Houghton	MI	49931	USA
City	State	Zip	Country

CERTIFICATION OF U.S. GOVERNMENT WORK

Sign this section only if ALL authors were U.S. Government employees at the time the work was prepared. Any privately employed authors should sign above. (See below for explanation.)

I certify that the article referenced above was prepared solely by U.S. Government employees as part of their official duties and therefore legally cannot be copyrighted. I confirm that this article has not been published previously elsewhere, nor is it under consideration by any other publisher.

Signature

Name, Printed or Typed

Title (if not Author)

Date

Institution Name

Street Address

City	State	Zip	Country
------	-------	-----	---------

AGU cannot publish any works without a properly effected copyright transfer agreement. Authors of manuscripts subject to Crown copyright, i.e., those that are prepared solely by official employees of the governments of the United Kingdom, Canada, Australia, New Zealand, or other members of the Commonwealth, should contact AGU for an alternate copyright transfer form.

Please sign and return this form to Publications Administration

Fax: 202-777-7395; mail: AGU, 2000 Florida Avenue, NW, Washington, DC 20009 USA

Appendix F – Copyright Permissions

INFORMATION CONCERNING YOUR COPYRIGHT AGREEMENT

The Copyright Law enacted in 1978 requires the American Geophysical Union to obtain specific rights to articles published. This legal requirement does not alter in any way the long-standing relationship between AGU and its authors, nor does it change the philosophy behind our practice of copyrighting our journals and books.

AGU's philosophy recognizes the need to ensure that authors have a say in how their works are used and the necessity to foster broad dissemination of scientific literature while protecting the viability of the publication system. Authors still retain all proprietary rights other than copyright (such as patent rights), the right to present the material orally, the right to reproduce figures, tables, and extracts properly cited, and the right to deny subsequent commercial use of the paper.

Permission to Deposit an Article in an Institutional Repository

AGU allows authors to deposit their journal articles if the version is the final published citable version of record, the AGU copyright statement is clearly visible on the posting, and the posting is made 6 months after official publication by the AGU.

Public Domain

Work prepared by U.S. Government employees in their official capacities is not subject to copyright in the United States. Such authors may place their papers in the public domain, which means that it may be freely copied, republished, and redistributed. In order for the work to be placed in the public domain, all authors must be official U.S. Government employees. If at least one author of the work was privately employed, copyright should be transferred to AGU by any of the privately employed authors.

Works Prepared by Both Privately Employed Persons and Official U.S. Government Employees

To ensure that we can continue to promote wide availability of our publications, AGU requests all non-U.S. Government employees to transfer copyright to us. This transfer permits us to continue publishing our journals and books in all their various formats, to grant permission to abstracting and indexing services to cover our publications, and to grant permission for photocopying beyond the limits defined in the law. In instances where authorship consists of both U.S. Government and privately employed individuals, we require at least one privately employed author to transfer copyright to AGU. This kind of transfer provides ultimate protection and broad dissemination of the work.

Rights Other Than Copyright

Privately employed authors who have written articles in their official capacities as employees should also transfer copyright to AGU. The author's employer retains the same rights as individual authors. AGU claims no right to the work other than copyright; the author's employer retains all other rights such as patent rights.

Works Supported by U.S. Government Grants or Contracts

Authors who are publishing works supported by a U.S. Government grant or contract are requested to transfer copyright to AGU. This kind of transfer permits the broad dissemination of the work while recognizing the U.S. Government's prior license to use the work for noncommercial purposes.

Copyright Permission for Reprinted/Modified Figures/Tables

If any of the figures/tables in your article are reprinted or modified from another source (this includes any that were redrawn but are basically unaltered or have only slight modifications), you must obtain and provide AGU with original letter(s) (fax or e-mail not acceptable) from the copyright holder(s) granting permission to use them in your article before your article may be published. If the original copyright holder has given blanket permission for reuse with credit, a copy of the published permission statement is sufficient. If the material is in the public domain, please provide confirmation of this in an original letter. Material originally published in AGU publications does not require copyright permission as long as proper credit is given.

* * * * *

Please sign the applicable portion of the form and return it promptly to AGU. We cannot begin the production process until this signed form has been received. Please help us to expedite the publication of your paper with your immediate response. If you have any questions, please call the AGU Author Information Line at (202) 777-7354.

July 1999 (rev. Jan 2010)

Excerpts from the The MathWorks, Inc. (Matlab) Software License Agreement:

4. LICENSE RESTRICTIONS. The License is subject to the express restrictions set forth below. Licensee shall not, and shall not permit any Third Party to: ...
 - 4.7. use MathWorks' **name, trade names, logos**, or other trademarks of MathWorks or any of its Affiliates or Licensors in any advertising, promotional literature or **any other material**, whether in written, electronic, or other form, distributed to any Third Party, **except in the form provided by MathWorks, and then solely for purposes of identifying MathWorks' Programs; ...**

THE MATHWORKS, INC. SOFTWARE LICENSE AGREEMENT - Deployment Addendum

This is an Addendum to The MathWorks, Inc. Software License Agreement (the "Agreement"), and the terms and conditions of this Addendum are incorporated therein. Each capitalized term used herein and not defined herein shall have the meaning ascribed to it in the Agreement.

1. PURPOSE. The MathWorks, Inc. Software License Agreement (the "Agreement") contains restrictions prohibiting Licensee from modifying, distributing, or providing access to the Programs or any Program Components (as defined below), except as expressly provided in this Addendum. If the Programs licensed by Licensee under the Agreement contain Source Code or Object Code Program Components, then this Addendum sets forth the Licensee's rights with respect to creating Applications and Derivative Forms and distributing Applications, Derivative Forms, and Deployment Programs, as well as certain additional obligations related thereto.

MathWorks or its Licensors retain all right, title, and interest in Its Programs, Program Components, and Derivative Forms of its Programs.

2. USER CREATED FILES. **This Addendum does not apply to M-files, MDL-files, MEX-files, MAT- files, VHDL-files, Verilog-files, FIG-files and P-files that are created by Licensee** and that do not include any code obtained from M-files, MAT-files, P-code, MDL-files, C/C++ files, VHDL-files, Verilog-files, TLC-files, or other Source Code files supplied with the Programs ("**User Files**"). **Licensee may distribute, sublicense, and resell without restriction, User Files.**